

Air Force Institute of Technology

**AFIT Scholar**

---

Theses and Dissertations

Student Graduate Works

---

6-12-2008

## The Effect of Radiation on the Electrical Properties of Aluminum Gallium Nitride/Gallium Nitride Heterostructures

John W. McClory

Follow this and additional works at: <https://scholar.afit.edu/etd>



Part of the [Electromagnetics and Photonics Commons](#), and the [Semiconductor and Optical Materials Commons](#)

---

### Recommended Citation

McClory, John W., "The Effect of Radiation on the Electrical Properties of Aluminum Gallium Nitride/Gallium Nitride Heterostructures" (2008). *Theses and Dissertations*. 2644.  
<https://scholar.afit.edu/etd/2644>

This Dissertation is brought to you for free and open access by the Student Graduate Works at AFIT Scholar. It has been accepted for inclusion in Theses and Dissertations by an authorized administrator of AFIT Scholar. For more information, please contact [richard.mansfield@afit.edu](mailto:richard.mansfield@afit.edu).



**THE EFFECT OF RADIATION ON THE ELECTRICAL  
PROPERTIES OF ALUMINUM GALLIUM NITRIDE/GALLIUM  
NITRIDE HETEROSTRUCTURES**

DISSERTATION

John W. McClory, Lieutenant Colonel, USA

AFIT/DS/ENP/08-01

**DEPARTMENT OF THE AIR FORCE  
AIR UNIVERSITY**

***AIR FORCE INSTITUTE OF TECHNOLOGY***

---

**Wright-Patterson Air Force Base, Ohio**

APPROVED FOR PUBLIC RELEASE; DISTRIBUTION UNLIMITED

The views expressed in this thesis are those of the author and do not reflect the official policy or position of the United States Air Force, Department of Defense, or the United States Government.

AFIT/DS/ENP/08-01

THE EFFECT OF RADIATION ON THE ELECTRICAL PROPERTIES OF  
ALUMINUM GALLIUM NITRIDE/GALLIUM NITRIDE HETEROSTRUCTURES

DISSERTATION

Presented to the Faculty

Graduate School of Engineering and Management

Air Force Institute of Technology

Air University

Air Education and Training Command

in Partial Fulfillment of the Requirements for the

Degree of Doctor of Philosophy

John W. McClory, BS, MS

Lieutenant Colonel, USA

June 2008

APPROVED FOR PUBLIC RELEASE; DISTRIBUTION UNLIMITED

THE EFFECT OF RADIATION ON THE ELECTRICAL PROPERTIES OF  
ALUMINUM GALLIUM NITRIDE/GALLIUM NITRIDE HETEROSTRUCTURES

John W. McClory, BS, MS  
Lieutenant Colonel, USA

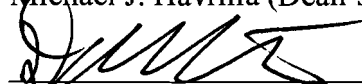
Approved:

  
James C. Petrosky (Chairman)

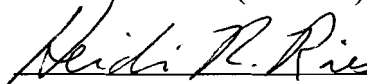
06 Jun 08  
Date

  
Michael J. Havrilla (Dean's Representative)

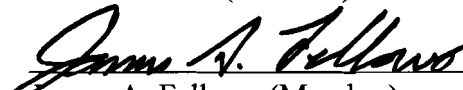
06 Jun 08  
Date

  
David E. Weeks (Member)

09 June 08  
Date

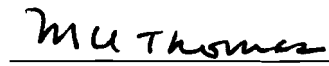
  
Heidi R. Ries (Member)

10 Jun 08  
Date

  
James A. Fellows (Member)

11 JUN 08  
Date

Accepted:

  
Marlin U. Thomas  
Dean, Graduate School of  
Engineering and Management

12 Jun 08  
Date

## Abstract

AlGaIn/GaN Heterostructure Field Effect Transistors (HFETs) have attracted radiation effects research interest due to their potential use in high power and high frequency space applications. Some of these applications involve the integration of GaN-based HFETs into satellite systems required to operate in earth orbit for years in a radiation environment at widely varying temperatures.

In this study, AlGaIn/GaN Heterostructures were irradiated at low temperature and the temperature dependent changes to drain current, gate current, capacitance, and gate conductance were measured. The results were compared to the charge control model of the drain current and trap-assisted tunneling model of the gate current to determine the source of the radiation-induced changes in these properties. AlGaIn/GaN HFETs were generally hardened to radiation effects compared to silicon and gallium arsenide based devices. The HFETs continued to function as transistors after radiation fluences of up to  $10^{14}$  0.45 MeV electrons/cm<sup>2</sup> or  $10^{13}$  1.0 MeV(eq) neutrons/cm<sup>2</sup>.

AlGaIn/GaN HFETs were susceptible to threshold voltage shifts and changes to drain currents after irradiation. After electron and neutron irradiation applied at ~80 K, measurement of the drain current at this temperature without warming showed an increase in the current that saturated after  $10^{13}$  electrons/cm<sup>2</sup> or  $10^{10}$  neutrons/cm<sup>2</sup>. This low-temperature increase in drain current and negative threshold voltage shift after irradiation is attributed to positive charge in the AlGaIn layer. The effect anneals after warming to room temperature as the positive charge is neutralized.

Measurement at room temperature after low-temperature irradiation shows a decrease in drain current. The positive charges that cause the low-temperature increase become mobile as the temperature increases and result in charged defects along the AlGa<sub>N</sub>-Ga<sub>N</sub> interface. These charged defects decrease the mobility in the 2DEG and hence decrease the current. This drain current reduction does not anneal at room temperature as these defects are persistent.

AlGa<sub>N</sub>/Ga<sub>N</sub> HFET gate leakage currents increase after low temperature irradiation. The increased gate current again saturated with additional electron and neutron irradiation above  $10^{13}$  electrons/cm<sup>2</sup> or  $10^{10}$  neutrons/cm<sup>2</sup>. Below  $10^{10}$  neutrons/cm<sup>2</sup> the increase was not observed. The increase was present throughout the temperature range of 80 K to 300 K and was persistent after room temperature annealing. The increased gate leakage current is attributed to trap-assisted tunneling. The saturation after a relatively low level of irradiation indicates that the defects are based on the complexing of gallium, nitrogen, and/or aluminum defects with an impurity element in the AlGa<sub>N</sub>. The impurity is of limited quantity in the AlGa<sub>N</sub> and therefore limits the growth of additional defects. Oxygen is the most likely impurity that is the source of this complexing behavior.

The source of the increase in the gate leakage current was modeled using the trap-assisted tunneling (TAT) model. The TAT model was applied to an optimization algorithm to determine which of the variables of the model was the source of increased TAT. Application of the model to post-irradiation vs. pre-irradiation data showed that the dominant parameter change that results in increased gate current was an increase in trap concentration,  $N_t$ .

## Acknowledgments

I have been helped and influenced by many wonderful people during my work on this dissertation. I was deployed to Iraq for a year in the middle of this research and the understanding and encouragement I received was truly remarkable. I would like to acknowledge the assistance and support that I've received from a number of diverse people and groups.

This work was partially supported by the following Defense Department organizations: the Defense Threat Reduction Agency, the Air Force Office of Scientific Research, and the Air Force Research Laboratory, Space Vehicles Directorate. Each of these organizations was a source of material support and encouragement. They are wholly committed to academic freedom through the non-intrusive but supportive manner in which they support this and other research programs.

The support I received from the non-AFIT radiation facilities that I used here in Ohio during this research was outstanding. Dr. Gary Farlow of Wright State University and Mr. Joe Talnagi and Mr. Andrew Kaufmann of The Ohio State University were always professional, knowledgeable, and encouraging. They are great partners for AFIT. I always felt that their concern for my research was real and their facilities were run with high standards and a focus on the customer.

My committee members have been very helpful and gracious during the extended time it took for me to complete this dissertation. They were very understanding of the change in circumstances that pulled me away for a year. They then supported me upon my return and helped me to get back on track and bring this work to fruition.

The Physics Department Head, Dr. Robert Hengehold, was also very supportive of my deployment. He understood both the needs of the Army and my commitment to military service. Upon my return he was always encouraging and interested in my progress and willing to help me overcome any obstacles to successful completion.



Mr. Eric Taylor, the nuclear engineering laboratory technician, was always professional and helpful. He was always supportive of my work as I took it in different directions that required a short-notice response to new requirements. Both he and the AFIT machine shop staff, led by Mr. Jan LeValley, were always available to provide outstanding professional service and advice.

The other PhD students and many of the MS students at AFIT were an incredible source of encouragement, technical excellence, and professionalism. Diverse students from many classes stretching from the class of 2003 to the class of 2010 were instrumental in helping me through this research. I would like to single-out individuals for their unique support but I'm afraid that if I do so I would miss someone. So I would like to acknowledge them as a group, if I hadn't had their support I would never have finished, or even started, this research.

By far the most influential contributor to my technical success and professional development was my advisor, Dr. Jim Petrosky. I have worked with Jim since the early 90's. I knew that Jim was an outstanding Army officer, nuclear engineer, and a great friend. But when I began this program, I did not truly understand the depth of his technical knowledge, his commitment to the development of students, and his leadership and integrity. It is impossible for me to imagine completing this research without his constant support. This dissertation and the research findings contained within are as much due to his fine work as to my struggles in following through on his insights.

My most heartfelt thanks are reserved for my family. My sons have always been supportive of my work. My wife has been an incredible source of encouragement. She has been a tremendous wife and partner for over 20 years. In particular she has been steadfast in her support over the past four years through my year-long deployment and through many doubts as I continued in this research. Her patience with me and her commitment to my work have been truly extraordinary.

John W. McClory

# Table of Contents

	Page
Abstract .....	iv
Acknowledgments .....	vi
Table of Contents .....	viii
List of Figures .....	x
List of Tables .....	xvi
I. Introduction .....	1
1.1 Focus of Research .....	2
1.2 Outline of Dissertation .....	4
II. Heterostructure Theory .....	7
2.1 Material Considerations .....	7
2.2 Two-Dimensional Electron Gas Formation .....	10
Carrier Concentration .....	14
Mobility .....	16
2.3 The Effect of Passivation .....	17
III. Model for Radiation Effects .....	19
3.1 Electron Non-ionizing Energy Loss .....	19
3.2 Neutron Non-ionizing Energy Loss .....	24
3.3 Defects in GaN and AlGaN .....	25
3.4 Radiation Effects on AlGaN/GaN Devices .....	29
Experimental Studies (Protons) .....	30
Experimental Studies (Gammas) .....	35
Experimental Studies (Neutrons) .....	36
3.5 The Trap-Assisted Tunneling Model .....	37
3.6 The Transistor Current Model .....	42
IV. Experimental Procedures .....	46
4.1 Device Preparation .....	47
4.2 Data Collection .....	51
Pre-irradiation Characterization .....	52
Neutron Irradiation Equipment .....	54
Electron Irradiation Equipment .....	59
4.3 Irradiations .....	61

	Page
4.4 Modeling Optimization Procedure.....	69
V. Experimental Results .....	72
5.1 Electron Irradiation Results .....	74
5.2 Neutron Irradiation Results.....	79
Pre-Irradiation Measurements.....	79
First Neutron Irradiation Experiment.....	88
Second Neutron Irradiation Experiment .....	95
5.3 Modeling Results .....	114
VI. Analysis and Discussion .....	123
6.1 Irradiation Effect on Drain Current.....	129
6.2 Irradiation Effect on Gate Leakage Current.....	136
Increased Gate Leakage and the TAT Model .....	137
6.3 Irradiation Effect on Capacitance .....	140
6.4 Device Design to Mitigate Radiation Effects .....	143
VII. Conclusions .....	145
Bibliography .....	151

# List of Figures

Figure	Page
1. Cross section of a typical $\text{Al}_x\text{Ga}_{1-x}\text{N}$ /GaN HFET [1].....	11
2. Energy bands in an $\text{Al}_x\text{Ga}_{1-x}\text{N}$ /GaN heterostructure showing the first two energy subbands in the quantum well and both the neutral (closed circles) and ionized (open circles) impurities in the $\text{Al}_x\text{Ga}_{1-x}\text{N}$ [14]. .....	12
3. ( a) The energy band diagram (from left-to-right) of the Schottky metal, the AlGaIn layer, and the GaN layer. The $\chi$ 's represent the electron affinity of the two semiconductors. (b) Energy bands in an AlGaIn/GaN HFET after formation showing the Schottky barrier at the metal-AlGaIn interface and the 2DEG at the AlGaIn-GaN interface.....	13
4. Maximum energy transfer for Ga and N as a function of the incident electron energy. The average and minimum displacement energies for both Ga and N are shown as horizontal lines. Values are calculated with Equation (11) [27].....	21
5. Electron stopping powers as calculated by XGEN for materials of interest [31]. .....	23
6. Dose deposition profiles for GaN (2 $\mu\text{m}$ ) on $\text{Al}_2\text{O}_3$ (1 mm) for particle energies of 0.5, 1.0, and 1.5 MeV. Calculation was performed using 200,000 histories in 20 batches in TIGER [31]. .....	23
7. EPR spectrum of an HFET after 1.0 MeV electron irradiation with a fluence of $1 \times 10^{16} \text{ cm}^{-2}$ . The carbon vacancy and the carbon in a silicon position antisite defects are clearly visible. ....	28
8. Common-source drain current as a function of gate voltage and transconductance of the same transistor pre-irradiation (solid line), post- $10^{12} \text{ cm}^{-2}$ fluence (dashed line), and post- $5 \times 10^{13} \text{ cm}^{-2}$ fluence (dotted line) [45]. .....	31
9. Transconductance vs. gate-source voltage for AlGaIn/AlN/GaN HEMTs before and after 1.8 MeV proton irradiation with fluences from $10^{13} \text{ cm}^{-2}$ to $10^{15} \text{ cm}^{-2}$ [49] .....	33
10. Normalized mobility and 2DEG sheet density from room temperature Hall Effect measurements [51]. .....	34
11. Transfer characteristics for AlGaIn/GaN HEMTs before and after 1.8-MeV proton irradiation at different fluences [52]. .....	35
12. Band diagram of the AlGaIn/GaN heterostructure.....	37
13. Trap-assisted tunneling through the Schottky barrier.....	39

Figure	Page
14. Band diagram of conduction band edge from the Schottky metal contact through the AlGa <sub>N</sub> layer to the GaN bulk showing the potentials used in the discussion. ....	41
15. Energy band diagram of an unpassivated HFET using Davinci showing the relative heights and widths of the two barriers at the metal-AlGa <sub>N</sub> and AlGa <sub>N</sub> -GaN interfaces. ....	42
16. Heterostructure layer composition showing the location of contacts to be added during HFET fabrication. ....	46
17. Photograph of a reticle showing the HFET structures used in this research. ....	47
18. Top view of the FATFET used in the irradiation experiments showing the cross section line depicted in Figure 19. ....	48
19. Cross section of the device used in the irradiation experiments. ....	49
20. Diced and packaged reticle ready for experimental testing. ....	50
21. Detail of the wire connection to the gate, source, and drain of the FATFET on the reticle chip. ....	50
22. Configuration of OSURR reactor and irradiation chamber [66]. ....	55
23. Aluminum fin used for mounting samples in neutron flux from the reactor. ....	56
24. Absorption cross section of cadmium. ....	57
25. Irradiation chamber neutron flux profile. ....	57
26. Neutron spectrum inside the cryostat. ....	58
27. Van de Graaff facility at Wright State University [65]. ....	60
28. Cold head and mounting assembly used in the Van de Graaff accelerator [27]. ....	60
29. Optimization sequence for application of the TAT model to measured data. ....	71
30. The pre- and post-irradiation measurements of sample A08 showing the increase in both $I_{\text{drain}}$ (a) and $I_{\text{gs}}$ (b) following irradiation. The curve for $V_{\text{gs}} = -1\text{V}$ is shown with and without $I_{\text{gs}}$ . The irradiation and measurements were performed at liquid nitrogen temperatures ( $\sim 85\text{K}$ ). ....	75
31. The pre- and post-irradiation measurements of sample A09 following several measurement and irradiation cycles. The irradiation and measurements were performed at $\sim 80\text{K}$ . $I_{\text{gs}}$ was subtracted from all curves in Figure 31(a). ....	77

Figure	Page
32. The pre- and post-irradiation measurements of sample A09 at RT following several measurement and irradiation cycles. The irradiations were performed at ~85 K. $I_{gs}$ was subtracted from all curves in Figure 32(a). $I_{ds}$ has returned to its pre-irradiation value. Figure 32(b) shows a persistent increase following irradiation and warming to RT. ....	78
33. Pre- and post-irradiation capacitance-voltage measurements of HFET A01 recorded at ~80 K following exposure to a fluence of $3.5 \times 10^{12} \text{ e}^- / \text{cm}^2$ with 0.45 MeV electrons. ....	79
34. Pre-irradiation I-T curves at three gate voltages over the temperature range of 84-294K for HFET JM18.....	80
35. Pre-irradiation I-T curves for unpassivated (a) and passivated (b) HFETs at a gate voltage of -4V. ....	81
36. Average pre-irradiation I-T curves for unpassivated and passivated HFETs at a gate voltage of -4V showing the 80% increase in gate current with passivation. ....	82
37. Multiple gate voltage vs. temperature sweeps of an HFET to determine the variation with repeated cooling and heating. The cycles in the legend are listed in chronological order. ....	84
38. Average of the gate voltage versus temperature sweeps in Figure 37, not including the first sweep, with error bars of one standard deviation in the data. ....	84
39. Gate current versus gate voltage at five different temperatures for an unpassivated HFET.....	85
40. Gate current versus gate voltage at five different temperatures for a passivated HFET. ....	85
41. Drain-to-source current versus drain-to-source voltage at three different gate voltages and temperatures of 80 and 300 K for an unpassivated HFET. ....	86
42. Drain-to-source current versus drain-to-source voltage at three different gate voltages and temperatures of 80 and 300 K for a passivated HFET. ....	87
43. Capacitance versus gate voltage at temperatures of 80 and 300 K for passivated and unpassivated HFETs. ....	88
44. Experimental procedure of the first neutron irradiation experiment showing irradiations, measurements, and temperature profile.....	89
45. Temperature dependent $I_{gs}$ before and after neutron irradiation.....	90

Figure	Page
46. HFET transistor curves measured at 80 K before and after neutron irradiation at 84 K. .....	91
47. HFET transistor curves measured at 294 K before and after neutron irradiation at 84 K.....	91
48. Temperature dependent $I_{gs}$ before and after neutron irradiation and after a one-week room-temperature anneal. ....	92
49. HFET transistor curves measured at 80 K before and after neutron irradiation at 84 K and after a three-week room-temperature anneal.....	93
50. HFET transistor curves measured at 294 K before and after neutron irradiation at 84 K and after a three-week room-temperature anneal.....	93
51. C-V measurements at high frequency (1 MHz) at room-temperature and 80K, following irradiation at 84 K, and a 3-week room-temperature anneal. ....	94
52. Experimental procedure of the second neutron irradiation experiment showing irradiations, measurements, and temperature profile.....	96
53. Temperature dependent $I_{gs}$ before and after neutron irradiation for an unpassivated and a passivated HFET. ....	97
54. HFET transistor curves measured at 80 K before and after neutron irradiation at 84 K for an unpassivated and a passivated HFET. ....	98
55. HFET transistor curves measured at 300 K before and after neutron irradiation at 84 K for an unpassivated and a passivated HFET. ....	100
56. HFET capacitance vs. voltage curves measured at 80 K before and after neutron irradiation at 84 K for an unpassivated and a passivated HFET. The threshold voltage shift is more apparent in the unpassivated HFET. ....	101
57. HFET capacitance vs. voltage curves measured at 300 K before and after neutron irradiation at 84 K for an unpassivated and a passivated HFET. The threshold voltage shift is more apparent in the unpassivated HFET. ....	102
58. HFET gate conductance vs. voltage curves measured at 80 K before and after neutron irradiation at 84 K for an unpassivated and a passivated HFETs. The shift in the peak gate conductance is more apparent in the unpassivated HFET.....	103

Figure	Page
59. HFET gate conductance vs. voltage curves measured at 300 K before and after neutron irradiation at 84 K for an unpassivated and a passivated HFETs. The shift in the peak gate conductance is more apparent in the unpassivated HFET. The peak level is substantially reduced in the unpassivated HFET but slightly increased in the passivated HFET.....	104
60. Temperature dependent $I_{gs}$ before and after neutron irradiation and after one- and four-week room-temperature anneals for unpassivated and passivated HFETs. ....	105
61. HFET transistor curves measured at 80 K before and after neutron irradiation at 84 K and after one- and four-week room-temperature anneals for unpassivated and passivated HFETs. ....	106
62. HFET transistor curves measured at 300 K before and after neutron irradiation at 84 K and after one- and four-week room-temperature anneals for unpassivated and passivated HFETs. ....	107
63. HFET capacitance vs. voltage curves measured at 80 K before and after neutron irradiation at 84 K and after one- and four-week room-temperature anneals for unpassivated and passivated HFETs. ....	109
64. HFET capacitance vs. voltage curves measured at 300 K before and after neutron irradiation at 84 K and after one- and four-week room-temperature anneals for unpassivated and passivated HFETs. ....	110
65. HFET gate conductance vs. voltage curves measured at 80 K before and after neutron irradiation at 84 K and after one- and four-week room-temperature anneals for unpassivated and passivated HFETs. ....	112
66. HFET gate conductance vs. voltage curves measured at 300 K before and after neutron irradiation at 84 K and after one- and four-week room-temperature anneals for unpassivated and passivated HFETs. ....	113
67. Pre-irradiation gate leakage current vs. temperature at a fixed voltage and gate leakage current vs. voltage at a fixed temperature for an unpassivated HFET. The data with error bars is displayed along with the best fit using the TAT model.....	115
68. Pre-irradiation gate leakage current vs. temperature at a fixed voltage and gate leakage current vs. voltage at a fixed temperature for a passivated HFET. The data with error bars is displayed along with the best fit using the TAT model.....	116
69. Pre- and post-irradiation gate leakage current vs. temperature at a gate voltage of -4 V for unpassivated HFETs. Each of the four parameters of the model are varied independently from their pre-irradiation values in order to match the post-irradiation data. ....	118



Figure	Page
70. Pre- and post-irradiation gate leakage current vs. temperature at a fixed voltage and gate leakage current vs. voltage at a fixed temperature for an unpassivated HFET (JM110). The data is displayed along with the best fit using the TAT model.....	119
71. Pre- and post-irradiation gate leakage current vs. temperature at a fixed voltage and gate leakage current vs. voltage at a fixed temperature for an unpassivated HFET (JM41). The data is displayed along with the best fit using the TAT model.....	120
72. Pre- and post-irradiation gate leakage current vs temperature at a fixed voltage and gate leakage current vs. voltage at a fixed temperature for an passivated HFET (JM31). The data is displayed along with the best fit using the TAT model.....	121
73. Average $I_{gs}$ -T for all six unpassivated and passivated HFETs with $V_{gs} = -4$ V. Data from pre-irradiation, post-irradiation and after a four-week RT anneal measurements is shown. ....	124
74. Average $I_{ds}$ - $V_{ds}$ for all six unpassivated and passivated HFETs at 80 K with $V_{gs} = 2$ V. Data from pre-irradiation, post-irradiation and after a four-week RT anneal measurements is shown.....	126
75. Average $I_{ds}$ - $V_{ds}$ for all six unpassivated and passivated HFETs at 300 K with $V_{gs} = 2$ V. Data from pre-irradiation, post-irradiation and after a four-week RT anneal measurements is shown.....	127
76. HFET band diagram illustrating the formation of positive charge and traps during irradiation at 84 K. ....	133
77. HFET band diagram illustrating the movement of positive charge and the accumulation of donor-like defects near the AlGa <sub>N</sub> -Ga <sub>N</sub> interface during post-irradiation annealing at room temperature. ....	135
78. Average C- $V_g$ for all six unpassivated and passivated HFETs at 80 K with $V_{ds} = 0$ V. Data from pre-irradiation, post-irradiation and after a four-week RT anneal measurements is shown.....	141
79. Average C- $V_g$ for all six unpassivated and passivated HFETs at 300 K with $V_{ds} = 0$ V. Data from pre-irradiation, post-irradiation and after a four-week RT anneal measurements is shown. ....	142

## List of Tables

Table	Page
1. Selected Physical Properties of GaN and AlN at T = 300 K (from [8]and included references).....	9
2. Maximum Energy Transferred to AlGaN Atomic Constituents for Given Electron Energies .....	20
3. Material Parameters Used for Dose Calculations [8] .....	22
4. Defects in Gallium Nitride.....	27
5. Relevant Results in Radiation Effects on AlGaN/GaN HFETs.....	36
6. Electron Irradiation Experiment Summary.....	61
7. First Neutron Experiment Irradiations Summary .....	63
8. First Neutron Experiment Measurements Summary .....	64
9. Second Neutron Experiment Irradiations Summary.....	66
10. Second Neutron Experiment Measurements Summary.....	67
11. Modeling Results Pre- and Post-Irradiation .....	122
12. Low Temperature Parametric Changes Following Neutron Irradiation .....	138

# THE EFFECT OF RADIATION ON THE ELECTRICAL PROPERTIES OF ALUMINUM GALLIUM NITRIDE/GALLIUM NITRIDE HETEROSTRUCTURES

## I. Introduction

The study of III-V semiconductor materials is of interest to the Department of Defense due to their potential military applications. Specifically, gallium nitride (GaN) based semiconductor devices demonstrate attractive material properties including, 1) high temperature operation due to the wide bandgap, 2) high frequency operation due to the high electron velocity, and 3) high power density due to the wide bandgap and high field in the material [1]. Devices based on materials with these properties are attractive candidates for military applications such as sensors and communications platforms that require high-power applications at microwave frequencies. The aluminum gallium nitride/gallium nitride Heterojunction Field Effect Transistor (AlGaN/GaN HFET) is a prime candidate for these purposes. Additionally, GaN and related III-nitride alloys have emerged as the leading materials for many optoelectronic devices operating in the blue to ultra-violet spectrum.

Devices used in this study will operate in the space environment, which makes radiation resistance a priority feature. The use of these devices in space-based systems requires a detailed understanding of the effect of radiation on their operational characteristics. The space radiation environment includes long-term exposure to

electrons, protons, alpha particles, and heavy ions. In this research we used neutrons and electrons to induce displacement damage effects for comparison to proton and electron induced effects in previous studies.

Previous research has determined that gallium nitride based materials are relatively radiation tolerant compared to other semiconductor materials [2]. However, the effect of radiation, particularly neutrons, has not been sufficiently tested on these devices. Device characterization after irradiation is important for determining what effect the radiation environment in space will have on operation and reliability. Characterization using radiation defects additionally helps to probe the device physics, specifically defect formation and the interaction of those defects with the component materials.

## ***1.1 Focus of Research***

The objective of this work is to:

1. Experimentally measure the effect of irradiation on the electrical properties of AlGaIn/GaN HFETs.
2. Compare the experimental results to the output of a physics-based model of the devices.
3. Attribute these results to the interaction of radiation with the HFET component materials and the subsequent motion and interaction of radiation induced defects in the HFET.

The theory of radiation interaction and the resulting changes to device operation is supported by experimentation using neutrons and electrons and the modeling of device physics. A greater understanding of radiation effects will lead to better techniques for hardening devices. Additionally, understanding of radiation effects can lead to

improvements in material growth techniques, device construction geometries, and the maximization of desirable device characteristics.

This research specifically explored the effect of irradiation on the transistor currents and the gate leakage current of AlGa<sub>N</sub>/Ga<sub>N</sub> HFETs. The research was based on the following principles:

- Changes to the electrical properties of AlGa<sub>N</sub>/Ga<sub>N</sub> HFETs after irradiation can be linked to radiation-induced defects in its constituent materials.
- Post-irradiation change in the drain-to-source current can be attributed to defects in the AlGa<sub>N</sub> layer causing changes to the electron concentration and mobility of the Two-Dimensional Electron Gas (2DEG) in the channel.
- Post-irradiation change in the gate leakage current can be attributed to defects in the AlGa<sub>N</sub> layer resulting in changes to the trap-assisted tunneling process.
- Device growth and construction can enhance or mitigate these radiation induced effects.

The results of this research are in the following published, or soon to be published, documents:

1. An Analysis of the Effects of Low-Energy Electron Irradiation of AlGa<sub>N</sub>/Ga<sub>N</sub> HFETs [3].
2. The Temperature Dependent Electrical Characteristics of Neutron Irradiated AlGa<sub>N</sub>/Ga<sub>N</sub> HFETs [4].
3. Trap-Assisted Tunneling Induced Currents in Neutron Irradiated AlGa<sub>N</sub>/Ga<sub>N</sub> HFETs [5].

4. The Application of an Analytical Trap-Assisted Tunneling Model to the Voltage and Temperature Dependent Electrical Characteristics of AlGaN/GaN HFETs.
5. The Effect of SiN Passivation on the Modeling of the Gate Leakage Current in AlGaN/GaN HFETs.

## **1.2 Outline of Dissertation**

Chapter 2 describes the physics of AlGaN/GaN heterostructures and the effect of various growth and construction techniques. The relevant material parameters of AlGaN and GaN are described. Device construction techniques are linked to their effect on device operation. The physics of the formation of the 2DEG is described in terms of the material parameters and device construction. Finally the effect of passivation on device characteristics is explored.

Chapter 3 explains the model for radiation effects used in this research. The interaction of energetic particles with the device material layers is described. The results of previous device level studies and how they relate to this research is explained. Defect studies on AlGaN and GaN that are relevant to the observed changes in electrical characteristics are cataloged. Understanding these defects is crucial to the development of the radiation effects models employed later in the analysis of the experimental results. The relationship between these defects to the experimentally observed post-irradiation measurements described in the experimental results chapter is crucial to understanding the potential techniques to induce radiation hardness.

Chapter 3 also contains a description of the applicable models and how these models are applied to the experimental results. It first describes the model of 2DEG formation and the resulting channel or transistor current. The 2DEG model is based on

material configuration of the AlGaN epi-layer and at the metal and GaN interfaces. Radiation induced changes in the AlGaN layer and at the interface are interpreted in terms of this model in the Analysis chapter. Chapter 3 also contains a description of the possible sources of the gate leakage current through the AlGaN epi-layer. It contains a detailed analysis of the analytical trap-assisted tunneling (TAT) model after rejection of alternate leakage mechanisms.

Chapter 4 describes the experimental techniques used in each of the experimental rounds of irradiation and measurement. The construction of the wafer from which the devices are built, the masking procedure used to construct the devices, and the wiring of the experimental devices in order to make them accessible to the experimental apparatus is detailed. The equipment and controls designed for the irradiation and measurement procedures is described. This includes both the relevant hardware and software and how it was employed. The operation of the radiation facilities and the integration of the devices into the irradiation environment are explained. The data collection procedures and why those procedures were applied are laid out in detail. The method of application of the trap-assisted tunneling model to the experimental results is described. Finally, the irradiations that the devices received are laid out in detail.

Chapter 5 presents the results of both the experimental measurements as well as radiation effects modeling. The experimental results of multiple irradiations and measurement cycles are described. The systemic error in the measurement system and its causes are determined. The experimental results include two electron irradiation experiments carried out by other researchers and two separate neutron irradiation experiments conducted at the Ohio State University Research Reactor (OSURR). The

modeling results demonstrate the application of the TAT model to both the pre- and post-irradiation experimental results.

Chapter 6 contains an analysis of the results presented in Chapter 5 and a discussion of their meaning with respect to device operation after irradiation. Physical models that link defects in the AlGa<sub>N</sub> layer to observed changes in the electrical characteristics after irradiation are proposed. The results of experimental measurements are compared to the results of applying the models. This comparison is explained in the context of the developed physical models. Initial recommendations on device design are proposed.

Chapter 7 offers a conclusion to the work. It provides a summary of the findings in this study. Recommendations for future work are also offered.



## II. Heterostructure Theory

The focus of this research is the  $\text{Al}_x\text{Ga}_{1-x}\text{N}/\text{GaN}$  heterostructure constructed as a Heterojunction Field Effect Transistor (HFET). Heterojunctions in general are an interface composed of two layers of different semiconductor materials. The differing bandgaps of the two materials can lead to unique physical properties that can be exploited for a particular application. In the  $\text{AlGaN}/\text{GaN}$  heterojunction the interface between  $\text{AlGaN}$  and  $\text{GaN}$  is exploited for its unique properties. The  $\text{Al}_x\text{Ga}_{1-x}\text{N}$  layer is an alloy of aluminum nitride ( $\text{AlN}$ ) and  $\text{GaN}$  with aluminum molar fraction given by  $x$ . The HFET includes a Schottky gate contact and ohmic source and drain contacts that enable operation of the heterojunction as an electrical circuit element. This chapter describes the relevant physics of the  $\text{Al}_x\text{Ga}_{1-x}\text{N}/\text{GaN}$  HFET.

### 2.1 Material Considerations

Gallium nitride is a wide bandgap semiconductor that exists in both the wurtzite and zincblende crystal structure. The devices studied, and all devices currently constructed for applications, use the wurtzite structure. Because of the wide bandgap the intrinsic carrier concentration  $n_i$  of  $\text{GaN}$  is essentially zero at  $T = 300$  K and  $n_i$  remains small enough so as to have a negligible effect on the operation of most devices until  $T \approx 1000$  K. This property makes this wide bandgap material suitable for use in high temperature environments since the carrier concentration will depend only on the doping level (the extrinsic region) throughout a wide temperature range. The wide bandgap of  $\text{GaN}$  also makes the material resistant to electrical breakdown in high electric fields. The breakdown field strength of  $\text{GaN}$  is approximately 10 times higher than that of gallium

arsenide (GaAs) and silicon (Si) [6]. GaN also has an electron saturation velocity more than 2 times greater than that of GaAs and Si [7]. The high breakdown field and electron velocity make GaN an excellent material for high-power and high-frequency electronic devices.

Aluminum nitride has an identical wurtzite structure to GaN, with the gallium atoms replaced with aluminum atoms. The smaller radii of the aluminum atoms results in a smaller lattice constant and an even wider bandgap in AlN than in GaN.  $\text{Al}_x\text{Ga}_{1-x}\text{N}$  is an alloy where a percentage of the gallium atoms have been replaced with aluminum atoms. The lattice constant and bandgap of  $\text{Al}_x\text{Ga}_{1-x}\text{N}$  are at interim levels between those of GaN and AlN. Table 1 lists selected material parameters for GaN and AlN. The junction of GaN with AlGaN and the resulting discontinuities in lattice constant and bandgap result in the desired features of the AlGaN/GaN heterostructure as described in the subsequent paragraphs.

An expression for the bandgap of AlGaN as a function of temperature is necessary for applying the models used in this research. Vegard's law [9] determines some parameter values in  $\text{Al}_x\text{Ga}_{1-x}\text{N}$  for a given aluminum mole fraction  $x$ . Vegard's law is an approximate empirical rule that provides a linear relationship between lattice constant of an alloy and its constituent compounds. It can be expressed as

$$\Gamma(\text{Al}_x\text{Ga}_{1-x}\text{N}) = x\Gamma(\text{AlN}) + (1-x)\Gamma(\text{GaN}) \quad (1)$$

when applied to GaN and AlN, where  $\Gamma$  represents any physical parameter for which the relation holds. Vegard's equation is an approximation that holds for certain types of parameters and is specifically developed for the lattice constant. Hence Vegard's law can be used to determine the lattice constant of AlGaN at various aluminum mole fractions.

Table 1. Selected Physical Properties of GaN and AlN at T = 300 K (from [8] and included references).

Property (units)	Symbol	GaN Value	AlN Value
Energy Gap (eV)	$E_g$	3.39	6.1
Density (g/cm <sup>3</sup> )	$\rho$	6.15	3.23
Electron Affinity (eV)	a	4.1	0.6
Static Dielectric Constant (8.854 x 10 <sup>-14</sup> F/cm)	$\epsilon_r$	8.9	8.5
Lattice Constant (Å)	a	3.189	3.11
Lattice Constant (Å)	c	5.186	4.98
Electron Effective Mass ( $m_o$ )	$m_{eff}$	0.20	0.4
Electron mobility, bulk (cm <sup>2</sup> /V·sec)	$\mu_n$	>1000	300
Hole mobility, bulk (cm <sup>2</sup> /V·sec)	$\mu_p$	>200	14
Saturation Velocity (cm/s)	$v_{sat}$	2.5x10 <sup>7</sup>	1.4x10 <sup>7</sup>
Breakdown Field (V/cm)	$F_b$	~5x10 <sup>6</sup>	~1x10 <sup>6</sup>

The bandgap ( $E_g$ ) is one parameter that warrants analysis beyond Vegard's law. A quadratic term in  $x$  is added to Vegard's law that includes a bowing parameter,  $b$ . The equation for the bandgap for Al<sub>x</sub>Ga<sub>1-x</sub>N becomes [10]

$$\Gamma(\text{Al}_x\text{Ga}_{1-x}\text{N}) = x\Gamma(\text{AlN}) + (1-x)\Gamma(\text{GaN}) - bx(1-x) \quad (2)$$

where  $b$  has the same units as  $\Gamma$ . In the case of the bandgap in Al<sub>x</sub>Ga<sub>1-x</sub>N, the reported bowing parameters have ranged from  $b = 0$  [11] (no bowing) to  $b = 1.3$  eV [12], so equation (2) can not be applied with much certainty. The temperature dependence of  $E_g$  is given by the Varshni equation as

$$E_g(T) = E(0) - \frac{\alpha T^2}{(T + \beta)}. \quad (3)$$

In GaN,  $\alpha = 7.7 \times 10^{-4}$  eV/K and  $\beta = 600$  K determined empirically, and  $E(0) = 3.47$  eV [8]. In AlN,  $\alpha = 1.8 \times 10^{-3}$  eV/K,  $\beta = 1462$  K, and  $E(0) = 6.2$  eV [8]. In the devices of this research,  $x = 0.27$ , and the bandgap narrowing with temperature is needed for the development of the models used. The resulting Varshni equation for  $\text{Al}_{0.27}\text{Ga}_{0.73}\text{N}$  is

$$E_{g(\text{AlGa}_N, x=0.27)}(T) = 3.983 - \frac{6.24 \times 10^{-4} T^2}{(T + 525)} \quad (4)$$

extrapolated from equations (2) and (3) using an average bowing parameter of 1 eV based on the range of bowing parameters described above.

## 2.2 Two-Dimensional Electron Gas Formation

Figure 1 shows the structure of a basic  $\text{Al}_x\text{Ga}_{1-x}\text{N}/\text{GaN}$  HFET. The metal-AlGaN contact labeled *GATE* is a Schottky contact and the contacts labeled *SOURCE* and *DRAIN* are ohmic contacts. The AlGaN layer is normally a thin epi-layer on the order of tens of nanometers thick. The GaN layer is on the order of a micron to a few microns thick. The substrate is from a near lattice matching material such as silicon carbide. When a bias voltage is applied to the source and drain contacts, current flows readily in the 2DEG channel. This channel has high mobility, especially when the GaN is undoped, as is the case in the HFETs used in this study. Upon application of a negative voltage to the gate contact, the 2DEG diminishes in proportion to the magnitude of the applied gate voltage until a threshold voltage ( $V_{\text{TH}}$ ) is reached at which current is no longer carried between a biased source and drain. The speed with which channel conduction can be switched on and off and the high source-drain bias voltages that can be supported make the AlGaN/GaN HFET well suited to high-frequency and high-power applications. The

demonstrated power performance of AlGaN/GaN HFETs is generally 6-10 times better than that of GaAs or InP HFETs up through 20 GHz [13].

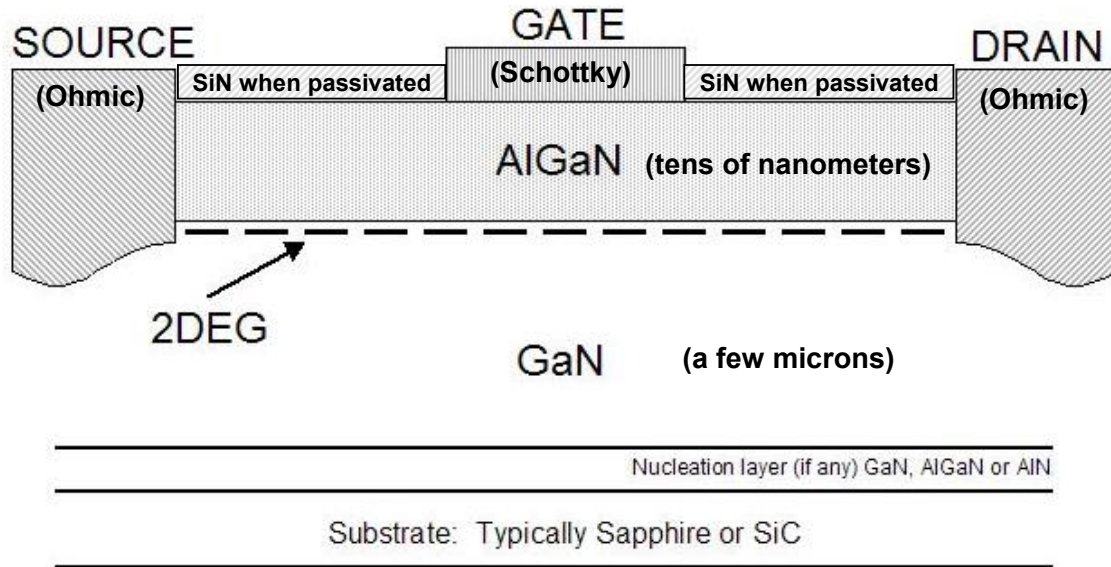


Figure 1. Cross section of a typical  $\text{Al}_x\text{Ga}_{1-x}\text{N}/\text{GaN}$  HFET [1].

The unique properties of the HFET are due to the formation of a 2DEG at the AlGaN-GaN interface. The bandgap discontinuity and the piezo-electric fields described below between the GaN and  $\text{Al}_x\text{Ga}_{1-x}\text{N}$  causes band bending along the interface. Under the right conditions, aluminum mole fraction, AlGaN layer width, etc., the band bending can result in the formation of 2DEG at the interface. The 2DEG is present at the interface when band bending results in a conduction band edge below the Fermi level. The 2DEG exists in the resulting quantum well formed parallel to the interface in the x-y plane as shown in Figure 2.

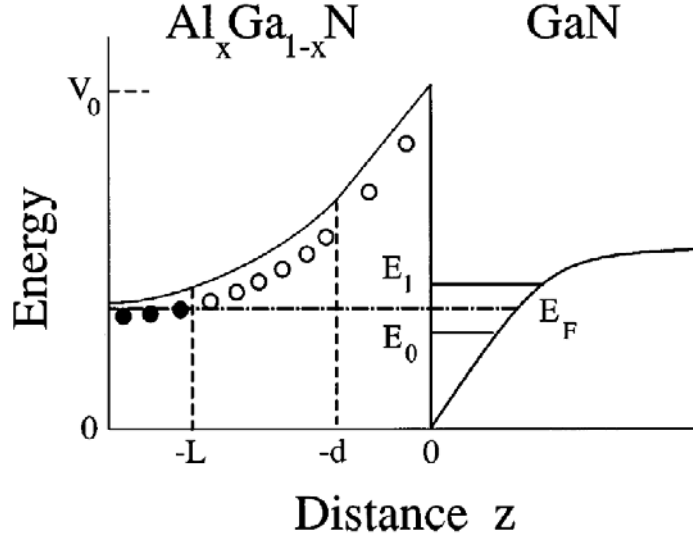


Figure 2. Energy bands in an  $\text{Al}_x\text{Ga}_{1-x}\text{N}/\text{GaN}$  heterostructure showing the first two energy sub-bands in the quantum well and both the neutral (closed circles) and ionized (open circles) impurities in the  $\text{Al}_x\text{Ga}_{1-x}\text{N}$  [14].

The band bending below the Fermi level can be due to a combination of the field produced from the piezoelectric polarization,  $P_{pz}$ , inherent in group III nitrides and the spontaneous polarization,  $P_{sp}$ , at the heterojunction of the two nitrides of differing ionicity [15]. The strain caused by the growth of the  $\text{Al}_x\text{Ga}_{1-x}\text{N}$  on GaN results in a total polarization given by [16]

$$P(x) = P_{pz} + P_{sp} \quad (5)$$

$$P(x) = -[(3 \cdot 2x - 1 \cdot 9x^2)x10^{-6} - 5 \cdot 2x10^{-6}x]C \cdot \text{cm}^{-2}$$

where  $x$  is the aluminum fraction. The ability to form a 2DEG is dependent on the aluminum content of the  $\text{Al}_x\text{Ga}_{1-x}\text{N}$  as well as the thickness of the  $\text{Al}_x\text{Ga}_{1-x}\text{N}$  layer. The field resulting from the polarization can be as high as 3-5 MV/cm.

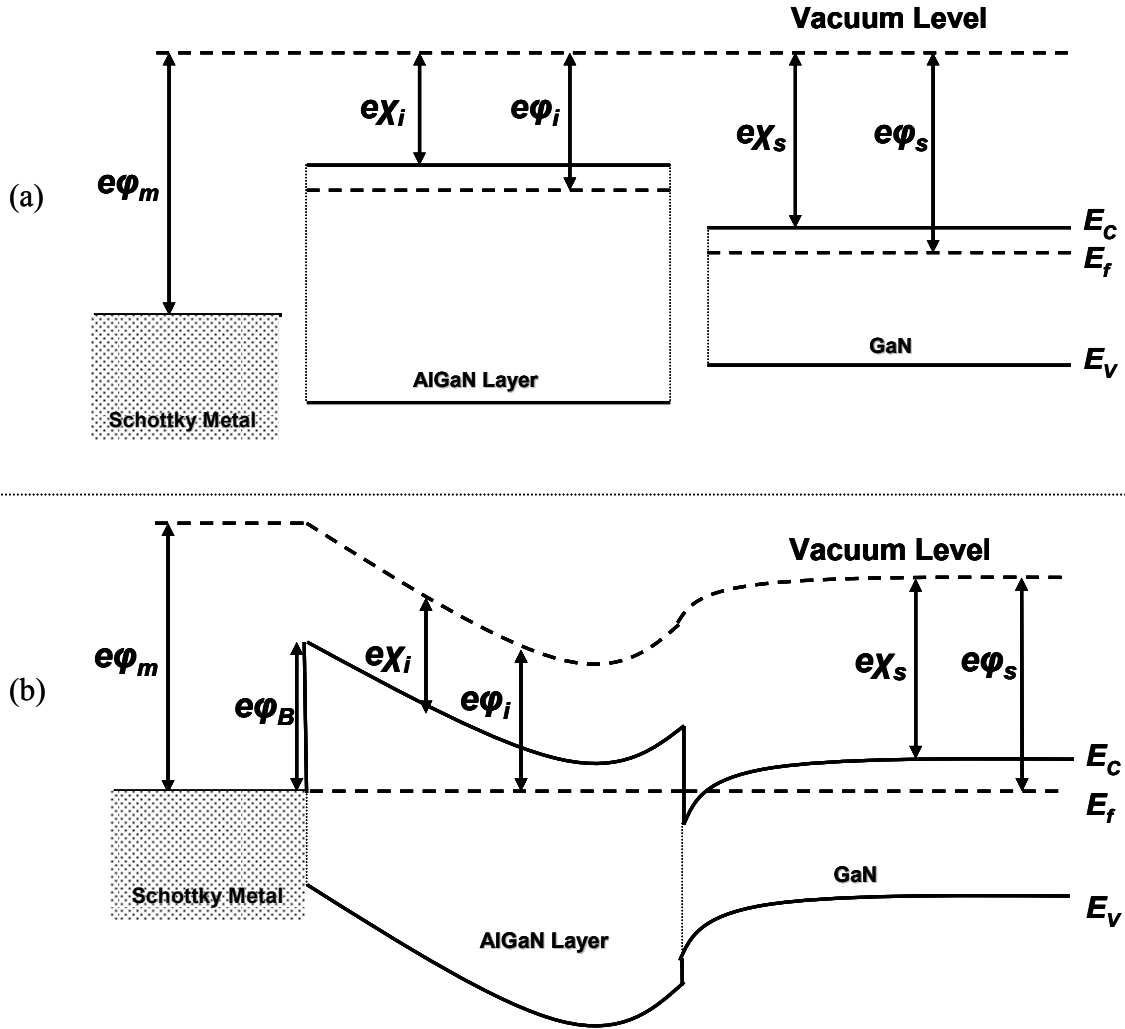


Figure 3. (a) The energy band diagram (from left-to-right) of the Schottky metal, the AlGaIn layer, and the GaN layer. The  $\chi$ 's represent the electron affinity of the two semiconductors. (b) Energy bands in an AlGaIn/GaN HFET after formation showing the Schottky barrier at the metal-AlGaIn interface and the 2DEG at the AlGaIn-GaN interface.

The complete heterostructure is formed with the Schottky metal gate deposited on the exposed AlGaIn surface. The band bending then consists of the alignment of the Fermi level from the gate metal through the AlGaIn layer to the GaN surface. The alignment of the Fermi levels together with the maintenance of the electron affinity for each of the semiconductor surfaces results in a well forming interface at the AlGaIn-GaN

boundary as well as the Schottky barrier interface at the metal-AlGa<sub>x</sub>N boundary. The bending of the energy bands in the formation of a HFET is shown in Figure 3.

The 2DEG has some properties that make it a unique channel for current flow in a field effect transistor arrangement. The triangular well formed between the conduction band edge of the interface and the conduction band edge of the GaN, shown in Figures 2 and 3(b), has a small width. The width is on the order of a Debroglie wavelength or a few nanometers. This gives the channel its two-dimensional nature. The electrons in the channel have high mobility; an order of magnitude or greater than in GaN, from a few hundred cm<sup>2</sup>/V-s in bulk GaN to a few thousand cm<sup>2</sup>/V-s in the 2DEG channel at room temperature [75]. The exact values depend upon growth technique, substrate material, GaN purity, AlGa<sub>x</sub>N layer thickness, etc. The higher mobility in the channel is due to the separation of the conduction electrons in the channel from their donor atoms in the GaN bulk. The high electron concentration and mobility in the well enable the desired features of the HFET, i.e. high-power density and high-frequency operation.

### **Carrier Concentration**

The electrons in the 2DEG are confined in the  $z$  direction by the quantum well formed as shown in Figure 2. The electrons in the well can have densities greater than  $10^{13}$  cm<sup>-2</sup> for heterostructures with aluminum fractions near 0.30 [1]. The electron density of the 2DEG in MBE grown Al <sub>$x$</sub> Ga<sub>1- $x$</sub> N/GaN heterostructures has been parameterized by the aluminum content [17]:

$$n_s(x) = n_0 + (5.45 \cdot 10^{13} \cdot \text{cm}^{-2})x \quad \text{for } 0.00 \leq x \leq 0.31. \quad (6)$$

The density of the gas is also dependent on the thickness of the AlGa <sub>$x$</sub> N layer and is included in the equation via the constant  $n_0$ .



But this parametric equation does not take into account the addition of defects in the component materials. For that a more complete derivation of the 2DEG carrier concentration is needed. In order to include changes to the carrier concentration from point defects, the development of Rashmi, *et al.* [18] is used. The polarization induced sheet charge density,  $\sigma(x)$ , is given by [16]

$$\sigma(x) = P_{sp}(AlGaN) - P_{sp}(GaN) + P_{pz}(AlGaN) - P_{pz}(GaN). \quad (7)$$

With this estimate of the sheet charge and the assumption that the 2DEG is formed in a triangular well with two available quantum states in the  $z$ -direction (as in Figure 2) one can solve for the carrier concentration.

A self-consistent solution of the Schrodinger and Poisson equations gives

$$n_s = \frac{4\pi m^* k_b T}{h^2} \ln \left[ \left( 1 + e^{\frac{E_F - E_0}{k_b T}} \right) \left( 1 + e^{\frac{E_F - E_1}{k_b T}} \right) \right]. \quad (8)$$

Assuming that the gate and interface depletion regions overlap, i.e. the total depletion approximation, then the total charge depleted from solving the Poisson equation in the AlGaN layer is

$$n_s = \frac{\varepsilon(x)}{qd} \left( V_{gs} - V_{TH}(x) - \frac{E_F}{q} \right) \quad (9)$$

where  $\varepsilon(x)$  is the dielectric constant in the AlGaN (a function of the Al fraction  $x$ ),  $d$  is the thickness of the AlGaN layer,  $V_{gs}$  is the gate bias, and  $V_{TH}$  is the threshold voltage. The threshold voltage is given by

$$V_{TH}(x) = \varphi_b(x) - \Delta\varphi_c(x) - \frac{qN_d d^2}{2\varepsilon(x)} - \frac{\sigma(x)}{\varepsilon(x)} \quad (10)$$

where  $\varphi_b$  is the Schottky barrier height,  $\Delta\varphi_c$  is the conduction band voltage difference between GaN and AlGaN, and  $N_d$  is the donor density in the AlGaN.

How can defects caused by irradiation induced displacement change the carrier concentration? The effect will be on the threshold voltage through: 1) changes in the effective Schottky barrier height by the addition of traps, and 2) changes in the polarization induced charge. In Chapter 3 this issue is revisited and mechanisms whereby point defects lead to shifts in the threshold voltage and hence the 2DEG carrier density are proposed.

## **Mobility**

One of the goals in the production of  $\text{Al}_x\text{Ga}_{1-x}\text{N}/\text{GaN}$  HFETs is the increased mobility possible in the 2DEG due to the isolation of the electrons in the gas from the ionized impurity sites responsible for scattering. However there are scattering centers in or near the 2DEG well that will still cause a reduction in mobility. The mechanisms of scattering include ionized impurities, alloy disorder, and acoustic and optical phonons [19]. All of these mechanisms are minimized in the 2DEG of the HFET to some degree leading to increased mobility of the electrons. The primary sources of scattering, and hence changes to the mobility, due to radiation damage-induced point defects are alloy disorder and coulomb scattering by charged impurities. Coulomb scattering by ionized centers in the GaN or along the heterojunction interface are more effective at limiting the electron mobility than impurities in the AlGaN [14]. The wavefunctions of the electrons in the 2DEG are confined mostly to the GaN side of the junction so the centers occupy the same space as the electrons.

Alloy disorder at the interface can be increased by electron irradiation. The irradiation can cause an increase in both the alloy disorder on the GaN and AlGaN sides of the interface. One of the issues investigated in this research is the formation of

aluminum displacements in the AlGa<sub>N</sub> leading to higher levels of alloy disorder near the interface and hence potentially decreased mobility.

### **2.3 The Effect of Passivation**

Spontaneous and piezoelectric polarization effects in the AlGa<sub>N</sub>/Ga<sub>N</sub> heterostructure result in a positive sheet charge in the AlGa<sub>N</sub> layer of the HFET [16]. A positive sheet charge at the AlGa<sub>N</sub>-Ga<sub>N</sub> interface is coupled with a negative sheet charge under the exposed AlGa<sub>N</sub> surface. In order for the 2DEG to form, the negative sheet charge under the surface must be neutralized by positive charge along the AlGa<sub>N</sub> exposed surface [20]. Ionized donor states along the exposed AlGa<sub>N</sub> surface provide this positive surface charge [21]. These donor-like states are AlGa<sub>N</sub> surface states along the exposed surface [22]. Trapping of electrons at this surface counteracts this positive charge leading to a decreased field in the 2DEG well and hence decreased electron concentration in the well and decreased transistor current. This manifests itself in a decreased threshold voltage and therefore device shut off at a lower reverse gate bias.

Surface passivation of the exposed AlGa<sub>N</sub> surface with a dielectric layer can help reduce the trapping of electrons by the surface donor states. Passivation with a silicon nitride (SiN) layer is typically applied to improve the performance of AlGa<sub>N</sub>/Ga<sub>N</sub> HFETs and was used in some of the HFETs irradiated and measured in this research. The effect of SiN passivation is not clear but a number of mechanisms have been proposed. The most widely accepted explanation is that passivation reduces the surface trap density and hence the number of electrons that can be trapped at the surface [23].

Surface passivation also increases the gate leakage current. The increased leakage is likely due to the edge effect on the Schottky barrier that lowers the barrier on the edges

of the contact at the passivation surface. This effect has been noted by [93] in experiments on HFETs with growth and metallization similar to those used in this study.

Surface passivation has been shown to increase the 2DEG electron concentration, drain-to-source current, and transconductance in HFETs similar to those used in this research. Kordos, *et al.* [24] found that SiN passivation on various samples deposited at 150-300 °C and in layers 30-160 nm thick resulted in increases in carrier concentration of 24-27%, increases in drain-to-source current of 22-37%, and increases in transconductance of 11-17%.

Some of the HFETs irradiated in this study were passivated with a SiN layer using Plasma Enhanced Chemical Vapor Deposition (PECVD) after metallization. Chapters 5 and 6 present and compare the results from irradiating both passivated and unpassivated HFETs.

### **III. Model for Radiation Effects**

When electrons or neutrons enter semiconductor material there are three possible outcomes: the energetic particles pass through the material with no energy loss, the particles (if charged) lose their energy through ionization, and the particles lose energy through non-ionizing interactions. The ionization energy loss is dose rate dependent and transitory while the non-ionizing loss is total dose dependent and persistent. This research is concerned with non-ionizing energy loss (NIEL) of the energetic particles in the semiconductor. The primary NIEL effect is displacement of constituent atoms leading to vacancies, interstitials, and the formation of defect complexes.

NIEL is a measure of the energy transferred to the atoms of the semiconductor lattice during irradiation. The effect of the energetic particles on the constituent atoms of the material differs depending on the atomic species, binding energy, and energy of the particles. The potential effects of the type and energy of the incident radiation can be determined by analyzing the possible energy transfer to the lattice atoms. Additionally, in order to determine the NIEL in a particular material, a calculation of the radiation dose for the energy level of the impinging particles is necessary.

#### ***3.1 Electron Non-ionizing Energy Loss***

The rates of displacement damage formation for the Ga, N, and Al sublattices depend on both the displacement energy and the maximum transferable energy via collisions. The displacement energy depends on the energy binding the atom to the lattice and the angle of the interaction. However, the fraction of energy transferred depends on

the mass of the nucleus. In order to determine the threshold energy for damage to each sublattice, both factors must be taken into account.

The maximum energy imparted to an atom in the lattice by an electron of energy  $E_{e^-}$  is given by [25]

$$E_{trans}^{max} = 2 \frac{(E_{e^-} + 2m_e c^2)}{m_{atom} c^2} E_{e^-} \quad (11)$$

where the  $E_{trans}^{max}$  value for each component of GaN and  $Al_xGa_{1-x}N$  is shown in Table 2. The displacement energy of the lattice constituents in GaN have been calculated by Nord [26]. The minimum displacement energies are  $22 \pm 1$  eV for Ga and  $25 \pm 1$  eV for N, where the minimum is an average over all angles. In an experimental study, Ionascut-Nedelcescu [2] found a minimum displacement energy of  $19 \pm 2$  eV for gallium. For an average over all possible angles (from Nord [26]), the displacement energies are  $45 \pm 1$  eV for Ga and  $109 \pm 2$  eV for N. The maximum energy transfer values in Table 2 are calculated using equation (11).

Table 2. Maximum Energy Transferred to AlGa<sub>x</sub>N Atomic Constituents for Given Electron Energies

Incident Energy (MeV)	Max Energy Transferred to Ga Atom (eV)	Max Energy Transferred to Al Atom (eV)	Max Energy Transferred to N Atom (eV)
0.42	18.7	48.2	92.9
0.62	31.4	81.0	156
1.0	62.3	161	310
1.2	82.1	212	409

The minimum electron energy necessary to create displacement of nitrogen atoms is approximately 0.15 MeV and for gallium atoms 0.50 MeV (Ionascut-Nedelcescu found

0.44 MeV for gallium [2]). Assuming that Al has a displacement energy comparable to that of the Ga atom, approximately 24 eV based on the mass difference between Al and Ga, then 0.27 MeV electrons are required for Al displacement. The ability to trigger different displacement types with different energy electrons permits the concentration on the effects of the displacement of different sublattice atoms. Figure 4 is a plot of the maximum energy transfer as a function of incident electron energy for gallium and nitrogen.

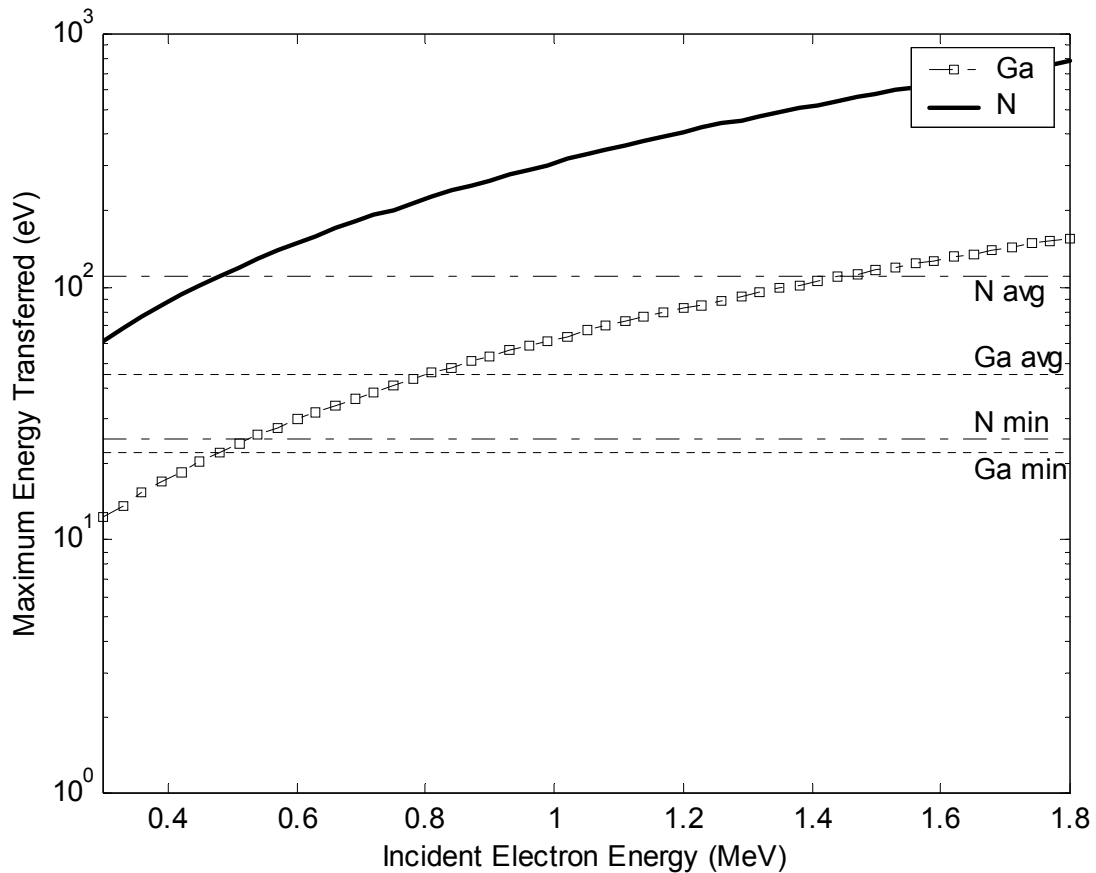


Figure 4. Maximum energy transfer for Ga and N as a function of the incident electron energy. The average and minimum displacement energies for both Ga and N are shown as horizontal lines. Values are calculated with equation (11) [27].

Look, *et al.* [29] took into consideration an average acceptance angle of 15° to account for thermal motions and possible beam misalignment in order to calculate N and Ga displacement energies of 66 and 38 eV, respectively. From these calculations and factoring in the higher mass of the Ga, they conclude that the minimum electron energy required for N displacement is 0.32 MeV and for Ga displacement is 0.53 MeV [29] These energies are comparable to the energies of terrestrially trapped electrons in near earth orbits.

The flux of electrons reaching the sample from the Van de Graaff (VDG) accelerator is determined by current integration. The electrons that reach the target sample mount are measured allowing for the determination of the charge deposition in the sample. Dose is determined by translating the charge deposition from the current integration into a dose received in the material of interest. The tool used to perform these calculations is the TIGER Monte Carlo electron transport code [30]. The electron stopping powers for the materials in the heterostructure is determined using the XGEN routine of the TIGER code using the parameters shown in Table 3, with silicon added as a reference material.

Table 3. Material Parameters Used for Dose Calculations [8]

<i>Material</i>	<i>Weight Fractions</i>			<i>Density (g/cm<sup>3</sup>)</i>
Si	Si – 1.0	N/A		2.33
GaN	Ga – 0.8327	N – 0.1673		6.15
Al <sub>0.3</sub> Ga <sub>0.7</sub> N	Al -0.114	Ga -0.689	N -0.197	~5.0
Al <sub>2</sub> O <sub>3</sub>	Al – 0.5293	O – 0.4707		3.98

The electrons are assumed to be monoenergetic and incident normally to the sample face for determining the stopping power and dose deposition profile using XGEN. The stopping power in Si, GaN, and Al<sub>2</sub>O<sub>3</sub> as calculated is shown in Figure 5.



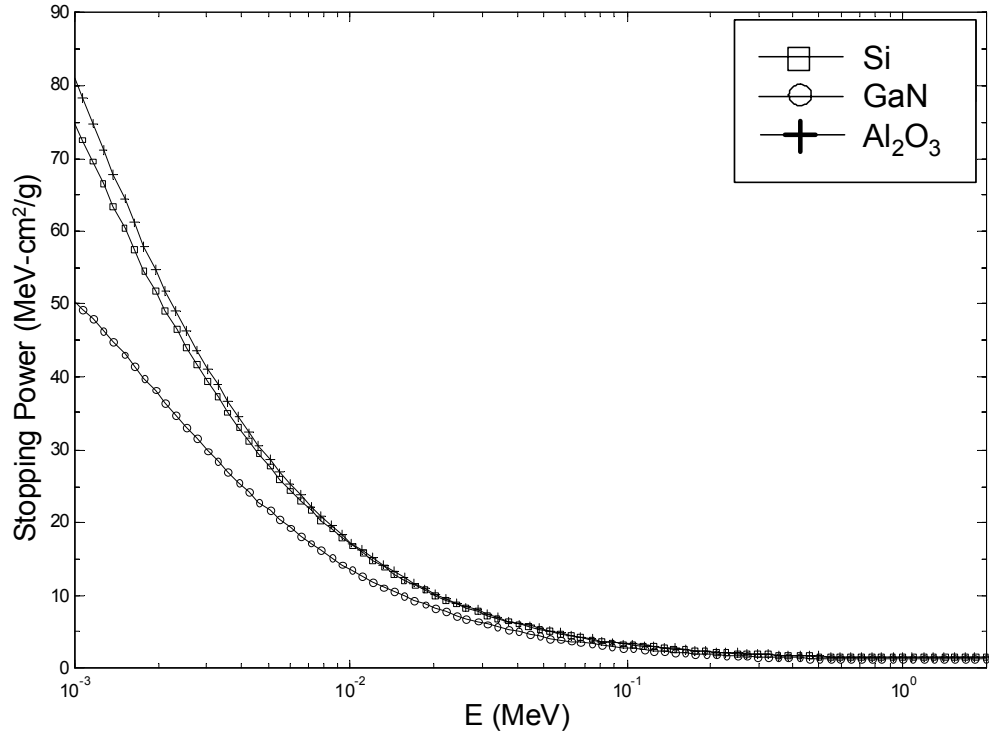


Figure 5. Electron stopping powers as calculated by XGEN for materials of interest [31].

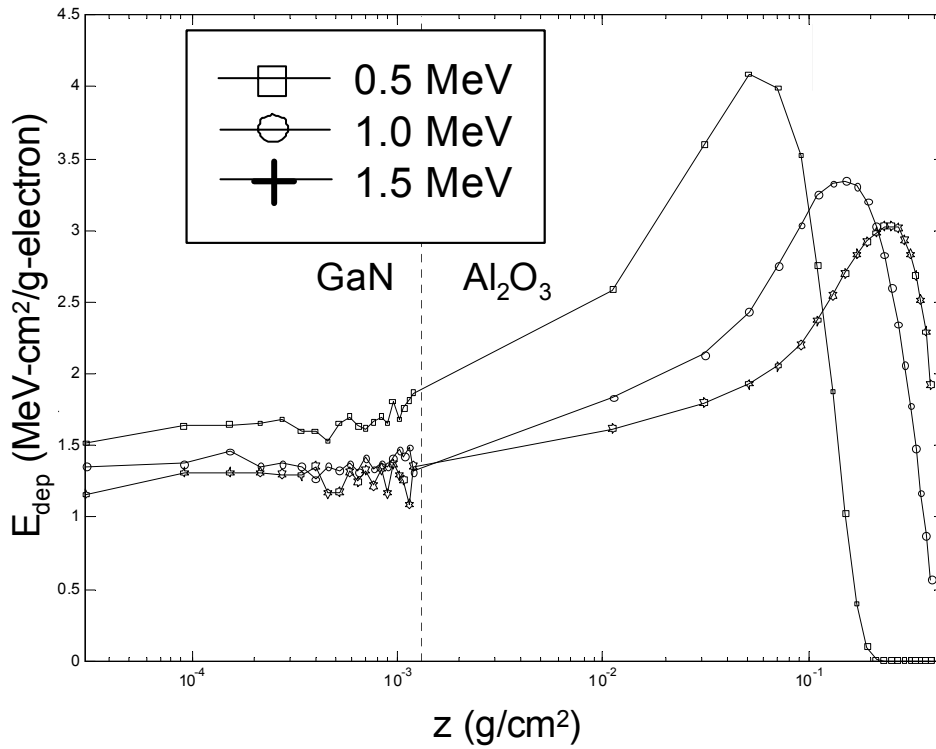


Figure 6. Dose deposition profiles for GaN (2 μm) on Al<sub>2</sub>O<sub>3</sub> (1 mm) for particle energies of 0.5, 1.0, and 1.5 MeV. Calculation was performed using 200,000 histories in 20 batches in TIGER [31].

The dose deposition profile in a 2.0  $\mu\text{m}$  GaN epilayer grown on an  $\text{Al}_2\text{O}_3$  substrate is shown in Figure 6. The majority of the absorbed dose is in the substrate. Likewise a thin AlGaIn layer on top of the GaN would absorb even less of the total dose.

### 3.2 Neutron Non-Ionizing Energy Loss

To determine the displacement damage effectiveness of a neutron source the neutron energy spectrum is reduced to a monoenergetic source with a damage effectiveness equivalent to the entire spectrum. For purposes of radiation testing of electronics, the 1 MeV equivalent neutron fluence for silicon (1 MeV Eq (material)) or simply 1 MeV (eq) is reported. The 1 MeV (eq) is determined by using MIL-STD-750D METHOD 1017.1. The DoD approved method is outlined in the ASTM E722(1994) standard [32]. The 1 MeV (eq) is the fluence required of 1 MeV monoenergetic neutrons to cause the same amount of damage as the entire neutron spectrum for a given material. ASTM E722(1994) provides the damage functions of both Si and GaAs. Using equation (12) below, 1 MeV equivalent electron dose can be determined.

$$\phi_{EQ,1MeV,MAT} = \frac{\int_0^{20MeV} \phi(E)F_{D,MAT}(E)dE}{F_{D,1MeV,MAT}} \quad (12)$$

where  $\phi(E)$  is the energy-dependent incident neutron energy-fluence spectral distribution,  $F_{D,MAT}(E)$  is the energy-dependent neutron displacement damage function for the material of interest, and  $F_{D,1MeV,MAT}$  is the displacement damage reference value at 1 MeV.  $F_{D,1MeV,Si}$  and  $F_{D,1MeV,GaAs}$  are 95 and 70 MeV-mb respectively.

### ***3.3 Defects in GaN and AlGaN***

In order to determine the effects of radiation on the properties of the 2DEG we need an understanding of the current state of knowledge regarding the defects caused by radiation on the constituent materials. Defects in AlGaN, GaN, SiC, and SiN have been studied due to their potentially negative effect on the operation of devices based on these materials. Defects caused by the interaction of radiation with the constituent materials are particularly worrisome for devices operated in radiation environments. The defects in GaN have been investigated extensively but those in AlGaN to a lesser degree. Radiation induced defects in SiC and SiN that may have a detrimental effect on the HFETs have also been studied. The defects in SiC are unlikely to have a great effect on the gate and drain current because of their distance from the gate and the channel but they will still be present in the device. SiN defects may affect the properties of the passivated HFETs. This section reviews the current state of knowledge on the defect types and formation mechanisms in all these materials with an emphasis on those defects caused by the interaction of electron and neutron radiation.

There are a number of different types of point defects that can occur in both as-grown and irradiated GaN and AlGaN. These defects include vacancies, interstitials, and anti-sites as well as complexes between defects or with impurities. The concentration and energy level of point defects in as-grown material depends upon the formation energy. This concentration as well as the rate of introduction is dependent on the growth and processing techniques employed by the manufacturer. These defects may also exist in more than one charge state. In addition, in alloys such as AlGaN additional defect states are possible depending on the nearest neighbor configuration in the vicinity of the defect.

Defects in GaN have been investigated by numerous spectroscopic techniques [33]. The defects can be separated into two groups: as-grown defects and radiation-induced defects.

As-grown defects in GaN include a number of species that have been investigated in detail in recent years. The primary as-grown donor is thought to be a Si or O impurity as opposed to a donor-like defect such as  $V_N$  or  $Ga_I$  [34].  $V_{Ga}$  has been established as the primary acceptor in as-grown GaN [35]. Self-compensation can also be a strong force in wide-bandgap materials since the lattice can lower its energy by creating these defect donors and acceptors to compensate p-type and n-type material [36].

The primary electron irradiation produced shallow donor in GaN is the  $V_N$  with an experimentally determined energy 0.06 eV below the conduction band [34]. The  $Ga_I$  is a deep paramagnetic center as detected by Optically Detected Magnetic Resonance (ODMR) [37] as well as Electron Paramagnetic Resonance (EPR) [27]. The  $N_I$ , a potential acceptor, is likely mobile and recombines with a vacancy or recombines with existing impurities or defects [29]. There have also been recent reports of Positron Annihilation Spectroscopy (PAS) detection of  $V_{Ga}$  in deep acceptor states after 2.0 MeV electron irradiation [38]. There are additionally numerous electron traps that have been discovered primarily by DLTS. Table 4 from Hogsed [39] shows the location of various electron generated shallow and deep traps in GaN.

Radiation induced defects that are 0.4 to 1.0 eV below the conduction band edge that act as electron trapping sites are most important in considering changes to the gate leakage current. As shown in Table 4, the nitrogen vacancy at 0.85 below the conduction band that is introduced during electron irradiation [41] is a likely trapping site in the

AlGaN layer that leads to increased trap-assisted tunneling through the Schottky barrier and into the channel.

Table 4. Defects in Gallium Nitride.

GaN								
Category	Energy as-grown (eV)	Introduced/ Increased by Radiation (eV)	Thermal Energy (eV)	Type of Radiation	Method	Material	I.D.	Ref.
Donors	0.06 0.018	0.06	0.06	e <sup>-</sup> (1 MeV)	TDH	undoped HVPE n $\approx$ 10 <sup>17</sup>	V <sub>N</sub> Si <sub>Ga</sub>	[34]
Acceptors			deep	e <sup>-</sup> (1 MeV)	TDH	"	N <sub>I</sub>	[34]
			deep	e <sup>-</sup> (2 MeV)	Positron Annihil.	Semi-insulating bulk [Mg] $\approx$ [O] $\approx$ 10 <sup>20</sup>	V <sub>Ga</sub>	[38]
Electron Traps	0.21, 0.27, 0.45, 0.61	0.22	<u>0.22 peak fit:</u> 0.06, 0.10, 0.20	e <sup>-</sup> ( <sup>90</sup> Sr)	DLTS	Undoped MOVPE ELO n $\approx$ 10 <sup>16</sup>	V <sub>N</sub>	[40]
	0.24, 0.45, 0.62	0.18, 0.85	0.06	e <sup>-</sup> (1 MeV)	DLTS	Undoped MOCVD n $\approx$ 10 <sup>16</sup>	V <sub>N</sub>	[41]

AlGaN has many of the same defects as GaN, but the energy levels differ owing to molecular bonding arrangements that depend on the Aluminum mole fraction. In recent work by Hogsed [42] a radiation induced defect level in AlGaN not found in GaN was investigated using DLTS. It was found to be at 0.33 eV below the conduction band edge in AlGaN with a mole fraction of  $x = 0.14$  and 0.38 eV for  $x = 0.20$ . This defect's origins have not yet been determined.

Defects induced in SiC by irradiation are mostly of concern in this work if they are charged. Charges in the SiC substrate can have an effect on the electrons in the 2DEG. Because of the minimum 2  $\mu$ m distance from the substrate to the 2DEG this effect is greatly diminished with respect to AlGaN defects that are within 25 nm of the 2DEG and GaN defects that are within 2  $\mu$ m. However they cannot be completely discounted. The carbon in a silicon position (C<sub>Si</sub>) antisite is potentially most significant because of its

+2 charge [43] that could decrease the 2DEG concentration by the resulting field. Figure 7 shows the X-Band Electron Paramagnetic Resonance (EPR) spectrum of an HFET recorded in this research. The post-irradiation spectrum shows the appearance of the  $C_{Si}$  after 1 MeV electron irradiation.

Defects in the SiN passivation can also have a detrimental effect on the gate leakage and drain currents. Any charges trapped in the SiN will particularly affect the drain current. Unlike the SiC, the edge of the SiN is only 25 nm from the AlGaIn-GaN interface. Trapped holes from electron-hole pair production are likely to have the greatest effect on the drain current. The additional positive charge in the SiN is above the channel next to the gate and will enhance the drain current at the same applied gate voltage, i.e. cause a threshold voltage shift. The determination of the dose to charging effect in SiN is described in Appendix A of Kucko [44].

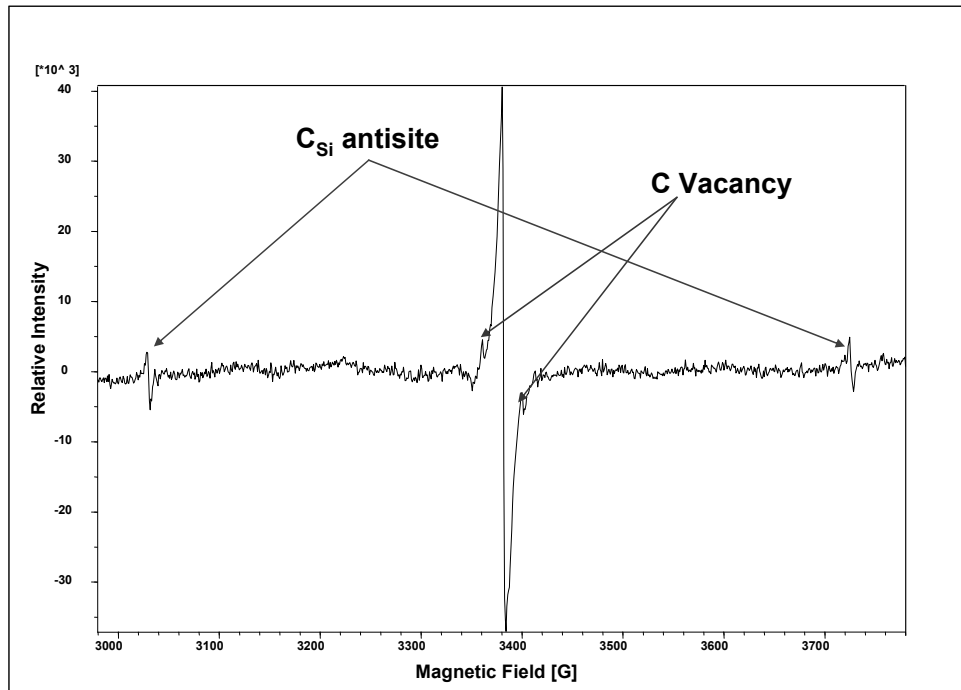


Figure 7. EPR spectrum of an HFET after 1.0 MeV electron irradiation with a fluence of  $1 \times 10^{16} \text{ cm}^{-2}$ . The carbon vacancy and the carbon in a silicon position antisite defects are clearly visible.

### **3.4 Radiation Effects on AlGaN/GaN Devices**

The Non-Ionizing Energy Loss (NIEL) of radiation in the heterostructure potentially causes the formation of nitrogen, gallium, and aluminum vacancies and interstitials. The goal of this research is to link defects to changes in the properties of the 2DEG and in the gate leakage current and hence the effect of these radiation-induced defects on device operation and reliability. This section reviews previous radiation effects studies on the 2DEG properties and gate leakage current. Proton irradiation studies dominate the literature with a few electron studies available, generally conducted with electron energies at or above 1 MeV. In contrast this study has obtained interesting results using lower energy electron and neutron radiation and by including temperature dependent effects.

The two primary ways radiation defects affect the 2DEG are by changing the electron density and/or changing the electron mobility. The 2DEG carrier concentration is changed by charged defects causing changes to the field at the interface. Positively charged defects in the AlGaN layer will increase the field at the interface allowing a greater density of electrons to accumulate. Conversely, negative defects in the AlGaN will decrease the field and the resulting carrier density. Positive and negative defects in the GaN layer have the opposite effect. This effect is manifested as a change to the threshold voltage. Additionally, ionized donor-type traps produced in both the AlGaN and GaN layers which contribute electrons to the conduction band can add to the carrier concentration in the 2DEG.

Post-irradiation changes to the electron mobility are primarily due to scattering from charged defect centers resulting from atomic displacements. Charged defects

outside and inside the 2DEG channel interact with the carriers through the Coulomb interaction. The mobility can also be degraded by increases to surface roughness at the AlGa<sub>N</sub>/Ga<sub>N</sub> interface. Surface roughness is the result of alloy disorder from atomic displacements near the interface. The alloy disorder is due to the radiation induced displacement of aluminum from the AlGa<sub>N</sub> side of the interface that to the Ga<sub>N</sub> side. This will degrade the mobility in the channel and at a high radiation level can lead to a breakdown in the piezoelectric field that maintains the 2DEG since an abrupt interface is necessary for maintenance of the quantum well.

### **Experimental Studies (Protons)**

In 2002, White, *et al.* [45] examined the effect of 1.8 MeV proton irradiation on AlGa<sub>N</sub>/Ga<sub>N</sub> MODFETs (Modulation Doped Field Effect Transistors which in this context is synonymous with HFET). The observed effects of proton irradiation on the electrical transfer characteristics of the device include a decrease in the saturation current, drain current, and transconductance as shown in Figure 8. White, *et al.* used low-energy electron-excited nanoscale-luminescence spectroscopy (LEEN), a low energy analog to cathodoluminescence, to probe the defects created by irradiation. They concluded that the changes in the electronic properties of the AlGa<sub>N</sub>/Ga<sub>N</sub> MODFET are due to a reduction of the internal electric field due to screening caused by charged complexes created in the AlGa<sub>N</sub> layer. The decreased field strength results in a reduction in the carrier density in the 2DEG well. While they concede that new defect complexes can also remove existing donors [46] and can lead to a reduction in channel mobility, these cannot account for the spectral differences found using LEEN [45].



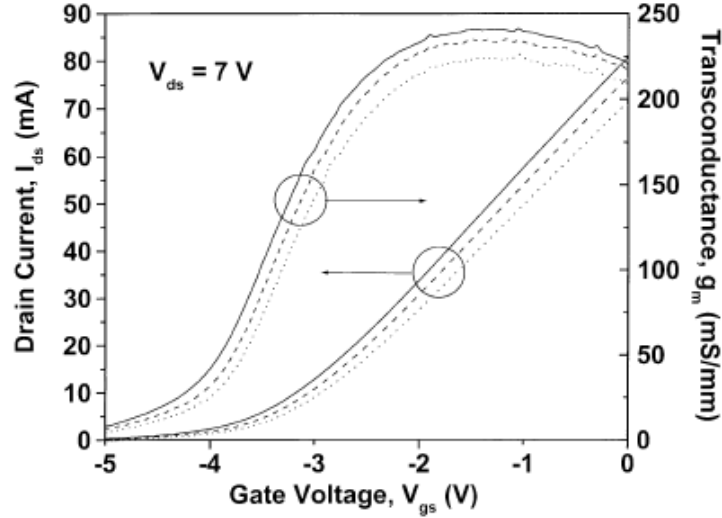


Figure 8. Common-source drain current as a function of gate voltage and transconductance of the same transistor pre-irradiation (solid line), post- $10^{12} \text{ cm}^{-2}$  fluence (dashed line), and post- $5 \times 10^{13} \text{ cm}^{-2}$  fluence (dotted line) [45].

Also in 2002, Luo, *et al.* [47], investigated the effect of high-energy proton irradiation on AlGaIn/GaN high-electron mobility transistors (HEMTs). The study used 40 MeV protons at doses that replicated over 100 years of exposure in low-earth orbit. The results showed a decrease in transconductance, drain-source current, forward gate current, and reverse breakdown voltage that they credited to a decrease in electron concentration in the HEMT channel. The decrease in breakdown voltage in particular indicates that protons created deep trap states that remove electrons. The possible nature of these traps is not discussed. Post-irradiation annealing restored approximately 70% of the initial decrease in transconductance and drain-source current.

Gaudreau, *et al.* (2002) [48], investigated the effects of 2-MeV protons on the transport properties of the two-dimensional electron gas at the AlGaIn/GaN interface using resistivity and Hall effect measurements. A fluence of  $10^{13} \text{ cm}^{-2}$  to  $7 \times 10^{15} \text{ cm}^{-2}$  of proton irradiation produced a carrier density decrease of a factor of two while the

mobility degraded by a factor of a thousand. A fluence of  $3 \times 10^{14} \text{ cm}^{-2}$  to  $3 \times 10^{15} \text{ cm}^{-2}$  caused the channel to change from a conductor to an insulator. This was attributed primarily to changes in the electron mobility. At fluences  $> 3 \times 10^{14} \text{ cm}^{-2}$ , the defects outside the region of the 2DEG gain importance in their effect on the electrical properties of the device. This is because changes in the mobility dominate over changes in the carrier density. Additionally, the authors reconfirm other research that indicated that AlGaIn/GaN is at least two orders of magnitude more radiation-resistant than AlGaAs/GaAs.

In 2003, Hu, *et al.* [49], studied the degradation of AlGaIn/AlN/GaN HFETs due to 1.8 MeV proton irradiation at fluences up to  $3 \times 10^{15} \text{ cm}^{-2}$ . These devices are similar to AlGaIn/GaN HFETs used in the current research but with a higher intrinsic mobility due to the reduction in alloy disorder scattering at the interface of the GaN and AlN. The larger bandgap difference at the heterojunction leads to a lesser penetration of the 2DEG electrons into the AlGaIn, also increasing mobility. The devices studied possessed high radiation tolerance up to  $10^{14} \text{ cm}^{-2}$  similar to AlGaIn/GaN devices, although they demonstrated decreased sheet carrier mobility and decreased sheet carrier density at higher fluences. Overall device performance degradation was a result of decreased maximum transconductance, increased threshold voltage, and decreased drain saturation current as shown in Figure 9.

AlGaIn/GaN device degradation is postulated to be caused by two mechanisms: defect centers outside the 2DEG well which decreases mobility due to Coulomb scattering and defect centers inside the 2DEG that leads to a decrease in 2DEG density.

Hu, *et al.* follow the arguments of Gaudreau, *et al.* [48], and Jun and Subramanian [50], in making this identification.

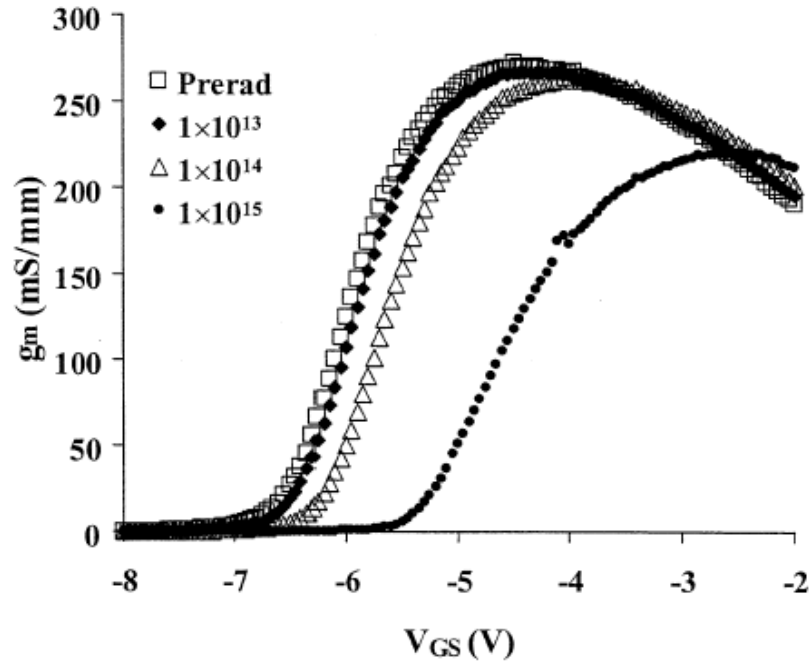


Figure 9. Transconductance versus gate-source voltage for AlGaIn/GaN HEMTs before and after 1.8 MeV proton irradiation with fluences from  $10^{13}$  to  $10^{15}$   $\text{cm}^{-2}$  [49].

Also in 2003, White, *et al.* [51], reported degradation of the channel properties of an AlGaIn/GaN HEMT grown on sapphire for 1.8 MeV protons at fluences above  $10^{14}$   $\text{p}^+/\text{cm}^2$ . For fluences through  $2 \times 10^{15}$   $\text{cm}^{-2}$ , they observed sheet resistance change primarily through degradation of the mobility. Above a fluence of  $5 \times 10^{15}$   $\text{cm}^{-2}$  both the mobility and sheet density decreased significantly as shown in Figure 10. The authors cite scattering and interface roughness as the cause of the mobility degradation at lower fluence levels. The partial relaxation of strain and dopant compensation in both the AlGaIn and GaN are the primary factors in the depopulation of the 2DEG.

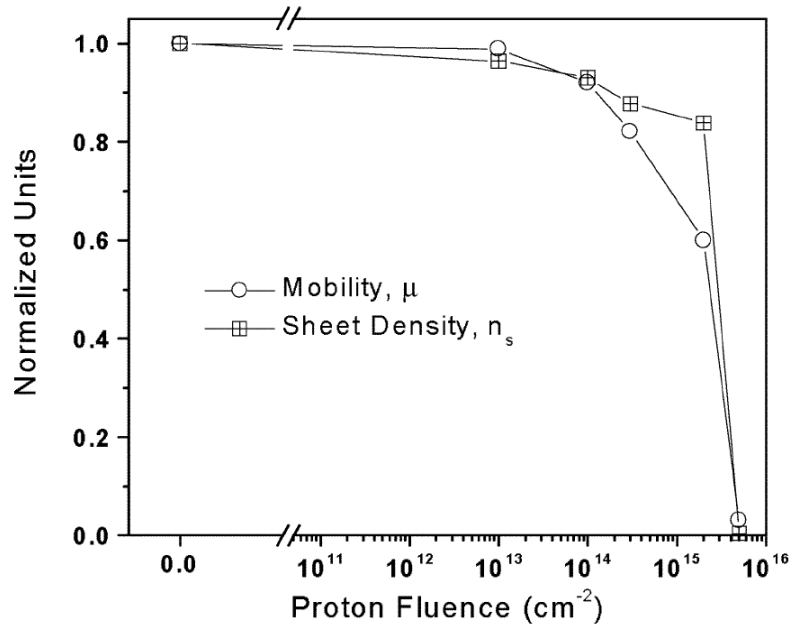


Figure 10. Normalized mobility and 2DEG sheet density from room temperature Hall Effect measurements [51].

In 2004, Hu, *et al.* [52], studied the energy dependent proton-induced degradation in AlGaIn/GaN HEMTs. They irradiated HEMTs with 1.8 MeV, 15 MeV, 40 MeV, and 105 MeV protons at fluences up to  $10^{13}$  cm<sup>-2</sup>. The greatest degradation was found for the lowest energy protons because of the much larger non-ionizing energy loss. Very little degradation was found for protons with energy greater than 15 MeV. The results for 40 MeV protons are contradictory with those of Luo, *et al.* [47] who found much higher degradation at lower fluence levels. They also found that the damage recovered after room temperature annealing. For a fluence of 1.8 MeV protons at  $10^{13}$  cm<sup>-2</sup>, the drain current decreased by approximately 10% and the maximum transconductance decreased by 6.1% as shown in Figure 11.

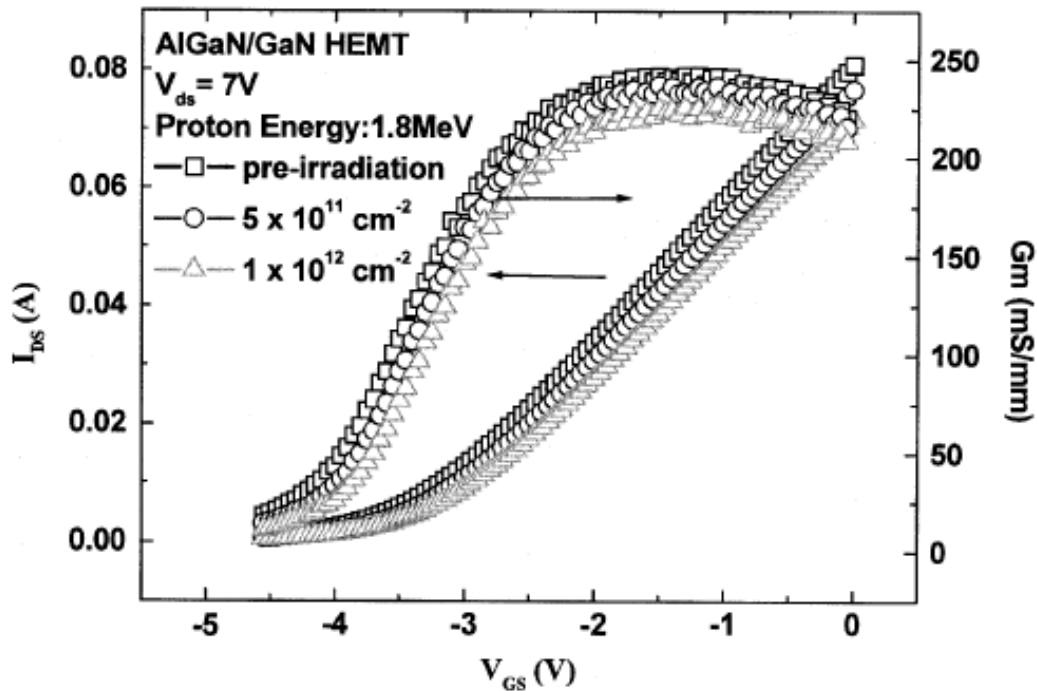


Figure 11. Transfer characteristics for AlGaIn/GaN HEMTs before and after 1.8-MeV proton irradiation at different fluences [52].

### Experimental Studies (Gammas)

Also in 2004, Aktas, *et al.* [53] investigated the effect of 600 MeV  $^{60}\text{Co}$  gamma radiation on AlGaIn/GaN HEMTs. The contact resistance, sheet resistivity, Hall mobility, and sheet carrier density did not exhibit significant changes up to the maximum dose used of 600 Mrad. The most significant results was a -0.1 V threshold voltage shift at a 600 Mrad total dose. These results were determined to be the result of the production of ionized donor sites close to the conduction band and acceptor sites at mid-gap in the AlGaIn under the gate. Some of the donors generated by the irradiation were found to contribute electrons to the channel resulting in a negative threshold voltage shift.

## Experimental Studies (Neutrons)

In 2005, Polyakov, [54] irradiated AlGaN/GaN heterostructures and Schottky diodes with 1 MeV neutrons and measured the post-irradiation mobility, capacitance, and transconductance. They found a measurable decrease in the 2DEG mobility at both 77 K and 300 K at doses above  $10^{14} \text{ cm}^{-2}$  and a decrease in 2DEG carrier concentration at fluences of above  $1.7 \times 10^{17} \text{ cm}^{-2}$ . The authors attribute the observed decrease in mobility to the introduction of additional scattering centers in the GaN channel. The 2DEG concentration decrease is related to the introduction of shallow centers in the AlGaN gate.

Table 5 presents a recapitulation of experimental results reported since 2002 that are relevant to the current study. The table presents the radiation type, temperature during irradiation, parameter measured, temperature during measurement, general change in the parameter recorded after irradiation, and the fluence at which the change occurred. Most notably, all of the irradiations and electrical measurements in those studies were conducted at room temperature.

Table 5. Relevant Results in Radiation Effects on AlGaN/GaN HFETs

Reference	Radiation Type/ Temperature	Measurement/ Temperature	Observed Change After Irradiation	Fluence Level at Onset of Change
White, <i>et al.</i> , 2002 [43]	1.8 MeV protons @ RT	$I_{ds}$ @ RT	Decrease	$1 \times 10^{11} \text{ p}^+/\text{cm}^{-2}$
Luo, <i>et al.</i> , 2002 [45]	40 MeV protons @ RT	$I_{ds}$ @ RT	Decrease	$5 \times 10^9 \text{ p}^+/\text{cm}^{-2}$
Hu, <i>et al.</i> , 2003 [47]	1.8 MeV protons @ RT	$I_{ds}$ @ RT	Decrease	$1 \times 10^{14} \text{ p}^+/\text{cm}^{-2}$
White, <i>et al.</i> , 2003 [49]	1.8 MeV protons @ RT	$I_{ds}$ @ RT Rev. and Fwd. $I_{gs}$ @ RT	Decrease Decrease then increase	$1 \times 10^{13} \text{ p}^+/\text{cm}^{-2}$ $1 \times 10^{12} \text{ p}^+/\text{cm}^{-2}$
Karmarkar, <i>et al.</i> , 2004 [53]	1.8 MeV protons @ RT	$I_{ds}$ @ RT Forward $I_{gs}$ @ RT	Decrease Decrease	$1 \times 10^{13} \text{ p}^+/\text{cm}^{-2}$ $1 \times 10^{12} \text{ p}^+/\text{cm}^{-2}$
Hu, <i>et al.</i> , 2004 [50]	105 MeV protons @ RT  40-, 15-MeV protons @ RT 1.8 MeV protons @ RT	$I_{ds}$ @ RT Forward $I_{gs}$ @ RT Reverse $I_{gs}$ @ RT $I_{ds}$ @ RT $I_{ds}$ @ RT	Decrease No Change Decrease No Change Decrease	$1 \times 10^{13} \text{ p}^+/\text{cm}^{-2}$ Up to $1 \times 10^{13} \text{ p}^+/\text{cm}^{-2}$ $3 \times 10^{11} \text{ p}^+/\text{cm}^{-2}$ Up to $1 \times 10^{11} \text{ p}^+/\text{cm}^{-2}$ $5 \times 10^{11} \text{ p}^+/\text{cm}^{-2}$
Atkas, <i>et al.</i> , 2004 [51]	$^{60}\text{Co}$ gamma @ 343 K	$I_{ds}$ @ RT	Increase	300 MRad
Sonia, <i>et al.</i> , 2006 [54]	68 MeV $\text{p}^+$ and ions @ RT  2 MeV protons @ RT 2 MeV ions @ RT	$I_{ds}$ @ RT  $I_{ds}$ @ RT $I_{ds}$ @ RT	No Change  No Change Decrease	Up to $1 \times 10^{13} \text{ p}^+/\text{cm}^{-2}$ Up to $1 \times 10^{11} \text{ ions}/\text{cm}^{-2}$ Up to $1 \times 10^{13} \text{ p}^+/\text{cm}^{-2}$ $5 \times 10^{10} \text{ p}^+/\text{cm}^{-2}$
This Study	1.0 MeV neutrons @ 84 K	$I_{ds}$ @ 80 K Rev. $I_{gs}$ vs. T @ 82-294 K $I_{ds}$ @ RT $I_{ds}$ @ 80 K after Anneal $I_{ds}$ @ 294 K after Anneal Rev. $I_{gs}$ vs. T @ 82-294 K after Anneal	Increase Increase Decrease Recovery No Recovery No Recovery	$3 \times 10^{10} \text{ n}/\text{cm}^{-2}$ $3 \times 10^{10} \text{ n}/\text{cm}^{-2}$ $6 \times 10^{12} \text{ n}/\text{cm}^{-2}$ $6 \times 10^{12} \text{ n}/\text{cm}^{-2}$ $6 \times 10^{12} \text{ n}/\text{cm}^{-2}$ $6 \times 10^{12} \text{ n}/\text{cm}^{-2}$

The current research extends these results using similar heterostructures configured as HFETs and applying 0.45 MeV electrons and 1 MeV neutrons as the irradiation source. The goal of the work is to use low temperature irradiation and temperature-dependent measurements to determine the mechanisms responsible for post-irradiation changes to drain-to-source and gate leakage currents.

### 3.5 The Trap-Assisted Tunneling Model

Trap-Assisted Tunneling (TAT) consists of tunneling by electrons in the gate metal into the Schottky barrier via traps in the AlGa<sub>N</sub> layer and tunneling from the traps into the conduction band of the AlGa<sub>N</sub> layer. The electrons then pass through the low barrier at the AlGa<sub>N</sub>/Ga<sub>N</sub> interface and continue into the channel and out through the source and drain. The band diagram of the heterostructure is depicted in Figure 12.

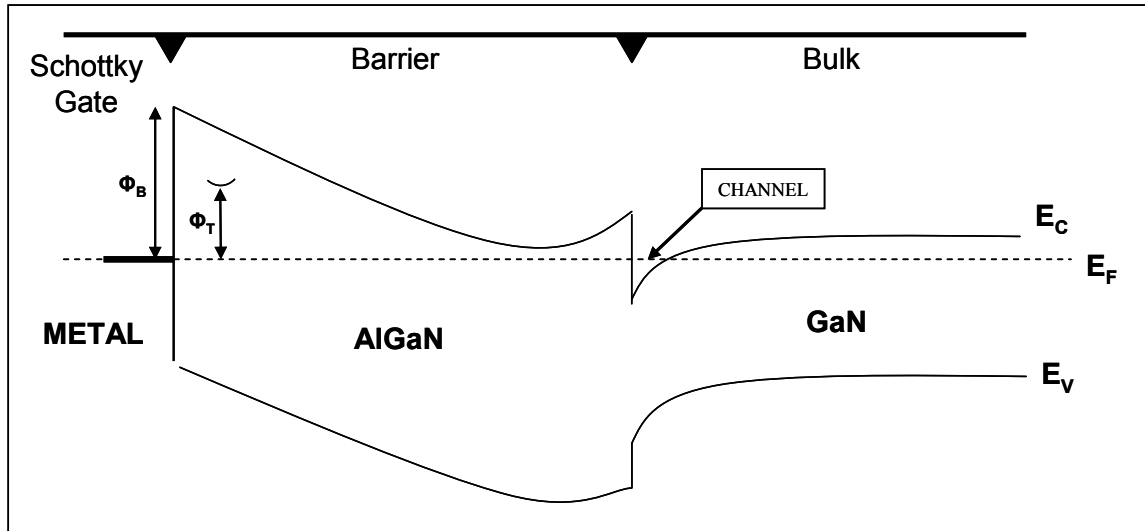


Figure 12. Band diagram of the AlGa<sub>N</sub>/Ga<sub>N</sub> heterostructure.

The tunneling current is an integration of the tunneling rate (R) over energy [57]:

$$I_{TAT} = \frac{qA}{\epsilon} \int_{\phi_i}^{\phi_b + |V_g|} R d\phi, \quad (13)$$

where  $A$  is the area of the gate,  $\mathcal{E}$  is the electric field in the AlGaIn layer,  $\varphi_b$  is the Schottky Barrier height,  $\varphi_t$  is the trap height, and  $V_g$  is the applied gate voltage.

The total tunneling rate,  $R$ , is the rate limited sum of the two tunneling rates  $R_1$  and  $R_2$ :

$$\frac{1}{R} = \frac{1}{R_1} + \frac{1}{R_2} \quad (14)$$

where

$$R_1 = C_t f_{FD} N_t P_1 \quad (15)$$

and

$$R_2 = C_t N_t P_{2\_triangle}. \quad (16)$$

$R_1$  is the rate of tunneling through the Schottky barrier depending on the temperature-dependent Fermi-Dirac occupancy fraction,  $f_{FD}$  and the tunneling probability  $P_1$ .  $P_1$  is the probability that an electron above the metal Fermi level with energy  $\varphi$  will tunnel through the Schottky barrier to the trap energy level  $\varphi_t$ .  $R_2$  is rate of tunneling from the trap through the triangular barrier dependent on the tunneling probability  $P_{2\_triangle}$ . Both tunneling rates depend upon the trap density  $N_t$  and the trap energy dependent rate constant  $C_t$ . Figure 13 depicts the tunneling process.

The tunneling rates are based on the Wentzel-Kramers-Brillouin (WKB) approximation [60] for the probabilities and Fermi-Dirac statistics. The WKB approximation is valid for this model because of the linearity of the potentials. The Fermi-Dirac function for electrons in the gate metal is

$$f_{FD} = \frac{1}{1 + e^{\left(\frac{q(\varphi_b - \varphi)}{kT}\right)}}. \quad (17)$$



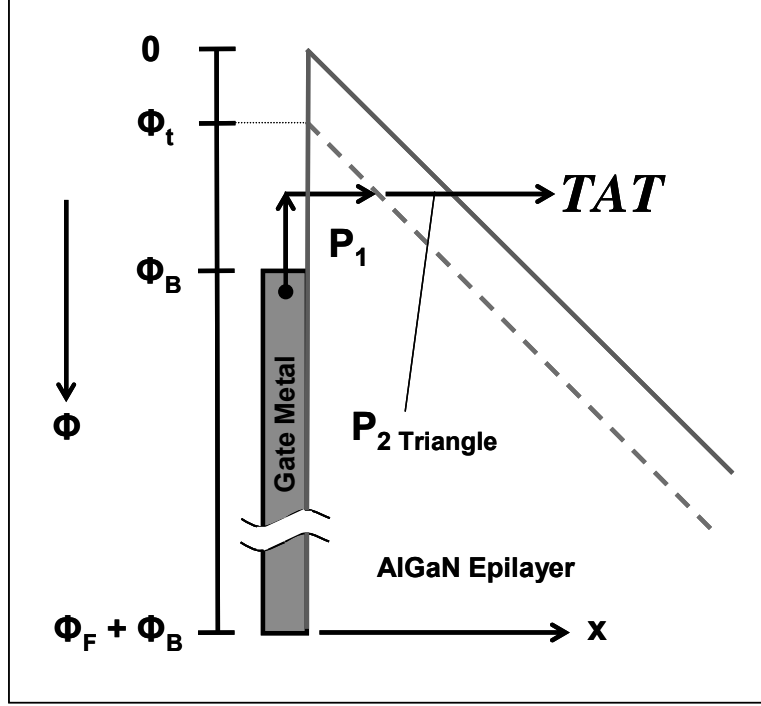


Figure 13. Trap-assisted tunneling through the Schottky barrier.

The probabilities of tunneling through the Schottky barrier to the trap level,  $P_1$ , and from the trap level through the triangular barrier into the conduction band of the AlGaN layer,  $P_2$ , are

$$P_1 = e^{-\frac{\alpha}{\epsilon} \left( \varphi^{\frac{3}{2}} - \varphi_t^{\frac{3}{2}} \right)} \quad (18)$$

and

$$P_{2\_triangle} = e^{-\frac{\alpha}{\epsilon} \varphi_t^{\frac{3}{2}}} \quad (19)$$

where

$$\alpha = \frac{8\pi\sqrt{2m_{AlGaN}q}}{3h}. \quad (20)$$

The trap energy dependent rate constant also comes from the WKB approximation [58]

and is given by

$$C_t = \left( \frac{m_M}{m_{AlGaN}} \right)^{5/2} \frac{16\pi q \varphi_1^{3/2}}{3h\sqrt{\varphi_t - \varphi_1}}, \quad (21)$$

where  $\varphi_1 = 0.2$  V is taken as the average total electron energy [59].

The total integral to be solved is then

$$I_{TAT} = \frac{qAC_t N_t}{\mathcal{E}} \int_{\varphi_1}^{\varphi_b + \varphi_F} \left( \frac{1}{f_{FD} P_1} + \frac{1}{P_{2\_triangle}} \right)^{-1} d\varphi \quad (22)$$

where  $\mathcal{E}$  is the field in the AlGaN layer, considered to be constant, and given by

$$\mathcal{E} = \frac{V_p + qN_d d^2 / 2\epsilon}{d} \quad (23)$$

where  $d$  is the AlGaN layer thickness,  $\epsilon$  is the dielectric constant of the AlGaN layer, and  $V_p$  is the voltage drop from the top of the Schottky barrier to the conduction band of the GaN bulk

$$V_p = V_g + \varphi_b - \Delta\varphi_C - \varphi_{fb} \quad (24)$$

where  $\Delta\varphi_C$  is the conduction band discontinuity at the AlGaN/GaN barrier and  $\varphi_{fb}$  is the flat band voltage as shown in Figure 14.

The Schottky barrier height incorporates image force barrier lowering and the bandgap reduction with temperature via [57]

$$\varphi_b = \varphi_{b0} - \gamma_1 \sqrt{\frac{q\mathcal{E}}{\pi\epsilon}} - \gamma_T T \quad (25)$$

where  $\gamma_1 = 0.4$  [57] and  $\gamma_T = 2.7 \times 10^{-4}$  V/K [8]. The integral is then a function of six variables  $T$ ,  $V_g$ ,  $N_d$ ,  $N_t$ ,  $\varphi_t$ , and  $\varphi_{b0}$  where  $N_d$  is the donor concentration,  $N_t$  is the trap concentration,  $\varphi_t$  is the trap energy level, and  $\varphi_{b0}$  is the Schottky barrier height.

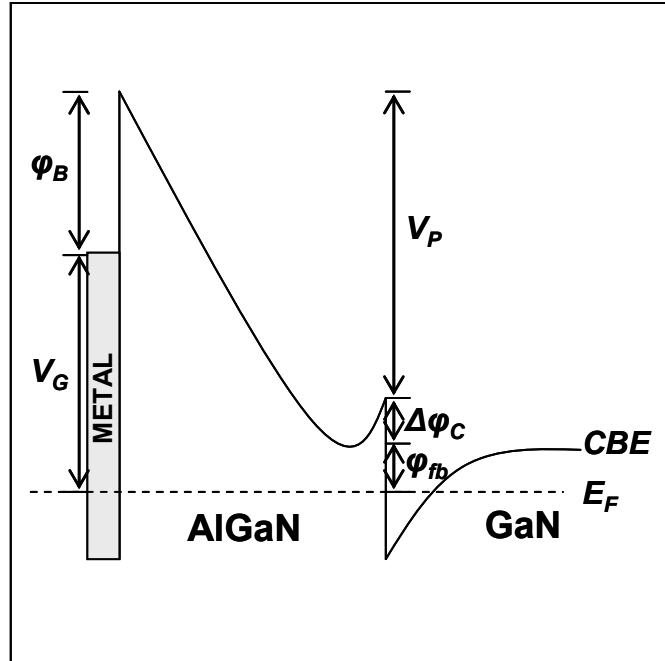


Figure 14. Band diagram of conduction band edge from the Schottky metal contact through the AlGaN layer to the GaN bulk showing the potentials used in the discussion.

The tunneling of electrons through the second barrier at the AlGaN-GaN interface is considered to be automatic in this model. Is this true? It depends on the height and width of the barrier and potentially the number of trap sites at the interface if trap-assisted tunneling is needed. In order to determine the height and width of the second barrier a model of the HFETs was built in the Davinci modeling program [61]. The resulting energy band diagram is shown in Figure 15. Electrons that have tunneled through the Schottky barrier into the conduction band of the AlGaN have sufficient energy to pass from the the AlGaN layer into the GaN layer by thermionic emission over the much lower barrier at the AlGaN-GaN interface.

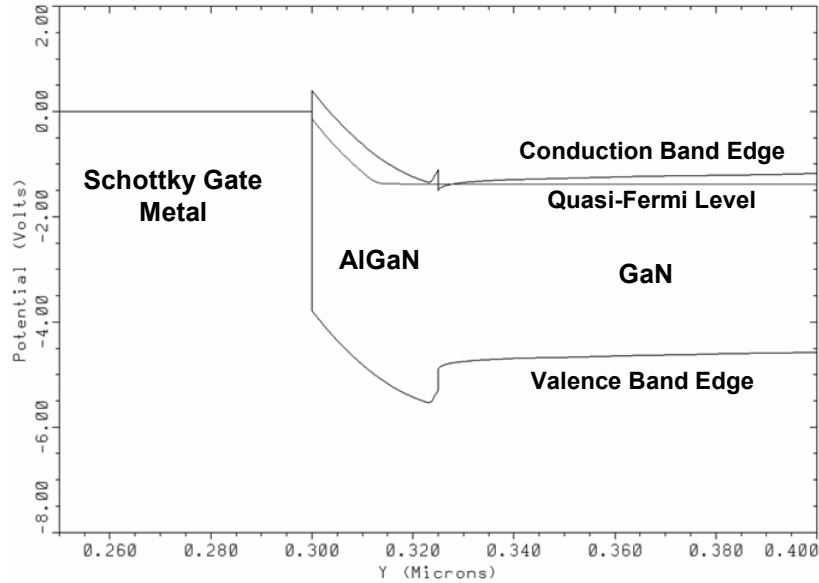


Figure 15. Energy band diagram of an unpassivated HFET using Davinci showing the relative heights and widths of the two barriers at the metal-AlGaN and AlGaN-GaN interfaces.

### 3.6 The Transistor Current Model

The second modeling effort ties the presence of irradiation induced defects to their influence on the electrical properties of the 2DEG. It uses the physics based charge control model developed by Rashmi, *et al.* [18], as introduced in Chapter 2, to a heterostructure with radiation induced defects in both the GaN and AlGaN layers.

The 2DEG formed at the AlGaN-GaN interface has an electron density that is polarization dependent, which is largely based upon the position of the Fermi level in the well. If one assumes that the total depletion region, i.e. the gate and junction depletion regions overlap, then equations (9) and (10) fully describe the effect of defects on the carrier concentration of the 2DEG. Combining equations (9) and (10) leads to

$$n_s = \frac{\varepsilon(x)}{qd} \left( V_{gs} - \varphi_b(x) + \Delta\varphi_c(x) + \frac{qN_d d^2}{2\varepsilon(x)} + \frac{\sigma(x)}{\varepsilon(x)} - \frac{E_F}{q} \right). \quad (26)$$

Each term can be analyzed with respect to the potential effect of irradiation on its contribution to the 2DEG concentration, in order to determine the major contributors to post-irradiation changes in current.

The aluminum molar fraction dependent dielectric constant,  $\varepsilon(x)$ , is largely independent of irradiation. Alloy disorder may have some effect on the dielectric constant but not at a level substantial enough for a perceptible change to the carrier concentration for the neutron fluences used in this study. White, *et al.* [51] used Secondary Ion Mass Spectroscopy (SIMS) to relate the reduced mobility in similar HFETs after 1.0 MeV proton irradiation. They observed a negligible increase in interface thickness, indicating alloy disorder, below a fluence of  $10^{14}$  p<sup>+</sup>/cm<sup>2</sup>. Above  $10^{14}$  p<sup>+</sup>/cm<sup>2</sup> they observed a substantial increase that was fluence dependent and a commensurate decrease in 2DEG mobility. The highest fluence of 1.0 MeV(eq) neutrons used in this study is  $10^{13}$  n/cm<sup>2</sup> and the damage constants of identical energy protons and neutrons are similar. Hence the fluence levels in this study are not high enough to cause enough alloy disorder to affect the mobility.

The gate-to-source voltage,  $V_{gs}$ , is an externally controlled parameter and is thus independent of irradiation. The conduction band discontinuity,  $\Delta\varphi_c$ , is established by the aluminum mole fraction, a material parameter, and also is not affected by irradiation, except secondarily through alloy disorder, i.e. aluminum displacement migrating into the GaN. This is again a minor effect. The Fermi level,  $E_F$ , is not substantially changed by irradiation for the same reasons.

Changes to the Schottky barrier height,  $\phi_b(x)$ , the doping density in the AlGaN,  $N_d$ , and the induced sheet charge density,  $\sigma(x)$ , are thus the primary factors potentially influenced by irradiation, and may be important contributors to changes in the carrier concentration after irradiation. The height of the Schottky barrier between the AlGaN layer and the gate metal in a device is determined by the bandgap and doping level of the AlGaN and the difference necessary to align the Fermi level in the AlGaN to the work function of the metal as shown in Figure 3(b). This is directly influenced by the aluminum content of the AlGaN.

Irradiation produces defects that act as trapping states allowing electrons to travel through the barrier via trap-assisted tunneling and hence virtually lowering the barrier height. Deep level defects produced in the AlGaN by electron irradiation have been identified [39] that may increase tunneling. Two potential electron traps that are present in AlGaN and enhanced by irradiation are of particular concern: the nitrogen vacancy at 0.85 eV below the conduction band edge in GaN (and hence AlGaN) [41] and the two irradiation induced electron traps at 0.33 and 0.38 eV below the band edge [42]. Both these traps were discussed in the previous section.

Irradiation also can change the doping density,  $N_d$ , of AlGaN. The heterostructures under investigation have an as-grown n-type doping, primarily from intrinsic Ga defects. The creation of additional donors following irradiation will increase this doping level and therefore raise the Fermi level. Creation of acceptors will compensate the existing donors leading to a decrease in the doping level and carrier concentration. Depending upon the defect type created by radiation there can be an

increase or decrease in donors and therefore carrier concentration. This type of damage is expected to be a significant contributor to changes in the carrier density.

The most significant changes to the carrier density following irradiation are due to changes in the induced sheet charge density,  $\sigma(x)$ . Positively charged defects in the AlGa<sub>N</sub> and negatively charged defects in the GaN increase the field in the well region leading to an increase in the carrier concentration. Negatively charged defects in the AlGa<sub>N</sub> and positively charged defects in the GaN have the opposite effect. By varying the temperature during irradiation and the energy of the radiation particles the experiments can cause displacements of the different constituent atoms resulting in defects of both polarities in the component semiconductors.

## IV. Experimental Procedures

The AlGaN/GaN HFETs used in this research were constructed from an AlGaN/GaN heterostructure wafer manufactured by Cree Inc. The wafer was produced using the metal-organic vapor-phase epitaxy (MOVPE) process with a substrate of 4H-SiC, a nucleation and buffer layer of GaN and an epilayer of  $\text{Al}_{0.27}\text{Ga}_{0.73}\text{N}$  (27% mole fraction of AlN and 73% mole fraction of GaN). The transistor dimensions are: the SiC substrate is  $413\ \mu\text{m}$  thick; the GaN Cree proprietary nucleation and buffer layer over the substrate has a nominal thickness of  $2\ \mu\text{m}$  and the  $\text{Al}_{0.27}\text{Ga}_{0.73}\text{N}$  layer over the GaN is  $25\ \text{nm}$  as shown in Figure 16 after construction. The gate, drain and source contacts have been added to the figure for illustration but are applied during HFET fabrication not during epilayer deposition. The GaN and AlGaN layers are nominally undoped with a room temperature channel carrier concentration of  $1.3 \times 10^{13}\ \text{cm}^{-2}$  and mobility of  $1300\ \text{cm}^2/\text{V}\cdot\text{s}$  as measured by the manufacturer.

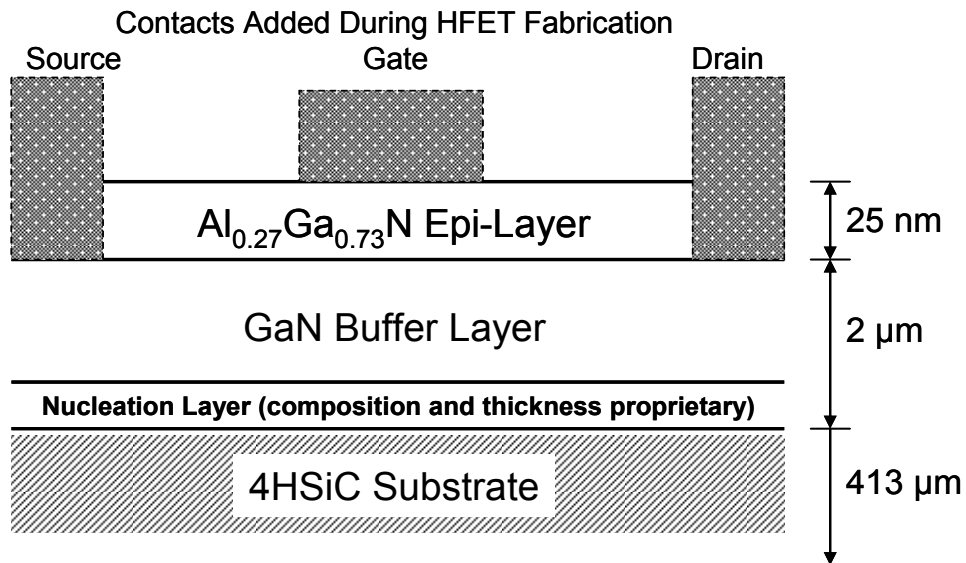


Figure 16. Heterostructure layer composition showing the location of contacts to be added during HFET fabrication.



## 4.1 Device Preparation

The fabrication of the HFET from the AlGaN/GaN heterostructure was performed at the Air Force Research Laboratories (AFRL) Sensors Directorate, Aerospace Components and Subsystems Technology Electron Devices Branch (RYDD). Sattler [31] provides a description of the original fabrication process in his thesis work. The RYDD standard GaN baseline process was used to produce a series of HFETs and test structures on multiple reticles. Transistors were produced using an HFET research mask layout with a  $25 \times 25$  array of HFETs on the reticle and metal deposited using a low-temperature vapor technique. A portion of one reticle is as shown in Figure 17.

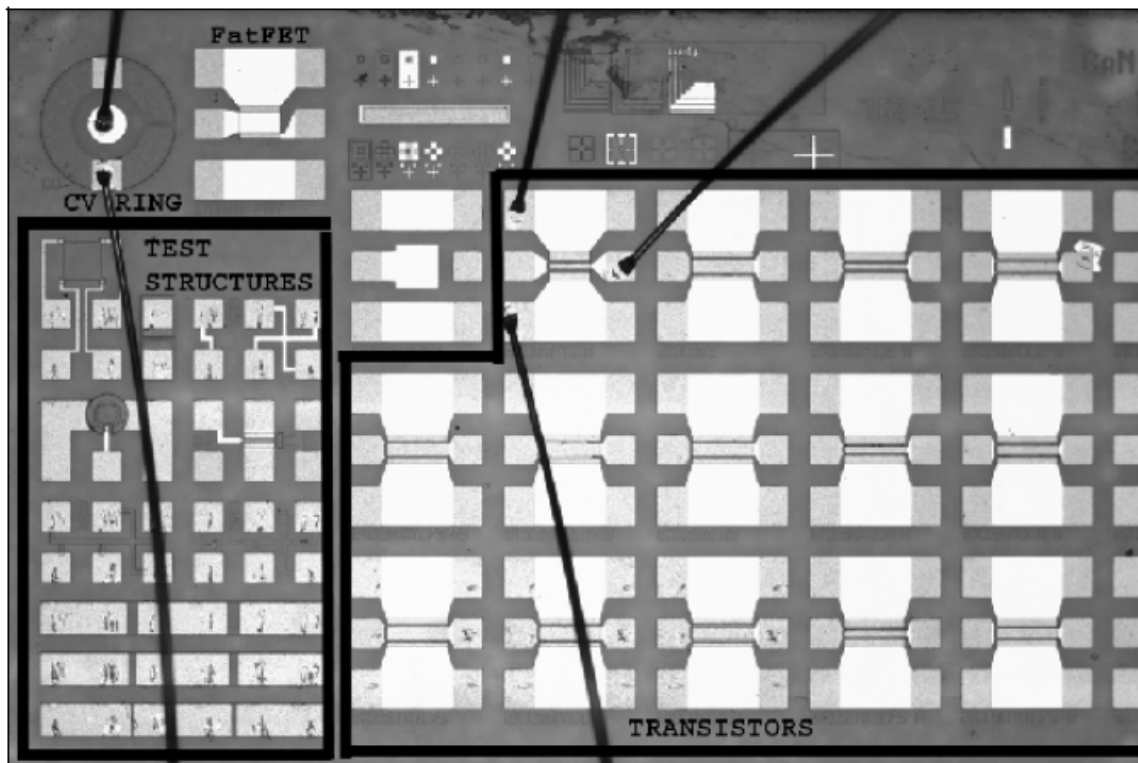


Figure 17. Photograph of a reticle showing the HFET structures used in this research.

The FATFET in the upper left hand corner of the photograph was the device used in each of the irradiation experiments. The gate length of the FATFET is  $50 \mu\text{m}$  as shown

in Figure 19. The other devices on the HFET chip have gate lengths of  $1.2\ \mu\text{m}$ . The FATFET was used in this research to increase the cross section of the gate region that would be irradiated. The source and drain ohmic contacts consisted of the deposition of four metals:  $350\ \text{\AA}$  titanium,  $2300\ \text{\AA}$  aluminum,  $500\ \text{\AA}$  nickel, and  $200\ \text{\AA}$  gold. The gate Schottky contact was formed by deposition of  $200\ \text{\AA}$  nickel and  $2800\ \text{\AA}$  gold. The passivated devices had a passivation layer of  $150\ \text{nm}$  of SiN deposited on the exposed AlGaN surface between the gate and the drain and source contacts. The unpassivated device fabrication did not include this step and the AlGaN surfaces between the contacts were left exposed.

Figure 18 shows the orientation of the gate, source and drain contacts on the device. The vertical line corresponds to the cross section diagram of Figure 19 that shows the detailed construction of the FATFET with dimensions.

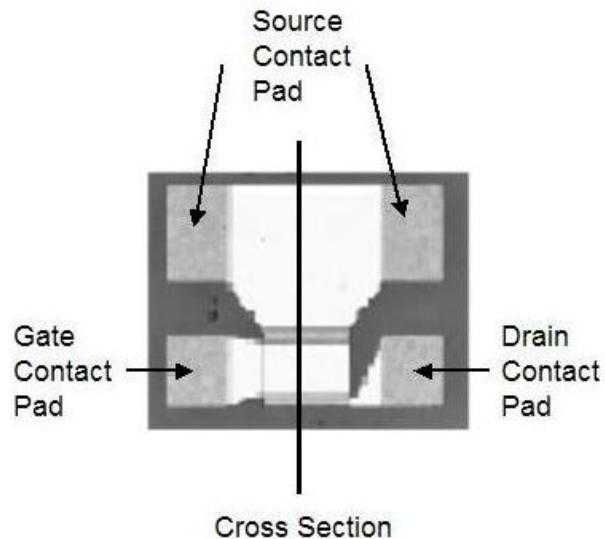


Figure 18. Top view of the FATFET used in the irradiation experiments showing the cross section line depicted in Figure 19.

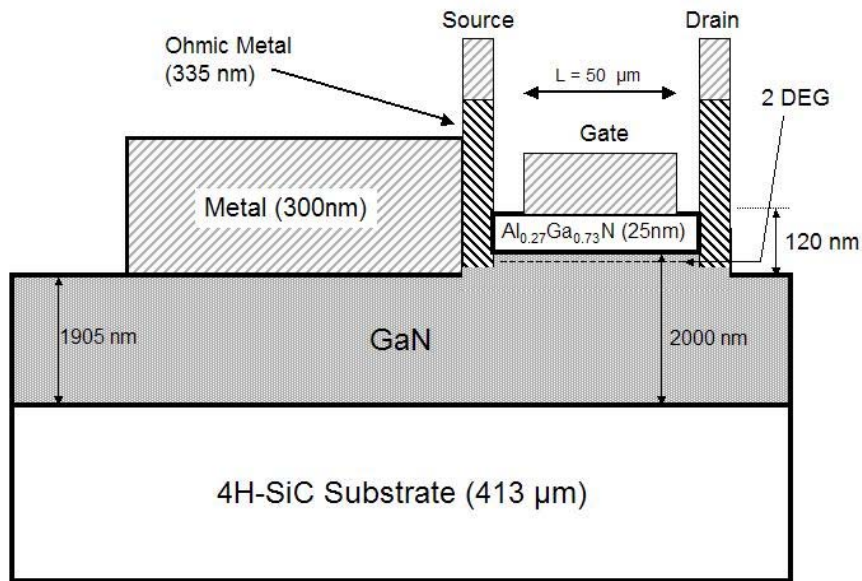


Figure 19. Cross section of the device used in the irradiation experiments.

The FATFETs were packaged for use as experimental test structures. The packaging process involved physically bonding the reticle to the package bottom and wire-bonding the desired transistors so that they were appropriately connected to the package pins. The samples were diced and mounted in 14-pin unsealed flat packs. The topsides of the reticles were left uncovered to allow radiation unimpeded access to the transistors. Figure 20 shows the packaging used while Figure 21 is a more detailed photograph showing the location of the FATFET on the chip and the wiring to the gate (G), source (S), and drain (D) contacts.

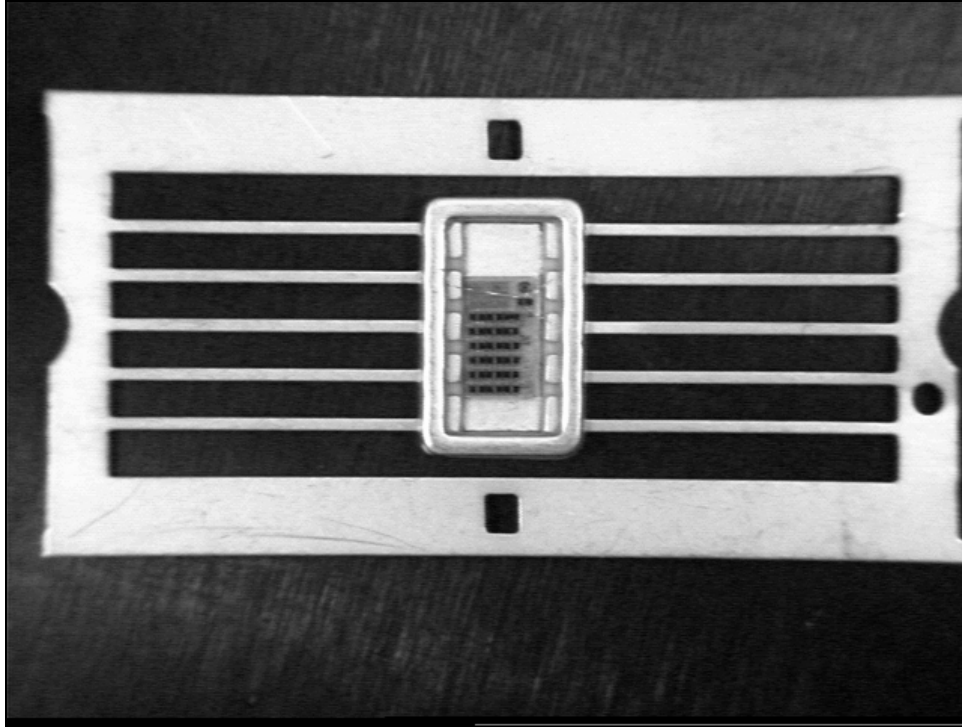


Figure 20. Diced and packaged reticle ready for experimental testing.

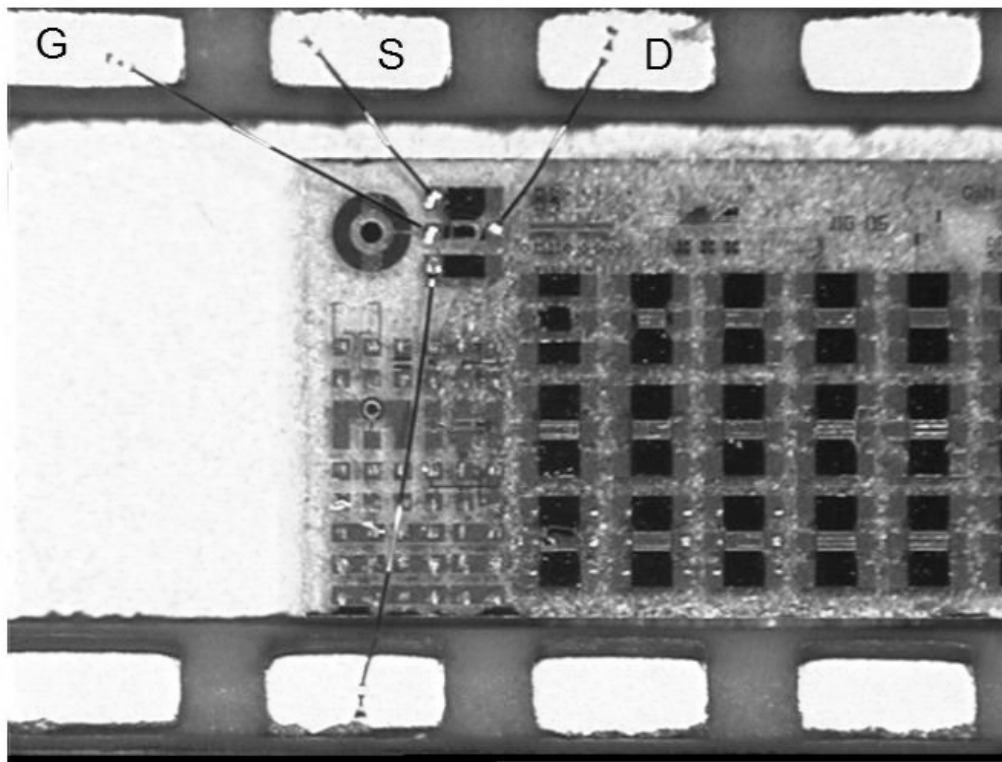


Figure 21. Detail of the wire connection to the gate, source, and drain of the FATFET on the reticle chip.

## 4.2 Data Collection

The measurements performed on the HFETs consisted of the following electrical measurements:

1. Incremental sweeps of the drain current vs. drain voltage at fixed gate voltages ( $I_{ds}$ - $V_{ds}$ ). At a fixed temperature, a gate-to-source bias voltage was set by one voltage source. A second voltage source set the incremental voltage from drain-to-source and the current from drain-to-source was measured. The gate voltage was then reset to another value and the HFET was heated or cooled to the next predetermined temperature to allow subsequent drain voltage sweeps.
2. Sweep of the gate current vs. gate voltage at zero bias drain-to-source ( $I_{gs}$ - $V_{gs}$ ). The source and drain leads were grounded together. At a fixed temperature, a voltage source set the incremental gate-to-source voltage and the current from gate-to-source was measured.
3. Incremental sweep of the gate current vs. temperature at fixed gate voltages and zero bias drain-to-source ( $I_g$ - $T$ ). The source and drain leads were connected together and grounded. A voltage source set the incremental gate-to-source voltage and the current from gate-to-source was measured at a fixed temperature. The device was heated or cooled to the next predetermined temperature and the measurement repeated.
4. Sweeps of the gate capacitance vs. gate voltage at zero bias drain-to-source ( $C$ - $V$ ). The source and drain were connected and a small-amplitude, high frequency AC voltage was applied with both DC and AC voltage sources connected to a common ground. At a fixed temperature, a voltage source applied an incremental bias to the gate and the capacitance across the gate was measured.
5. Sweeps of the conductance through the gate vs. gate voltage at zero bias drain-to-source ( $g_g$ - $V$ ). Gate conductance was measured in the same manner as the C-V measurements.

The current measurements were collected using either one or two Keithley 237 Source Measurement Units (SMU) depending upon the measurement. The capacitance and gate conductance measurements used the Keithley 590 Capacitance-Voltage Analyzer (C-V). Temperature was controlled with a Lakeshore 331 Temperature Controller using either a resistive temperature detector (RTD) (electron irradiation experiments) or a twisted wire thermocouple (neutron irradiation experiments) and an Omega ceramic heating element. All measurement equipment was controlled by laptop computer via a National Instruments General Purpose Interface Bus (GPIB). Control software included both National Instruments Labview [62] and National Instruments Measurement and Automation Explorer [63] with Microsoft Visual Basic [64].

## **Pre-irradiation Characterization**

Pre-irradiation characterization was used to:

- Ensure that the equipment and procedures would properly collect the post-irradiation data.
- Provide a baseline measurement for comparison with post-irradiation results.
- Determine which HFETs operated within the normal bounds and to classify each HFET with respect to levels of drain-to-source current, gate leakage current, capacitance, and response to temperature. HFETs that did not perform to standard were rejected from consideration and not irradiated.
- Provide data for the trap-assisted-tunneling model to compare the model to experimental data and to explore the effect of passivation on HFET behavior.
- Provide the data necessary to determine the uncertainty in the data for the construction of error bars.

The passivated and unpassivated HFETs that were irradiated with neutrons were pre-characterized using  $I_{ds}$ - $V_{ds}$ ,  $I_{gs}$ - $V_{gs}$ ,  $I_g$ - $T$ ,  $C$ - $V$ , and  $g_g$ - $V_g$ . The particular devices measured are described in Chapter 5. Pre-irradiation characterization included:

- $I_g$ - $T$  measurements at gate-to-source voltages ( $V_{gs}$ ) of -2, -3, and -4 V and temperatures of 82 to 300 K temperature increments of 2 K.
- $I_{ds}$ - $V_{ds}$  measurements at gate-to-source voltages ( $V_{gs}$ ) of -2, -3, and -4 V and drain-to-source voltages ( $V_{ds}$ ) of 0 to 8 volts with voltage increments of 0.2 V at 80 K, 140 K, 200 K, and at 300 K.
- $I_{gs}$ - $V_{gs}$  at  $V_{gs}$  of 0 to -4 volts at increments of 0.2 V at 80 K, 140 K, 200 K, and at 300 K.
- $C$ - $V$  and  $g_g$ - $V_g$  measurements were made across the heterojunction from the gate to the source at 1 MHz for  $V_{gs}$  from 0 to -6 V at 0.125 V increments at 80 K, 140 K, 200 K, and 300 K.

All pre- and post-irradiation measurements were performed using the same measurement apparatus with the HFETs affixed to the aluminum fin that is described below.

The unpassivated HFETs that were irradiated with electrons were pre-characterized using  $I_{ds}$ - $V_{ds}$  and  $I_{gs}$ - $V_{gs}$  measurements by Sattler [31].  $C$ - $V$  pre-characterization was performed by Jarzen [65]. Separate HFETs were used for the  $I$ - $V$  and  $C$ - $V$  measurements with the particular devices used described in Chapter 5. Pre-irradiation characterization included  $I_{ds}$ - $V_{ds}$  measurements at gate-to-source voltages ( $V_{gs}$ ) of -1, -2, and -3 V and drain-to-source voltages ( $V_{ds}$ ) of 0 to 10 volts at increments of 0.1 V at 85 K and at RT.  $C$ - $V$  measurements were made across the heterojunction from the gate to the source at 1 MHz for  $V_{gs}$  from 0 to -6 V at increments of 0.2 V at a

temperature of 85 K. The source and drain terminals were connected together during the C-V measurements. All pre- and post-irradiation measurements were performed using the same measurement apparatus with the HFETs affixed to the cold head that is described in the next section.

## **Neutron Irradiation Equipment**

The neutron irradiation experiments took place at the Ohio State University Research Reactor (OSURR). The OSURR is a Uranium reactor surrounded by a 20 foot deep pool of water. The pool provides cooling, neutron moderation, and gamma shielding. A vertical irradiation chamber developed by Gray [66] was used for these experiments. The irradiation chamber consists of a 20.5' long, 7" outside diameter aluminum tube (6061 T6 aluminum) with walls 0.125" thick. The chamber was moved into contact with the reactor with the top of the chamber tube against a bracket during each experiment. The chamber allowed access to the high neutron flux position adjacent to the reactor core while allowing easy access for the samples and mounting apparatus. The basic configuration is shown in Figure 22.



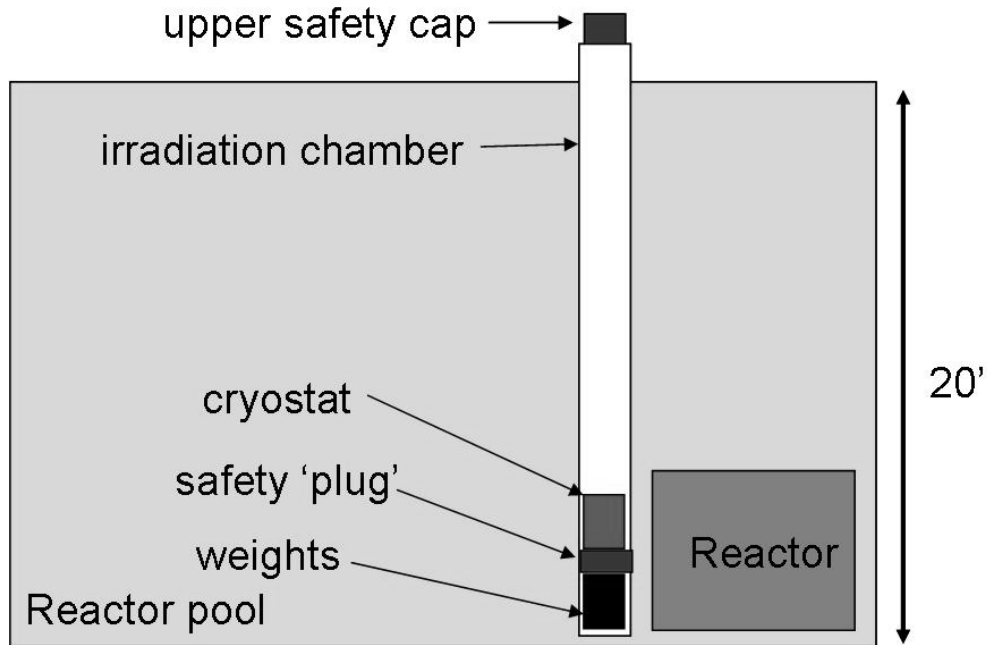


Figure 22. Configuration of OSURR reactor and irradiation chamber [66].

The HFETs were affixed to an aluminum fin which was held upright in a glass dewar filled with liquid nitrogen. A twisted wire thermocouple temperature sensor was attached to the fin adjacent to the sample mounting bracket to monitor temperature. A ceramic resistive heater was inserted into the top of the fin to control the temperature. A portion of the fin below the devices was milled to approximately 0.03" to reduce the rate at which heat was conducted away from the devices and enable the 10 watt heater to provide a greater temperature range. The devices, sensors, and heaters were surrounded in Styrofoam and wrapped in fabric tape to reduce ice formation and temperature change due to convection. The fin was placed upright in the glass dewar filled to the top of the milled section of the fin with liquid nitrogen with the devices in the top section. The dewar was wrapped in cadmium (Cd) and small cadmium and lead plates were mounted between the HFETs and the reactor to minimize thermal neutrons and gamma rays. The design of the aluminum fin is shown in Figure 23.

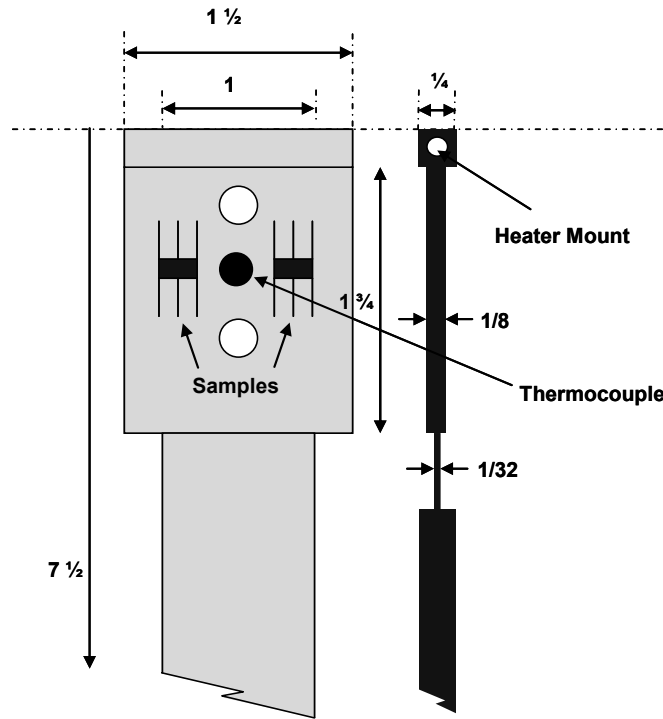


Figure 23. Aluminum fin used for mounting samples in neutron flux from the reactor.

In order to reduce neutron activation, the HFETs were shielded with cadmium. Ignoring resonance absorption lines, Cd has nearly a 4 order of magnitude increase in neutron absorption cross section below neutron energy of 0.2 eV [67]. Neutrons of energy greater than about 1.5 eV pass through Cd with little attenuation ignoring the resonance absorption as shown in Figure 24.

Although activation can be reduced with proper choices of shielding, fission gamma rays are a significant source of additional accumulated dose and are difficult to avoid. Gamma irradiation during neutron irradiation was reduced with shielding by a 1 mm lead shield although this also reduces the neutron fluence.

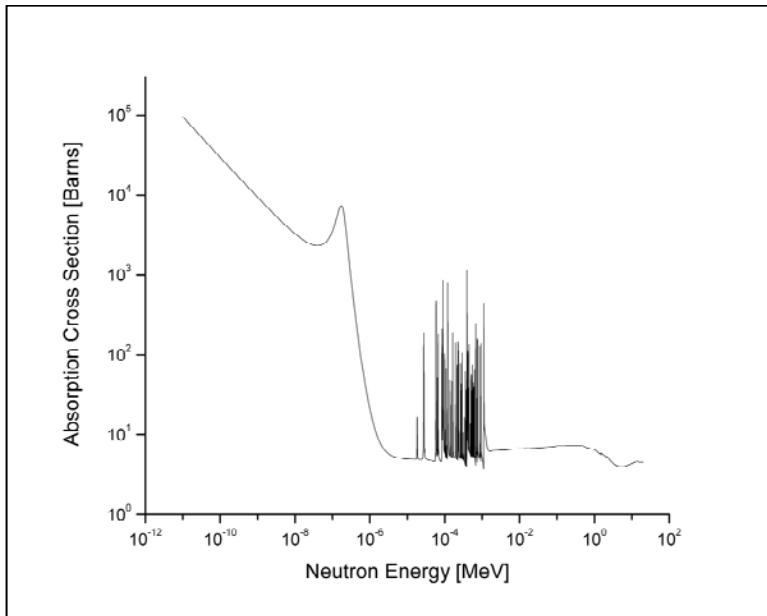


Figure 24. Absorption cross section of cadmium.

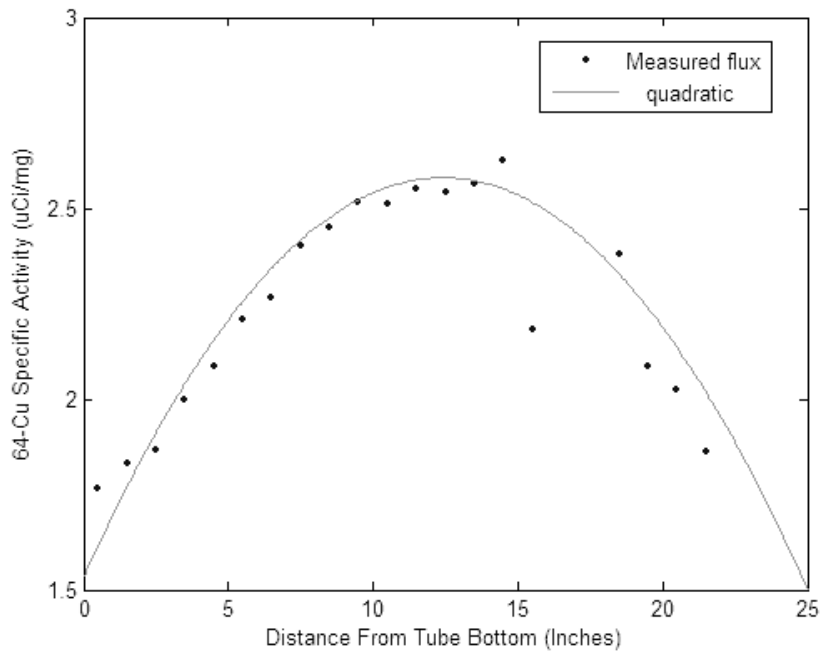


Figure 25. Irradiation chamber neutron flux profile.

Dosimetry was performed by Gray [66] measuring both the total neutron flux and the spectrum. The flux profile in the irradiation chamber was measured by irradiating a copper wire, held vertically in the bottom 25 inches of the chamber and measuring the

activity of segments of the wire at one inch intervals. A distance of 13 inches from the bottom of the tube was selected in order to maximize the neutron flux. All irradiations were made with devices at this position. The flux profile is given in Figure 25.

The neutron spectrum was measured by activation analysis. Gold, copper and cobalt wires were irradiated at the position where the devices were to be attached on the fin in the cryostat. The cryostat was wrapped in cadmium and placed at the same position in the irradiation chamber that would be used for the experiment. One wire set was bare and the other was enclosed in cadmium. The reactor was operated for one hour at 50 kW. The wires were removed and their activities were counted using a high purity germanium gamma detector. The resulting neutron spectrum is shown in Figure 26.

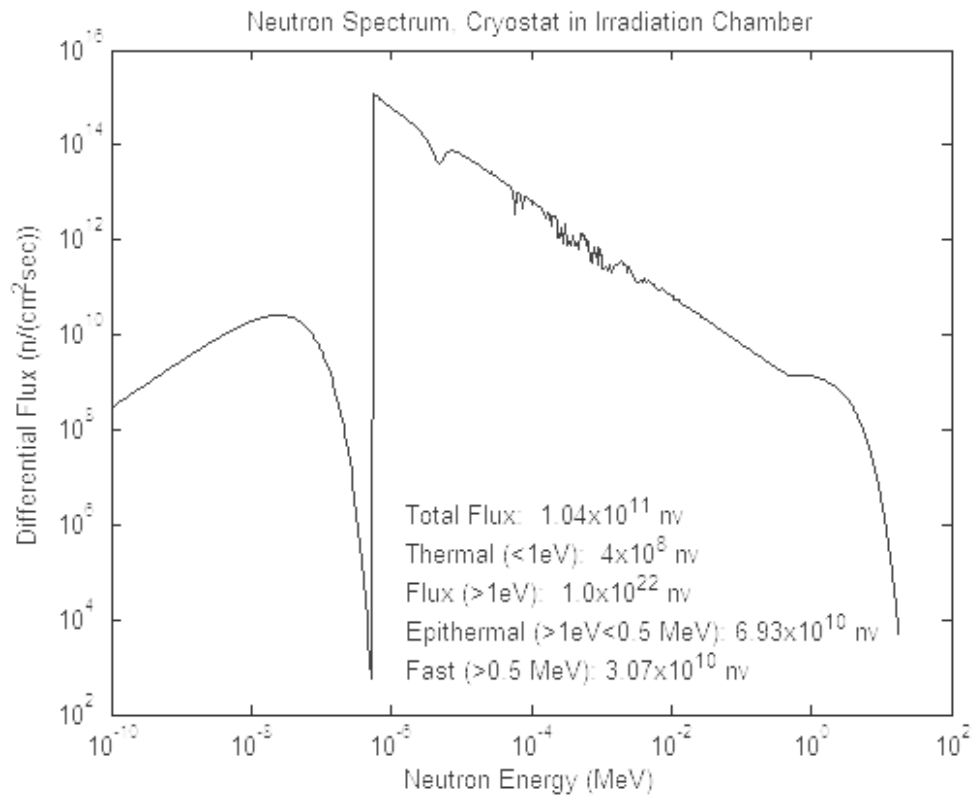


Figure 26. Neutron spectrum inside the cryostat.

At 450 kW power, a neutron flux of  $3.1 \times 10^{10}$  n/cm<sup>2</sup>-s of >0.5 MeV neutrons was measured. Neutron flux is linearly proportional to reactor power. Because of uncertainty in the measurement of the spectrum the fluence has an error of greater than 25%. For the purpose of this experiment, however, what is important is the reproducibility of the neutron damage effect on the HFETs for each irradiation, which is estimated to have an error less than 10%, primarily due to uncertainty in the orientation of the HFETs in the irradiation chamber. The fluence used in this experiment, based on times of irradiation and reactor power, will be discussed in Section 4.3.

## **Electron Irradiation Equipment**

The electron irradiation experiments were carried out by Sattler [31] and Jarzen [65] at the Wright State University (WSU) Van de Graaff accelerator shown in Figure 27. The accelerator produces electrons in a range from 400 keV to 1.8 MeV with beam currents at and below 30  $\mu$ A in an aperture area of 3.3 cm<sup>2</sup> with the beam line evacuated to  $>9 \times 10^{-6}$  torr. The temporal current deviation is estimated at  $\pm 3\%$ , the spatial beam uniformity is  $\pm 2-3\%$ , and the temporal energy deviation is estimated at  $\pm 5\%$  [27]. Beam current is used to control the flux with the total fluence determined through current integration.

The HFETs were affixed to a cold head sample mount assembly for irradiation as shown in Figure 28. The cold head was used to maintain the devices at low temperature  $\sim 85$  K during irradiation and allowed electrical lead access to the devices for measurements while they were maintained in vacuum and at low temperature. The cold head enabled temperature monitoring during irradiation via an implanted RTD.

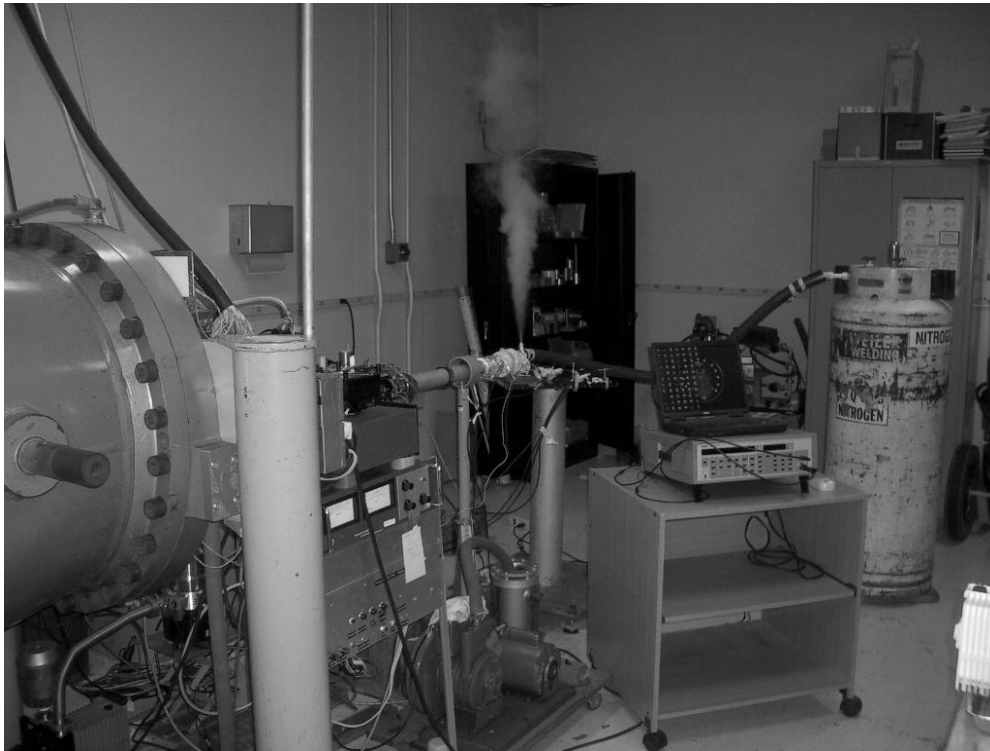


Figure 27. Van de Graaff facility at Wright State University [65].

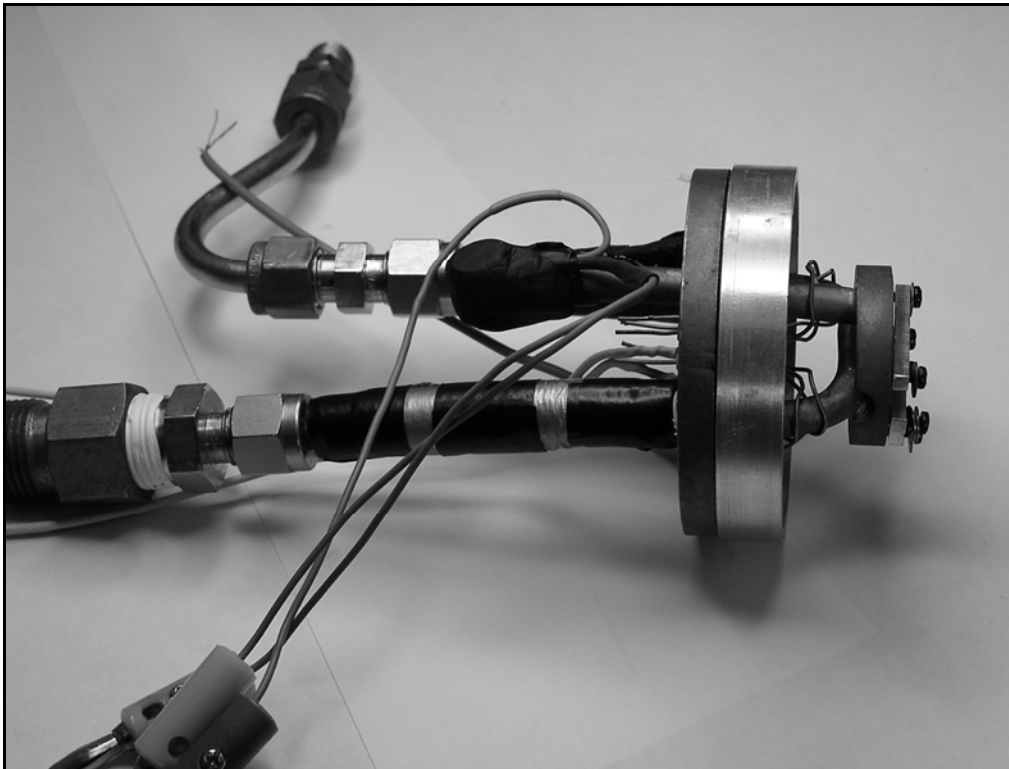


Figure 28. Cold head and mounting assembly used in the Van de Graaff accelerator [27].

The devices were attached to the cold head by physically clamping the package to the front face of the cold head and applying conductive grease to ensure a good thermal connection with the cold head in order to maintain the device at a low temperature. The leads of the samples were grounded to prevent transient currents produced by the electron beam from damaging the HFETs. The cold head with the HFET samples attached was mounted at the end of the beam line. Temperatures of approximately 85 K were maintained during irradiation by liquid nitrogen flowing through the cold head.

### 4.3 Irradiations

There were three irradiation series one using electrons from the WSU Van de Graaff accelerator and two using neutrons from the OSU research reactor. A total of 26 HFETs were irradiated, 19 unpassivated and 7 passivated. Each of the irradiation series are detailed below with the primary measurements made during and after irradiation.

The details of the electron irradiations are summarized in Table 6. In all cases, the devices were irradiated at  $\sim 85$  K and  $9 \times 10^{-6}$  Torr while mounted to the cold head.

Table 6. Electron Irradiation Experiments Summary

Sample	Energy (MeV)	Beam Current ( $\mu\text{A}$ )	Total Dose ( $\text{e}^-/\text{cm}^2$ )	Irradiation Time (min)
A08-IV	0.45	0.13	$1.0 \times 10^{14}$	7
A08-IV	0.45	0.13	$3.0 \times 10^{14}$	20
A09-IV	0.45	0.3	$3.0 \times 10^{14}$	8
A09-IV	0.45	0.3	$9.7 \times 10^{14}$	21
A09-IV	0.45	0.3	$1.87 \times 10^{15}$	39
A09-IV	0.45	0.3	$3.67 \times 10^{15}$	89
A16-CV	0.45	1.0	$3.3 \times 10^{14}$	2.2
A01-CV	0.45	0.15	$3.5 \times 10^{12}$	3

Irradiation was accomplished in stages, with the electron beam turned off during each measurement but with the device remaining under vacuum and in contact with the cold head. After each irradiation, the I-V and C-V measurements were repeated at 85 K. After the final irradiation and measurement cycle, a 21 minute RT anneal was performed on sample A09. Following the anneal, the  $I_{ds}$  and  $I_{gs}$  measurements were repeated at RT.

The first set of neutron irradiations was designed to test response, repeatability, minimum damage level, and saturation. The devices were mounted on the aluminum fin held in a liquid nitrogen bath and placed adjacent to the reactor core. The temperature was maintained at  $84\pm 2$  K during irradiation. The device fixture was surrounded by cadmium and the lead and cadmium shields were emplaced. Dosimetry was performed by activation foil analysis, as described in the previous section, and confirmed using a Monte-Carlo (MCNP) model. Six devices were irradiated: four devices (Set #1) with an initial 1 MeV equivalent neutron exposure of  $4\times 10^{11}$  n/cm<sup>2</sup> and a subsequent exposure to  $1\times 10^{12}$  n/cm<sup>2</sup>, and two devices (Set #2) with an initial exposure to  $3\times 10^{10}$  n/cm<sup>2</sup> and subsequent exposures of  $4\times 10^{11}$ ,  $1\times 10^{12}$ , and  $5\times 10^{12}$  n/cm<sup>2</sup>. The irradiations are summarized in Table 7. The doses are accurate to  $\pm 0.5$  per order of magnitude.



Table 7. First Neutron Experiment Irradiations Summary

Sample	Reactor Power (kW)	Irradiation Time (min)	Total Dose (1 MeV(eq) n/cm <sup>2</sup> )
JM19	4.3	27	$4.0 \times 10^{11}$
	9.0	27	$1.0 \times 10^{12}$
JM22	0.27	27	$3.0 \times 10^{10}$
	4.3	27	$4.0 \times 10^{11}$
	9.0	27	$1.0 \times 10^{12}$
	45	27	$5.0 \times 10^{12}$
JM23	4.3	27	$4.0 \times 10^{11}$
	9.0	27	$1.0 \times 10^{12}$
JM24	4.3	27	$4.0 \times 10^{11}$
	9.0	27	$1.0 \times 10^{12}$
JM27	4.3	27	$4.0 \times 10^{11}$
	9.0	27	$1.0 \times 10^{12}$
JM28	0.27	27	$3.0 \times 10^{10}$
	4.3	27	$4.0 \times 10^{11}$
	9.0	27	$1.0 \times 10^{12}$
	45	27	$5.0 \times 10^{12}$

The measurements conducted during and after irradiations for the first neutron irradiation experiment are summarized in Table 8.

Table 8. First Neutron Experiment Measurements Summary

Sample	Gate Current vs. Temp ( $I_{gs}$ -T at $V_g = -2, -3, -4$ V and 0 $V_{ds}$ )	Transistor Curves ( $I_{ds}$ vs. $V_{ds}$ at $V_{gs} = -2, -3, -4$ V)	Capacitance Curves (C- $V_g$ at $V_{ds} = 0$ V)
JM19	Post $4.0 \times 10^{11}$ at 82-86 K Post $1.0 \times 10^{12}$ at 82-294 K	PreIrrad Post $4.0 \times 10^{11}$ at 82 K Post $1.0 \times 10^{12}$ at 82 K Post $1.0 \times 10^{12}$ at 294 K	-
JM22	Post $3.0 \times 10^{10}$ at 82-84 K Post $4.0 \times 10^{11}$ at 82-84 K Post $1.0 \times 10^{12}$ at 82-212 K Post $5.0 \times 10^{12}$ at 82-294 K Post 3 wk at RT 82-294 K	PreIrrad Post $3.0 \times 10^{10}$ at 82 K Post $4.0 \times 10^{11}$ at 82 K Post $1.0 \times 10^{12}$ at 82 K Post $5.0 \times 10^{12}$ at 82 K Post $5.0 \times 10^{12}$ at 294 K Post 3 wk at RT, 82 K Post 3 wk at RT, 294 K	Post 3 week anneal
JM23	Post $4.0 \times 10^{11}$ at 82-204 K Post $1.0 \times 10^{12}$ at 82-294 K Post 1 wk at RT 82-294 K	PreIrrad Post $4.0 \times 10^{11}$ at 82 K Post $1.0 \times 10^{12}$ at 82 K Post $1.0 \times 10^{12}$ at 294 K Post 1 wk at RT, 82 K Post 1 wk at RT, 294 K	Post 1 week anneal
JM24	Post $4.0 \times 10^{11}$ at 82-204 K Post $1.0 \times 10^{12}$ at 82-294 K Post 1 wk at RT 82-294 K	PreIrrad Post $4.0 \times 10^{11}$ at 82 K Post $1.0 \times 10^{12}$ at 82 K Post $1.0 \times 10^{12}$ at 294 K Post 1 wk at RT, 82 K Post 1 wk at RT, 294 K	Post 1 week anneal
JM27	Post $4.0 \times 10^{11}$ at 82-86 K Post $1.0 \times 10^{12}$ at 82-294 K	PreIrrad Post $4.0 \times 10^{11}$ at 82 K Post $1.0 \times 10^{12}$ at 82 K Post $1.0 \times 10^{12}$ at 294 K	-
JM28	Post $3.0 \times 10^{10}$ at 82-84 K Post $4.0 \times 10^{11}$ at 82-84 K Post $1.0 \times 10^{12}$ at 82-212 K Post $5.0 \times 10^{12}$ at 82-294 K	PreIrrad Post $3.0 \times 10^{10}$ at 82 K Post $4.0 \times 10^{11}$ at 82 K Post $1.0 \times 10^{12}$ at 82 K Post $5.0 \times 10^{12}$ at 82 K Post $5.0 \times 10^{12}$ at 294 K	-

The second set of neutron irradiations was designed to test response, repeatability, minimum and maximum damage level, and saturation of the effects. It was also designed to collect data for model validation. Capacitance vs. voltage measurements were taken throughout the irradiation cycle unlike in neutron experiment #1. Both passivated and unpassivated HFETs were irradiated and measured to observe their respective response. The experimental set up was nearly identical to neutron experiment #1. The HFETs were mounted on the larger aluminum fin shown in Figure 23, held in a liquid nitrogen bath and placed adjacent to the reactor core. The temperature was maintained at  $84\pm 2$  K during irradiation. The device fixture was again surrounded by lead and cadmium shields. Twelve devices were irradiated in sets of two; one passivated HFET and one unpassivated HFET:

- Set #1 with an initial 1 MeV equivalent neutron exposure of  $2\times 10^9$  n/cm<sup>2</sup>, a subsequent exposure to  $1\times 10^{10}$  n/cm<sup>2</sup>, and a third exposure to  $1\times 10^{11}$  n/cm<sup>2</sup>.
- Set #2 with an initial 1 MeV equivalent neutron exposure of  $2\times 10^9$  n/cm<sup>2</sup> and a subsequent exposure to  $1\times 10^{13}$  n/cm<sup>2</sup>.
- Set #3 with a 1 MeV equivalent neutron exposure of  $1\times 10^{10}$  n/cm<sup>2</sup>.
- Set #4 with a 1 MeV equivalent neutron exposure of  $1\times 10^{11}$  n/cm<sup>2</sup>.
- Set #5 with a 1 MeV equivalent neutron exposure of  $1\times 10^{12}$  n/cm<sup>2</sup>.
- Set #6 with an initial 1 MeV equivalent neutron exposure of zero n/cm<sup>2</sup> and a subsequent exposure to  $1\times 10^9$  n/cm<sup>2</sup>.

The irradiations are summarized in Table 9 and the measurements in Table 10.

Table 9. Second Neutron Experiment Irradiations Summary

Sample	Reactor Power (kW)	Irradiation Time (min)	Total Dose (1 MeV(eq) n/cm <sup>2</sup> )
JM31	0.05	10	$2.0 \times 10^9$
	0.09	27	$1.0 \times 10^{10}$
	0.90	27	$1.0 \times 10^{11}$
JM41	0.05	10	$2.0 \times 10^9$
	0.09	27	$1.0 \times 10^{10}$
	0.90	27	$1.0 \times 10^{11}$
JM32	0.05	10	$2.0 \times 10^9$
	90.0	27	$1.0 \times 10^{13}$
JM111	0.05	10	$2.0 \times 10^9$
	90.0	27	$1.0 \times 10^{13}$
JM29	0.09	27	$1.0 \times 10^{10}$
JM42	0.09	27	$1.0 \times 10^{10}$
JM26	0.90	27	$1.0 \times 10^{11}$
JM110	0.90	27	$1.0 \times 10^{11}$
JM16	9.0	27	$1.0 \times 10^{12}$
JM34	9.0	27	$1.0 \times 10^{12}$
JM18	none	27	zero
	0.025	10	$1.0 \times 10^9$
JM210	none	27	zero
	0.025	10	$1.0 \times 10^9$





#### 4.4 Modeling Optimization Procedure

The TAT current is determined by simultaneously solving for  $I_{TAT}$  as a function of temperature at a fixed voltage and as a function of voltage at a fixed temperature. The  $I_{TAT}$  integral and its factors are functions of the six variables as given by,

$$I_{TAT} (T, V_g, N_d, N_t, \phi_t, \phi_{b0}) = \frac{qAC_t(\phi_t)N_t}{\mathcal{E}(V_g, N_d, \phi_{b0})} \times \int_{\phi_t}^{\phi_b(T, V_g, N_d, \phi_{b0}) + |V_g|} \left( \frac{1}{f_{FD}(\phi, T, V_g, N_d, \phi_{b0})P_1(\phi, V_g, N_d, \phi_t, \phi_{b0})} + \frac{1}{P_{2\_triangle}(V_g, N_d, \phi_t, \phi_{b0})} \right)^{-1} d\phi. \quad (27)$$

In order to determine the parameters in the model developed in [55, 57], an optimization process was developed.

The optimization procedure was to compare the calculated  $I_{TAT}(V_g)$  and  $I_{TAT}(T)$  against experimental  $I_g-V_g$  data measured at a fixed temperature and  $I_g-T$  data measured at a fixed gate voltage. For the  $I_g-V_g$  data and hence the  $I_{TAT}(V_g)$  calculation the range 0 to -4 volts was used for the gate voltage. This voltage range spans the reverse bias range of the device from essentially no current through the gate at 0 volts to a maximum gate current just below the threshold voltage. The temperatures set during the  $I_g-V_g$  measurements and  $I_{TAT}(V_g)$  calculations were 80, 140, 200, and 300 K. These values spanned the temperature range from liquid nitrogen temperature to room temperature at nearly equal intervals.

For the  $I_g-T$  data and hence the  $I_{TAT}(T)$  calculation the range 80 to 300 K was used for the temperature. This temperature range spans the normal operating range of these devices in a space environment. The gate voltages set during the  $I_g-T$  measurements and  $I_{TAT}(T)$  calculation were -2, -3, and -4 V. The reverse bias gate current is very low, below -2 V on the gate, providing little additional information on the model and -4 V on the gate puts the HFETs just above their threshold voltages. Initial values were set for the remaining four variables,  $N_d$ ,  $N_t$ ,  $\phi_t$ , and  $\phi_{b0}$ .

Each variable is adjusted sequentially within a limited set of values to optimize the fit to both  $I_g$ - $T$  and  $I_g$ - $V_g$  data. The sequence for variable adjustments is  $\varphi_t \rightarrow \varphi_b \rightarrow N_d \rightarrow N_t$ . This sequence of variable adjustment was based on their effect on the shape of the gate current in the model and their degree of variability both HFET-to-HFET and pre- and post-irradiation. By setting the energy levels first, the functional variation in the current with either temperature or voltage is established. Geometrically this is manifested by the shape of the calculated curve matching the shape of the data curve. The carrier and trap densities are then adjusted to match the level of the current level throughout the temperature range.

This sequential adjustment of variables proceeds as the Relative-Root Mean Square Error (R-RMSE) is minimized through the optimization algorithm. Figure 29(a) shows the overall optimization sequence while Figure 29(b) provides a process diagram for the optimization algorithm.

The algorithm minimizes the difference between the current data and the calculated  $I_{TAT}$  through the minimization of R-RMSE function. R-RMSE is a measure of the absolute error between the data points and the calculated values at the different voltage and temperature increments. It is calculated as the sum of the squares of the differences between the data and the calculated tunneling currents divided by the mean value of the currents:

$$R - RMSE = \sum_{n=1}^N \frac{(I_{TAT}(T_n) - I_g(T_n))^2}{\left| \frac{(I_{TAT}(T_n) + I_g(T_n))}{2} \right|} + \sum_{n=1}^N \frac{(I_{TAT}(V_{g_n}) - I_g(V_{g_n}))^2}{\left| \frac{(I_{TAT}(V_{g_n}) + I_g(V_{g_n}))}{2} \right|}. \quad (28)$$

The first term in R-RMSE is the difference between the data and calculated values along the I vs. T curve and the second is the difference between the values along the I-V curve.



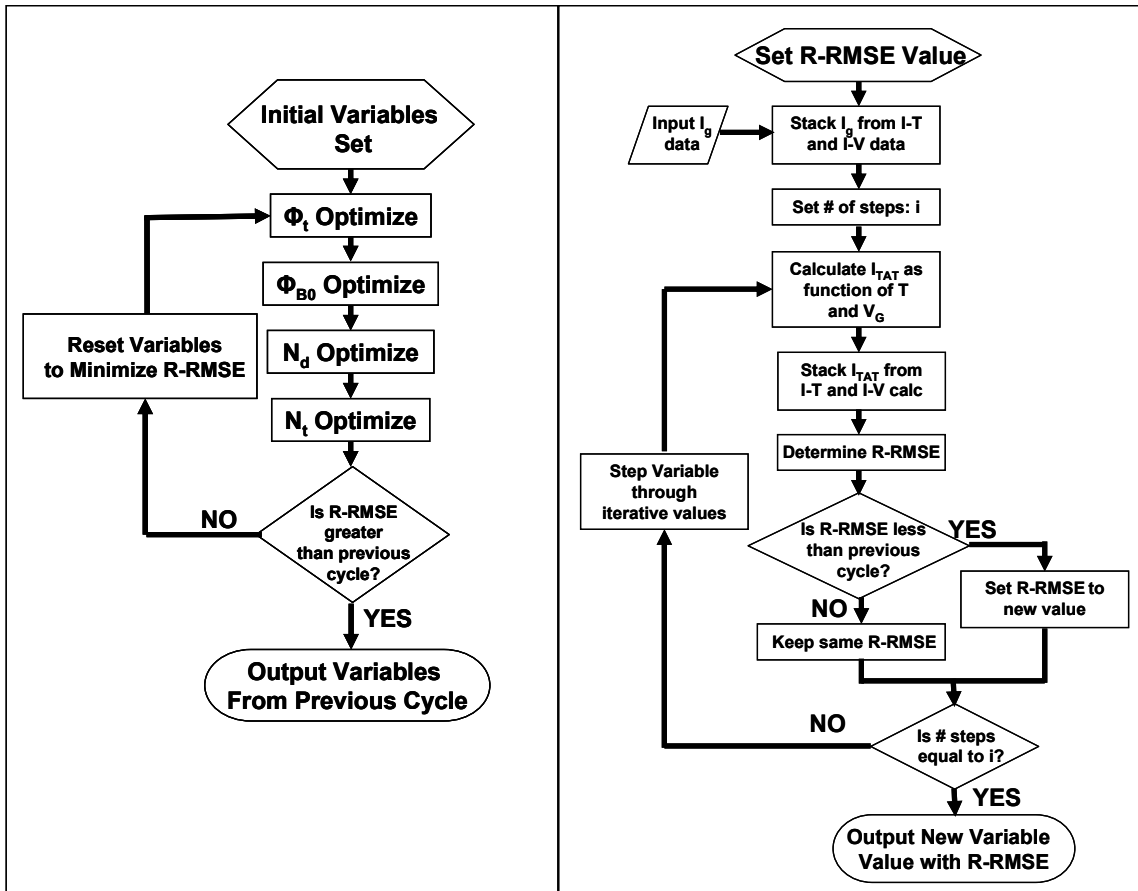


Figure 29. (a). Optimization sequence for application of the TAT model to measured data. (b) Optimization algorithm for minimization of R-RMSE to determine the best value for each variable in the model.

## V. Experimental Results

There are three categories of results presented in this chapter. They are denoted as electron irradiation, first neutron irradiation, and second neutron irradiation results. First are the results of electron irradiation of unpassivated HFETs. These measurements were carried out by Sattler [31] and Jarzen [65]. These results focused on the low temperature ( $\sim 85$  K) transistor current, gate leakage current, and the junction capacitance. Only those results that are relevant to the analysis in Chapter 6 are presented here. The complete results of Sattler's and Jarzen's electron irradiation experiments are available in their theses. [31, 65]

The primary results presented in this chapter are from the two neutron irradiation experiments conducted at the OSURR. The first neutron experiment focused on determining the temperature dependent effect of neutron irradiation on the electrical properties of the HFETs. Four HFETs survived the irradiation and measurement cycling. The transistor current was measured before and after irradiation and at low ( $\sim 80$  K) and high ( $\sim 300$  K) temperatures. These measurements were made to compare the effect of neutron irradiation to the effect of electron irradiation as determined by Sattler and the effect of proton irradiation by other researchers [45, 47-52, 55, 56]. The gate leakage currents were measured before and after irradiation and throughout the temperature range of 80 to 300 K. The measurement of the gate current as a function of temperature at multiple gate voltages was made to enable comparison with the results of Gray [66]. His measurements were made with similar HFETs under similar conditions. Measurement of the same currents after one week and three week RT annealing under zero bias sought to determine the long-term effect on device characteristics after irradiation. Also,

temperature dependent measurement of junction capacitance vs. voltage after irradiation and a room temperature anneal was made for comparison to the results of Jarzen.

The second set of neutron irradiation measurements was designed to extend and amplify the results from the first neutron experiment. A total of twelve HFETs were irradiated and measured to demonstrate the repeatability of the results. Six of the HFETs were passivated with SiN and six were unpassivated. The measurements of temperature dependent transistor current and gate leakage current were repeated. The transistor currents were measured at multiple temperatures through the 80 to 300 K range, instead of measurement only at the extremes, in order to determine the temperature dependent response throughout the range. Measurements of the temperature dependent junction capacitance and gate conductance as a function of voltage were made in order to help determine the source of the changes to the currents. More complete measurements of the gate leakage current as a function of both voltage and temperature were taken to support the comparison of experimental results with the trap-assisted tunneling model of Saithaya [60].

This last set of results is focused on the source of the increase in gate leakage current after irradiation. The trap-assisted tunneling model was applied to the HFETs and the voltage and temperature-dependent gate leakage were determined. The results were compared to the pre- and post-irradiation experimental data taken from the second set of neutron irradiations. Changes to the current are explained via the model in terms of the change in the input parameters in Section 5.3 and Chapter 6. The results of the application of the model to the experimental data helps to explicate the observed changes

in the gate leakage current in terms of irradiation induced defects in the HFET AlGaIn layer.

## **5.1 Electron Irradiation Results**

The irradiation produced similar changes to the I-V and C-V characteristics for all devices measured. Figure 30 presents the pre- and post-irradiation transistor curves and  $I_{gs}$ -V measurements for device A08. Figures 31 and 32 provide the same results with additional measurement and irradiation cycles for device A09. Figure 33 presents the pre- and post-irradiation C-V results for device A01. Variations in results for different HFETs are discussed as necessary.

All irradiations were conducted at  $85 \pm 2$  K in order to reduce defect migration and annealing during irradiation. The C-V and I-V measurements were conducted immediately following irradiation while the devices were still maintained below 85 K to again minimize the effect of annealing on any radiation induced displacements or trapped charge.

Figure 30 provides the results of the  $I_{ds}$ - $V_{ds}$  and  $I_{gs}$ - $V_{ds}$  measurements after an initial exposure to a fluence of  $10^{14}$  e $^-$ /cm $^2$  at  $\sim 85$  K. The gate current increase in Figure 30(b) is also visible in the post-irradiation  $V_{gs} = -1$  V curve in Figure 30(a), resulting in an increased slope in the drain current with increased gate voltage after reaching saturation. The  $I_{ds}$  with the gate leakage current removed is also displayed for  $V_{gs} = -1, -2,$  and  $-3$  V. Following the subtraction of  $I_{gs}$ , the curves still show a 20% increase in  $I_{ds}$  in the saturation region at  $V_{gs} = -1$  V following irradiation. There is also a one order of magnitude increase in  $I_{gs}$  at  $V_{gs} = -3$  V and  $V_{ds} = 0$  after irradiation.

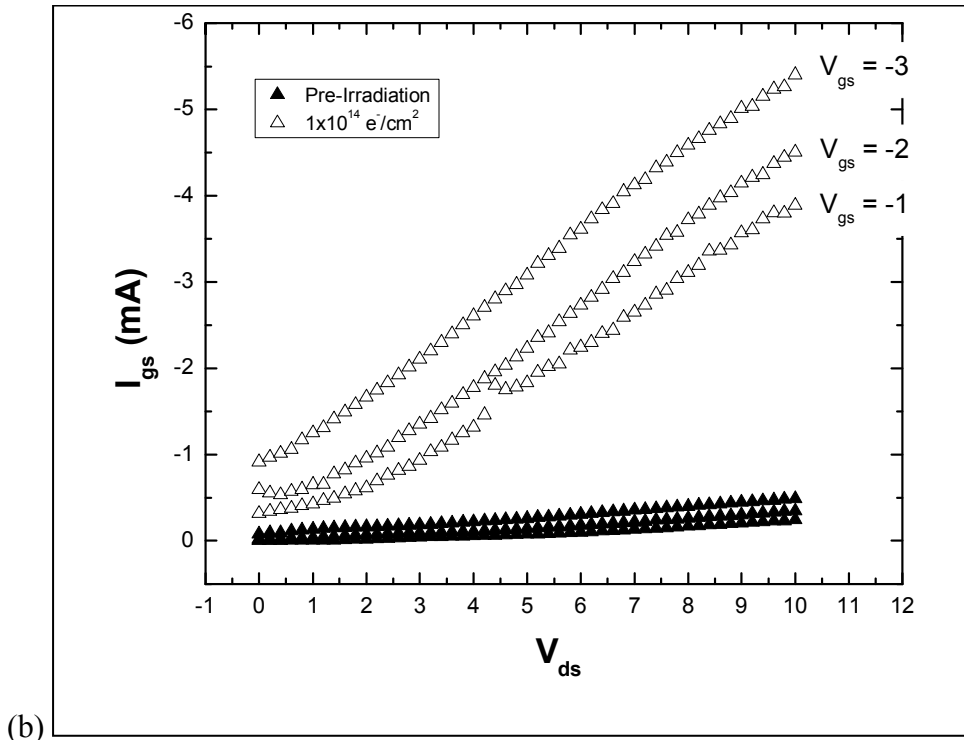
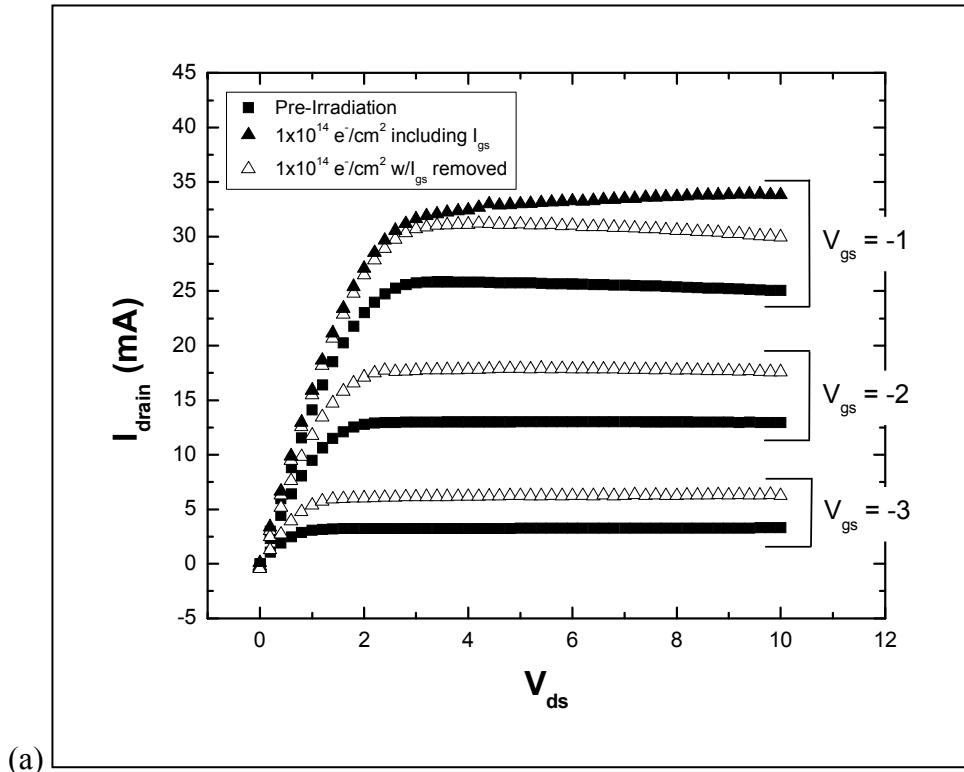
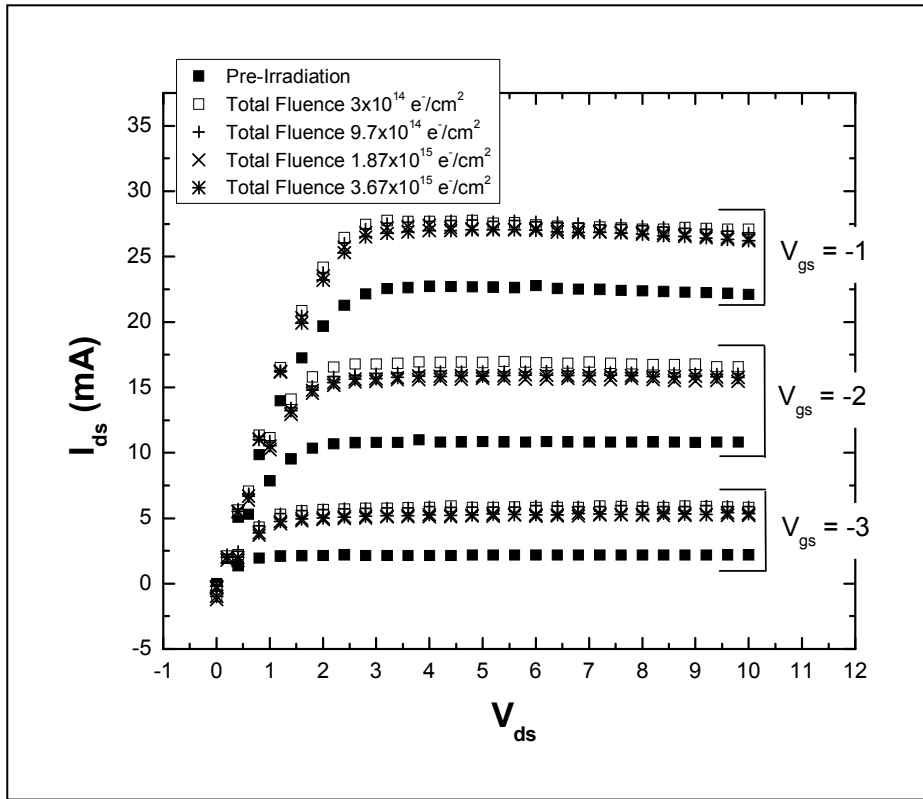


Figure 30. The pre- and post-irradiation measurements of sample A08 showing the increase in both  $I_{\text{drain}}$  (a) and  $I_{\text{gs}}$  (b) following irradiation. The curve for  $V_{\text{gs}} = -1\text{V}$  is shown with and without  $I_{\text{gs}}$ . The irradiation and measurements were performed at liquid nitrogen temperatures ( $\sim 85\text{ K}$ ).

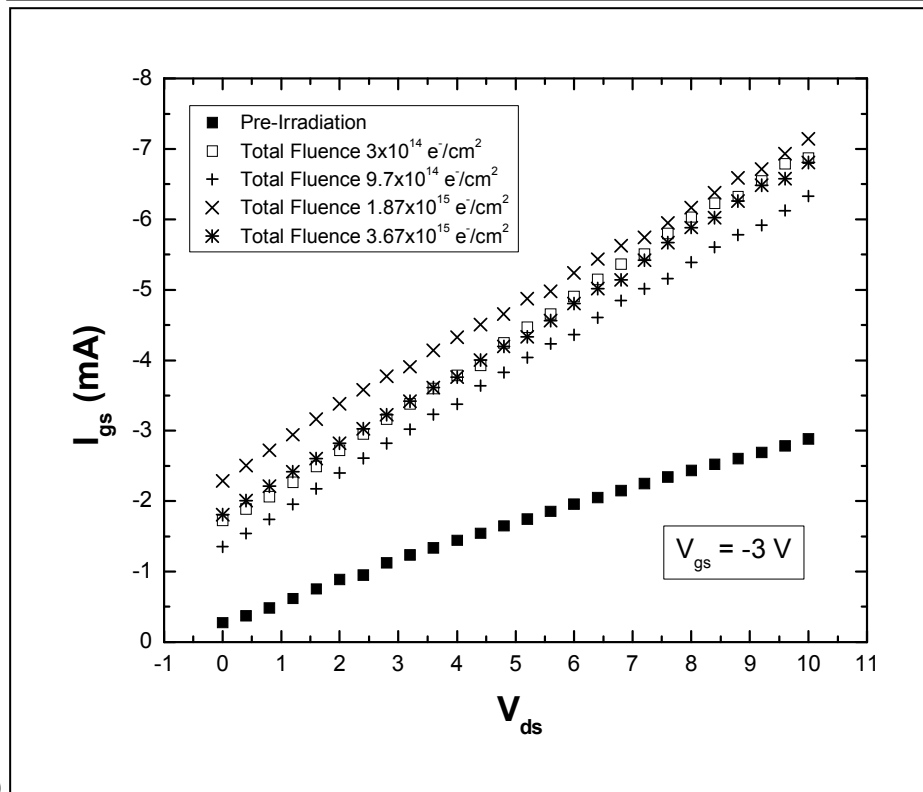
Figure 31 presents the pre- and post-irradiation transistor curves and  $I_{ds}$ - $V_{ds}$  and  $I_{gs}$ - $V_{ds}$  measurements for HFET A09 following several irradiation and measurement cycles. The  $I_{ds}$  curves are displayed with  $I_{gs}$  subtracted. Figure 31(a) clearly shows that  $I_{ds}$  saturates following the initial radiation, while in Figure 31(b) the gate current recovers slightly following the initial irradiation.

Following an in-situ anneal from 85 K to room temperature (RT) over 21 minutes,  $I_{ds}$  and  $I_{gs}$  were again measured at RT.  $I_{ds}$  returned to its pre-irradiation values while the increase in  $I_{gs}$  is persistent at RT. Figure 32 shows  $I_{ds}$  and  $I_{gs}$  measured at RT pre- and post-irradiation for A09.

Figure 33 presents the pre- and post-irradiation high frequency (1 MHz) capacitance measurements at 85 K on sample A01. The figure has two interesting post-irradiation features. First, the heterojunction capacitance increases in the inversion region of the curve as well as in the accumulation region following electron exposure. Second the curve shifts more negative, meaning that a threshold voltage shift of -0.5 V has occurred.



(a)



(b)

Figure 31. The pre- and post-irradiation measurements of sample A09 following several measurement and irradiation cycles. The irradiation and measurements were performed at  $\sim 80$  K.  $I_{gs}$  was subtracted from all curves in Figure 31(a).

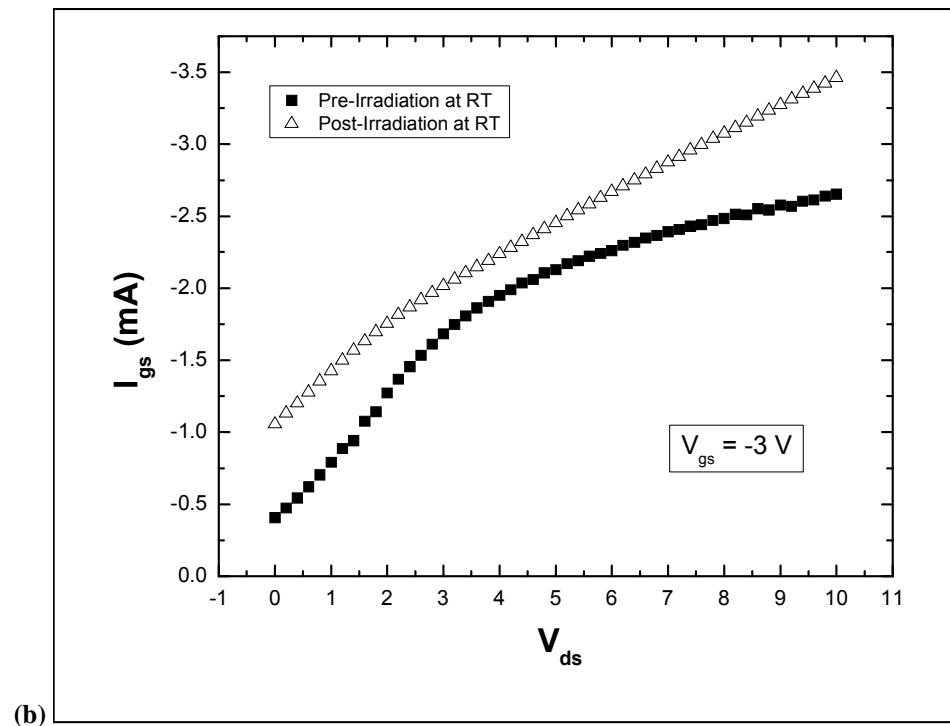
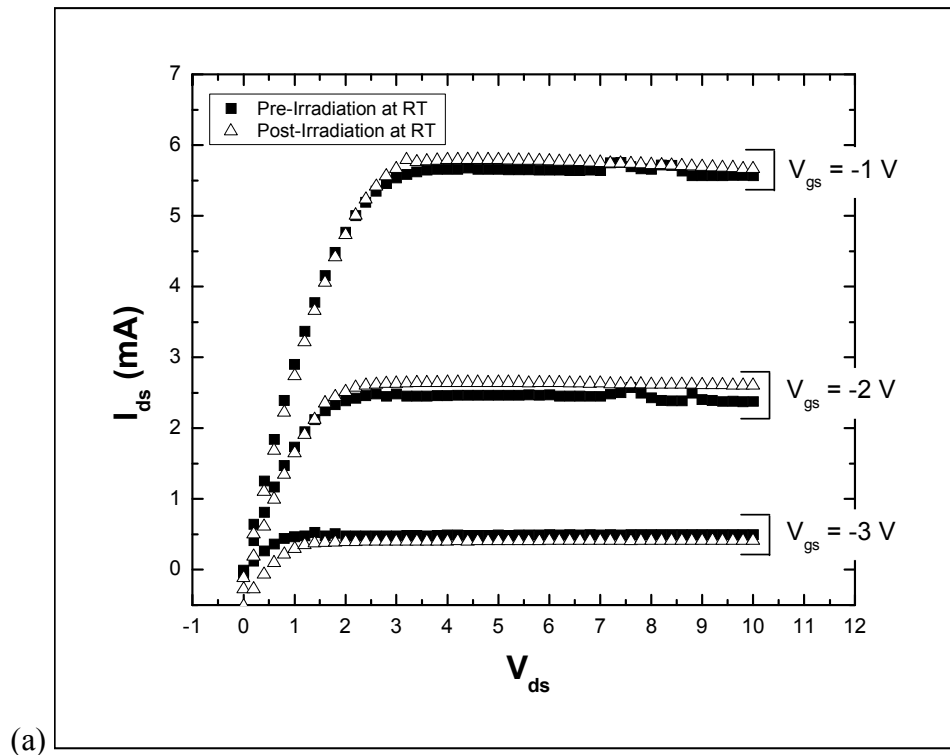


Figure 32. The pre- and post-irradiation measurements of sample A09 at RT following several measurement and irradiation cycles. The irradiations were performed at  $\sim 85$  K.  $I_{gs}$  was subtracted from all curves in Figure 32(a).  $I_{ds}$  has returned to its pre-irradiation value.

Figure 32(b) shows a persistent increase following irradiation and warming to RT.



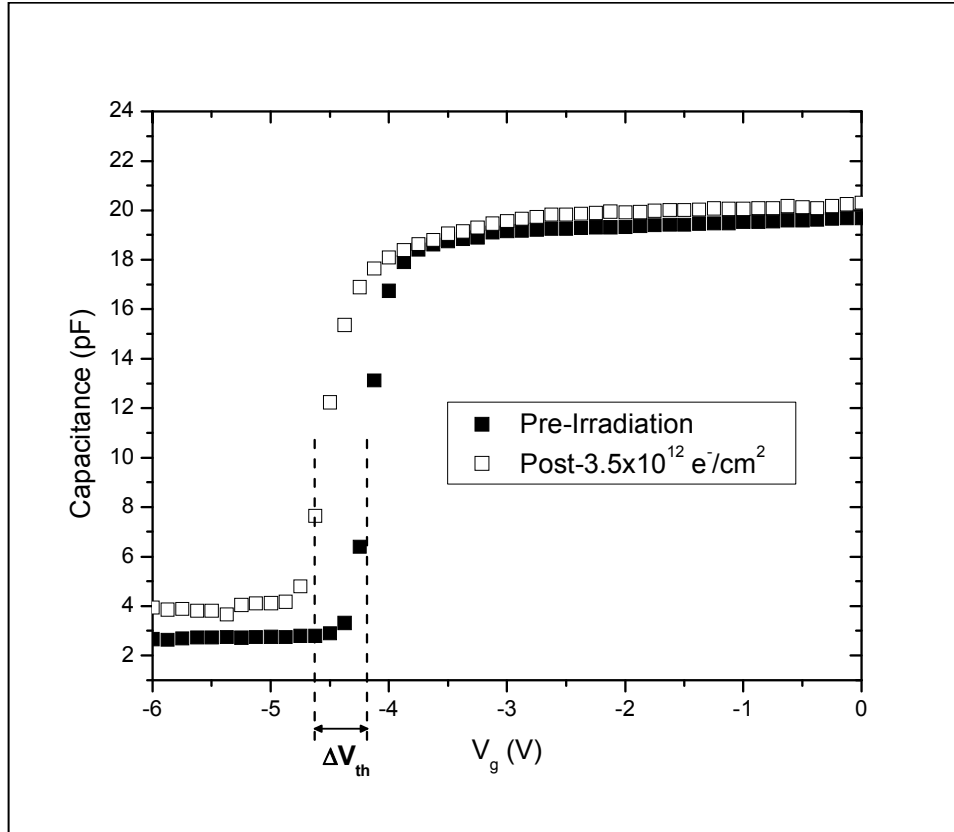


Figure 33. Pre- and post-irradiation capacitance-voltage measurements of HFET A01 recorded at  $\sim 80$  K following exposure to a fluence of  $3.5 \times 10^{12} \text{ e}^-/\text{cm}^2$  with 0.45 MeV electrons.

## 5.2 Neutron Irradiation Results

### Pre-Irradiation Measurements

The results of pre-irradiation measurements of the gate leakage current vs. temperature at three voltages in the electron irradiation results demonstrate the generally linear increase in current with temperature. The purpose of the multiple gate voltage setting for the temperature sweeps from 82 to 294 K in the neutron irradiation measurements is the application of the data to the trap-assisted tunneling model. The maximum gate voltage of -4 V was selected in order to maximize the gate leakage current but to keep the HFETs above the threshold voltage. All HFETs tested had threshold gate

voltages between -4 and -5 V. Figure 34 shows a typical HFET's pre-irradiation  $I_{gs}$ -T curves.

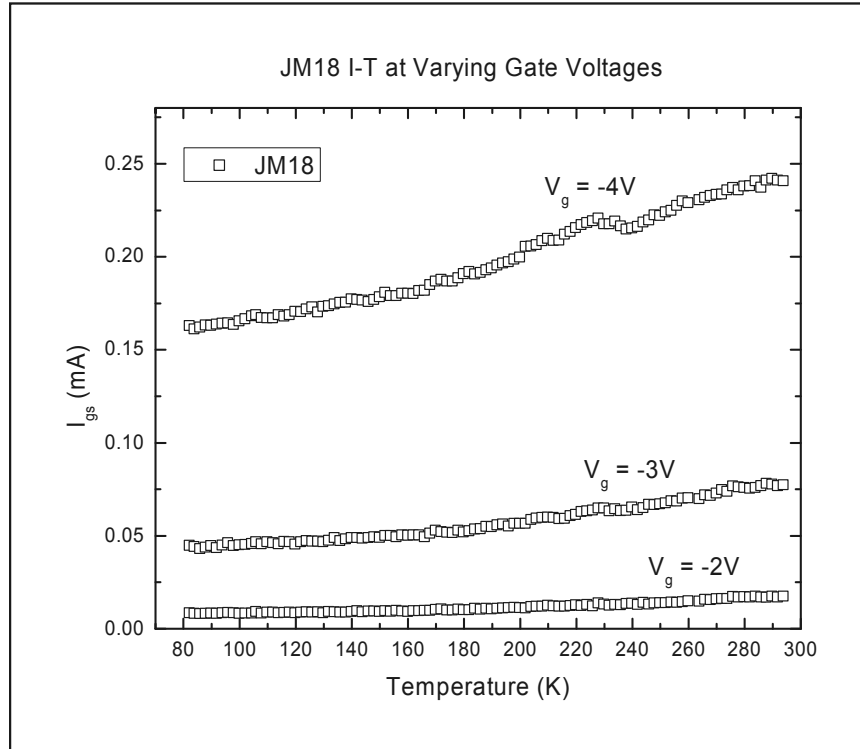


Figure 34. Pre-irradiation I-T curves at three gate voltages over the temperature range of 82-294K for HFET JM18.

The pre-irradiation  $I_{gs}$ -T curves at a gate voltage of -4 V for each the passivated and unpassivated HFETs used in the second neutron experiment are shown in Figure 35. Each of the curves illustrates a generally a linear increase in current with temperature with only small variations. The normal device-to-device variation is also demonstrated. The average pre-irradiation I-T curves of the six passivated and six unpassivated HFETs are shown in Figure 36. The average leakage current in the passivated HFETs is nearly double that of the unpassivated HFETs, specifically an average increase of ~80% throughout the temperature range. The reason for the difference is discussed in Chapter 2 and the effect on post-irradiation results in Chapter 6.

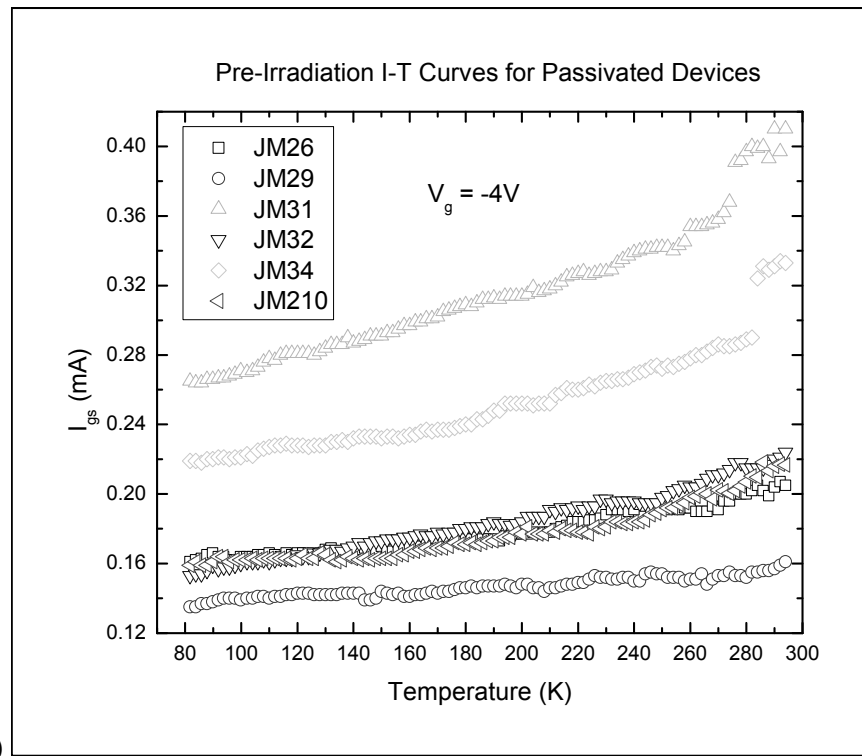
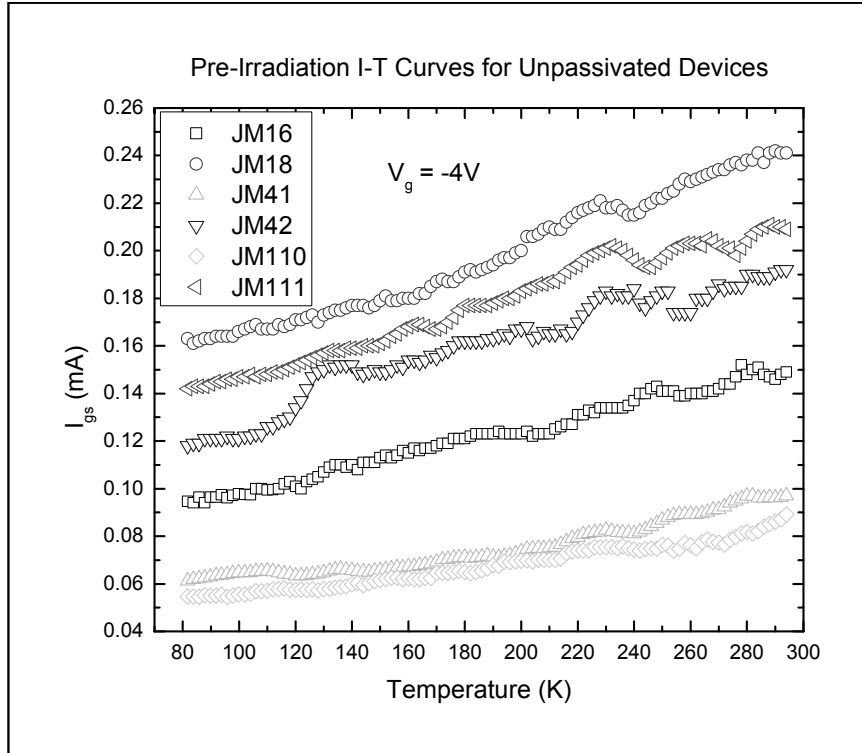


Figure 35. Pre-irradiation I-T curves for unpassivated (a) and passivated (b) HFETs at a gate voltage of -4V.

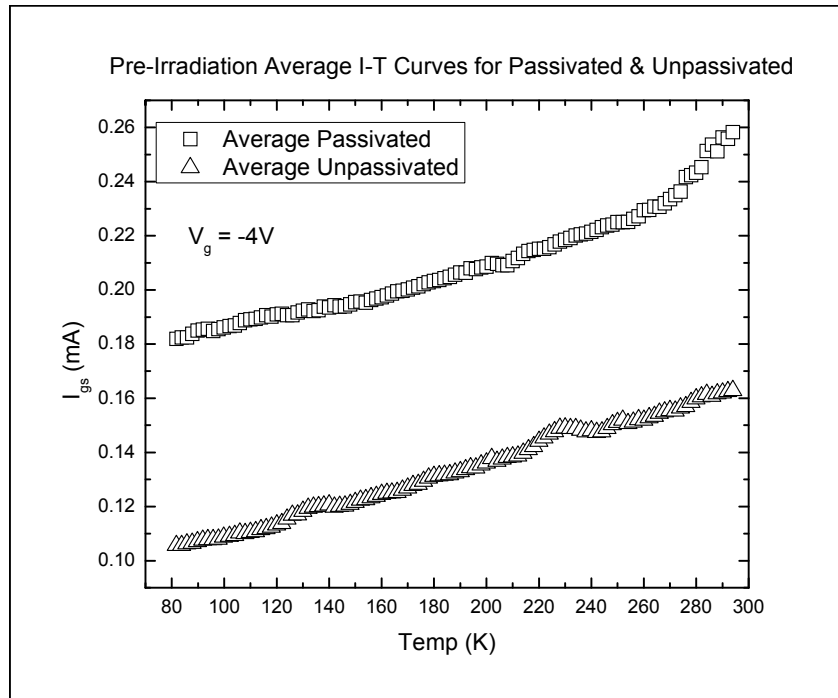


Figure 36. Average pre-irradiation I-T curves for unpassivated and passivated HFETs at a gate voltage of -4V showing the 80% increase in gate current with passivation.

In order to determine the reliability of the changes observed in the gate leakage current after irradiation as well as the reliability of the trap-assisted tunneling model in matching the experimental data, a measure of the uncertainty in the gate leakage current was developed. There are systemic errors in the current and temperature measurements and random errors introduced in the system due to the temperature cycling. Cooling and heating of the HFETs has an effect not only on mobile charges in the AlGaIn layer but also on the contacts. The ohmic contacts are particularly susceptible to cracking and breaking due to thermal cycling. Changes to the contacts are most severe during the first cooling and heating cycle. All HFETs were first cooled and heated at least once before the initial gate voltage vs. temperature measurement to prevent these changes from skewing the pre-irradiation data.

An HFET was repeatedly heated and cooled with gate current measurements recorded throughout the temperature to determine the error introduced by repeated heating and cooling cycles. Figure 37 shows the results of this test. There is a noticeable shift in the gate leakage current after the first temperature sweep from 82 to 294 K. The gate current in three additional sweeps of 294 to 82 K and 82 to 294 K were measured. The standard deviation was calculated based on these six current measurements at intervals of 2 K. Figure 38 shows the resulting average current for the six sweeps with error bars of one standard deviation. As is apparent from Figure 37, the sweep-to-sweep variation is minimized after the first cooling and heating cycle. Also from Figure 37, the spread becomes greater as the sweep approaches room temperature as the mobile charge becomes free to move in the AlGa<sub>N</sub> layer.

Pre-irradiation gate current vs. gate voltage measurements are shown in Figures 39 and 40 for an unpassivated and passivated HFET respectively at five temperatures ranging from 80 to 300 K. The measurements are as expected with an exponential increase with increased reverse bias on the gate and an increase with temperature throughout the temperature range. Every HFET irradiated had these measurements taken in order to support comparison with the TAT model.

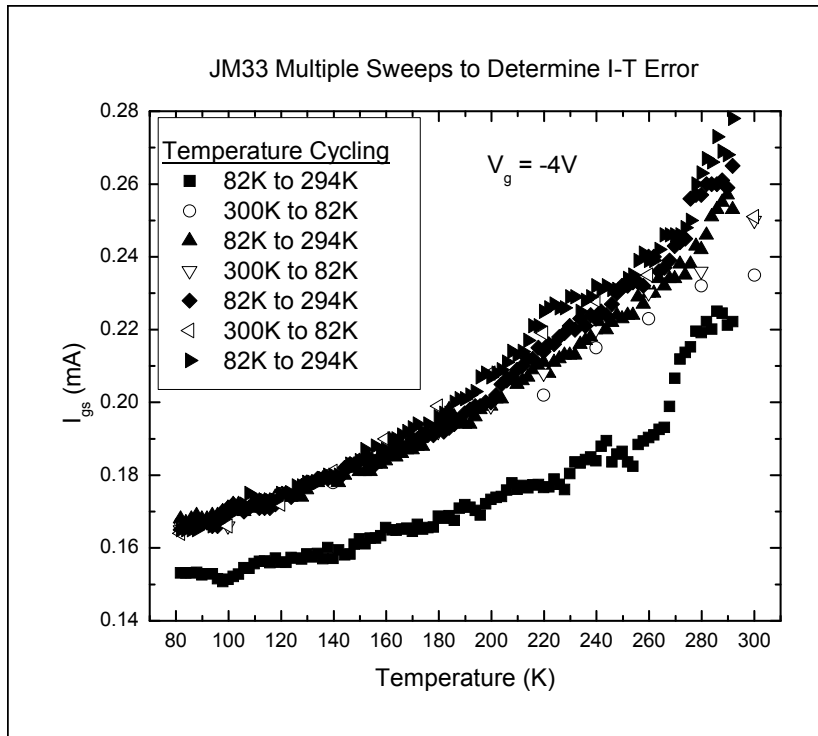


Figure 37. Multiple gate voltage vs. temperature sweeps of an HFET to determine the variation with repeated cooling and heating. The cycles in the legend are listed in chronological order.

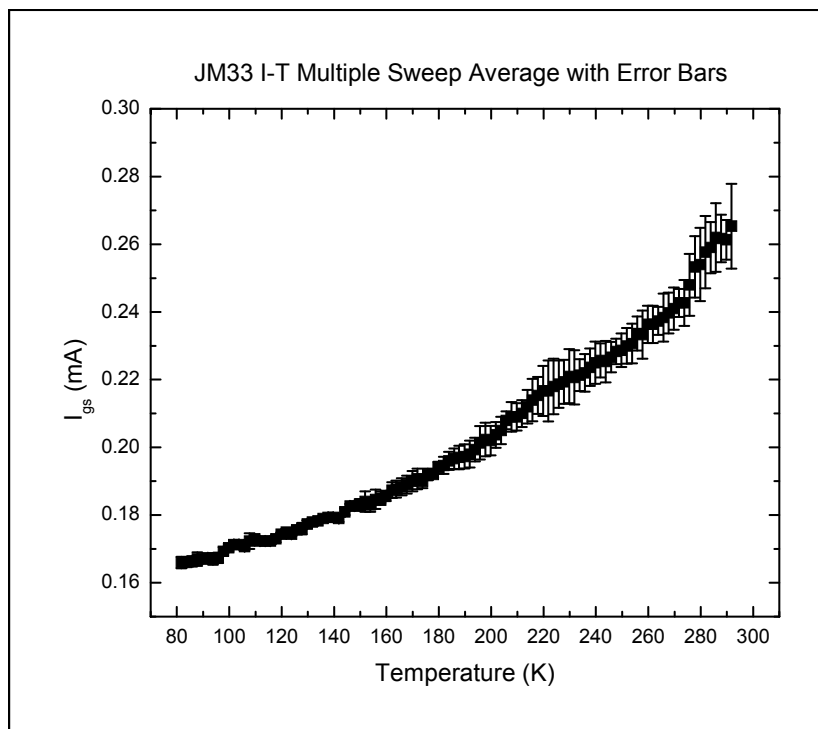


Figure 38. Average of the gate voltage versus temperature sweeps in Figure 37, not including the first sweep, with error bars of one standard deviation in the data.

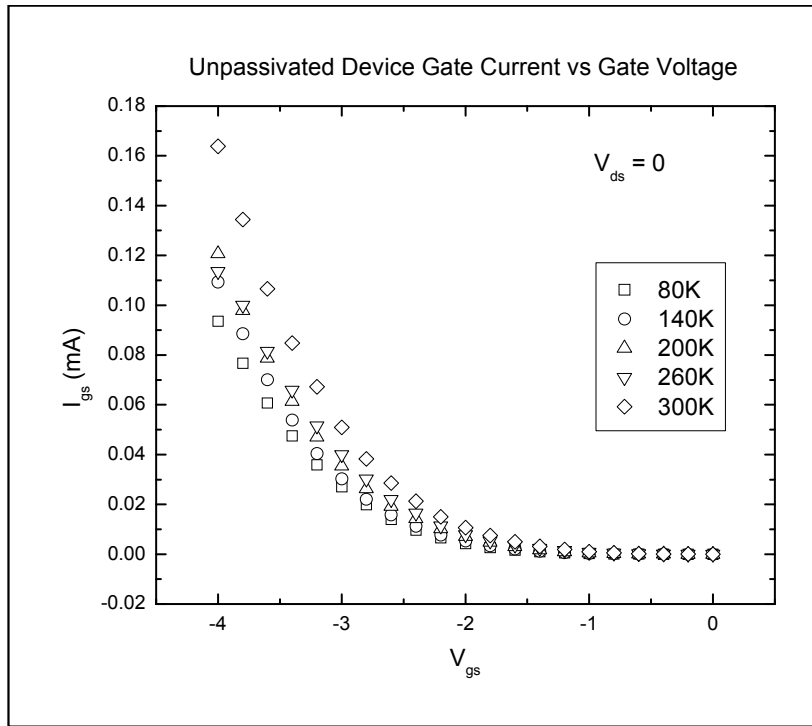


Figure 39. Gate current versus gate voltage at five different temperatures for an unpassivated HFET.

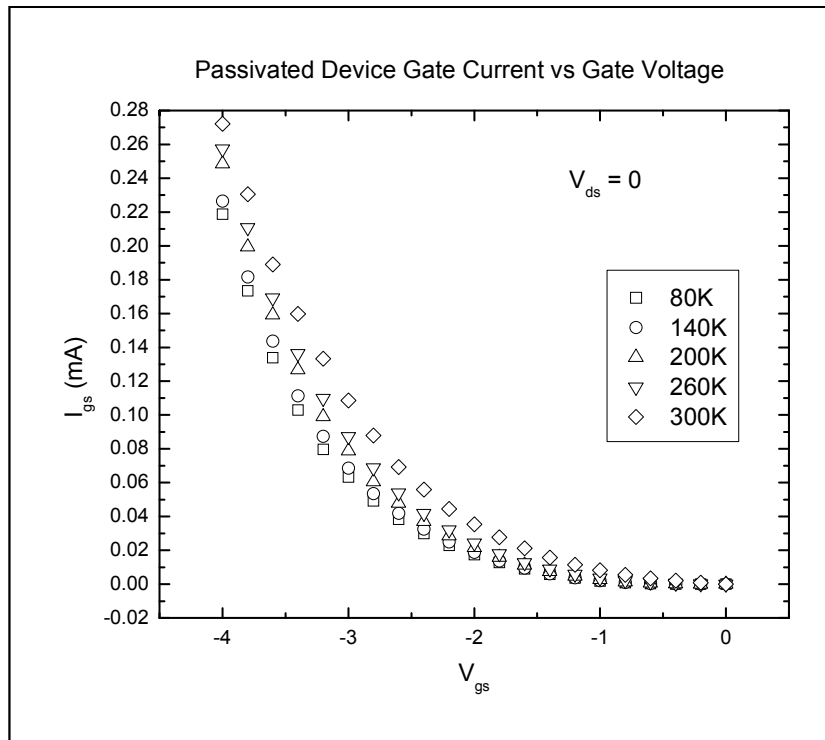


Figure 40. Gate current versus gate voltage at five different temperatures for a passivated HFET.

Pre-irradiation drain-to-source current vs. drain-to-source voltage or transistor current measurements were recorded at gate voltages of -2, -3, and -4 V and at temperatures of 80, 140, 200, 260, and 300 K. Figures 41 and 42 show typical results for unpassivated and passivated HFETs for temperatures of 80 and 300 K. The increase in transistor current with passivation due to increased  $n_s$  as well as the increase with decreased temperature due to decreased channel  $\mu$  is expected. Also, the linearity in the transistor current of the HFETs in the saturation region after the initial rise in the linear region is indicative of well behaving HFETs.

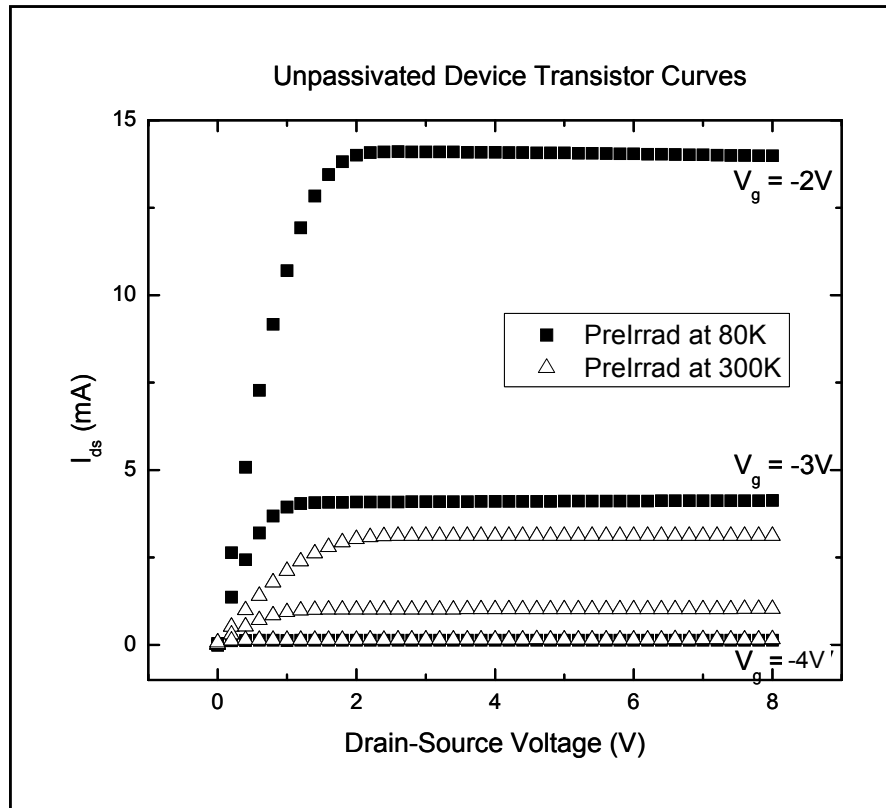


Figure 41. Drain-to-source current versus drain-to-source voltage at three different gate voltages and temperatures of 80 and 300 K for a unpassivated HFET.



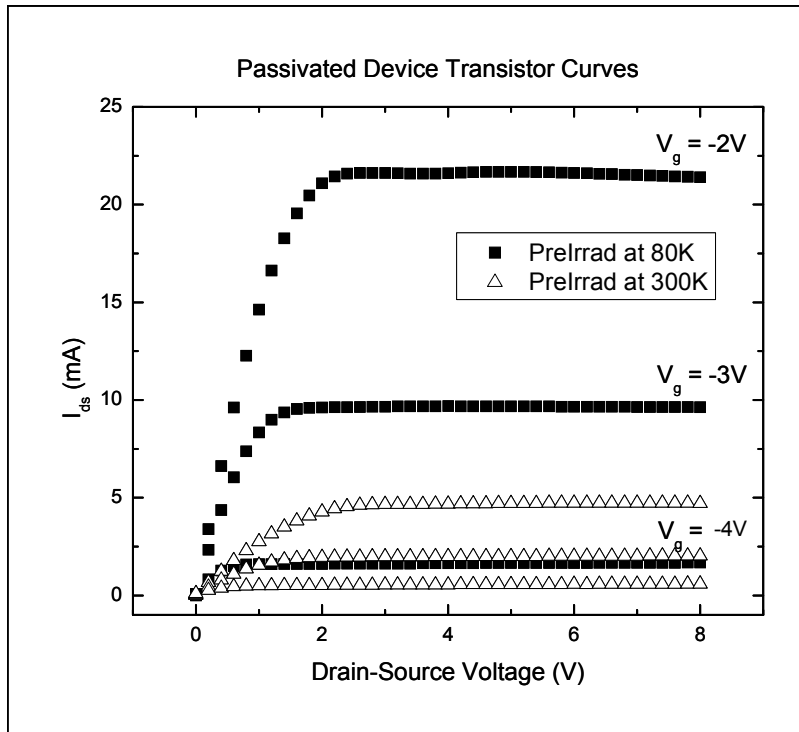


Figure 42. Drain-to-source current versus drain-to-source voltage at three different gate voltages and temperatures of 80 and 300 K for a passivated HFET.

Pre-irradiation gate capacitance vs. gate voltage measurements were recorded at gate voltages of -6 to 0 V and at temperatures of 80, 140, 200, 260, and 300 K with drain-to-source voltages of 0 V. Figure 43 shows typical results for unpassivated and passivated HFETs for temperatures of 80 and 300 K. The increased threshold voltage in the passivated HFETs is apparent with an average shift of -0.6 V from an unpassivated average of -4.2 V to a passivated average of -4.8 V since more positive charge on the passivated AlGaIn surface requires more negative gate voltage to reach threshold. The presence of more interface traps at higher temperature is evident in the reshaping of the curves at 80 K versus 300 K without an accompanying shift in the threshold voltage [92].

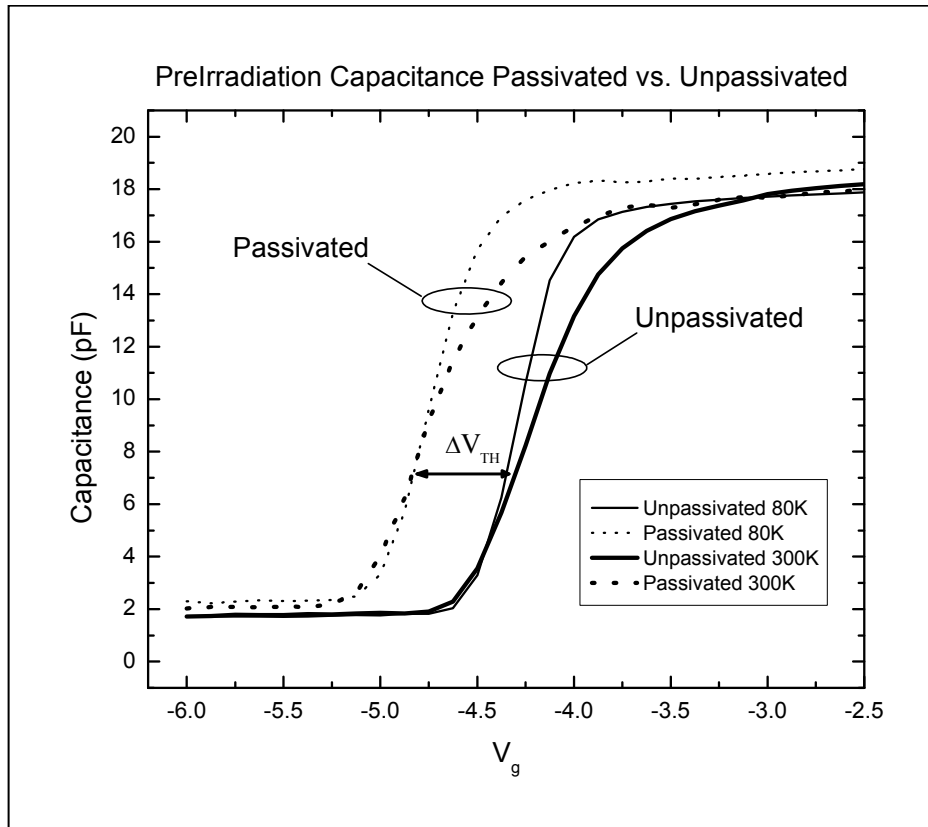


Figure 43. Capacitance versus gate voltage at temperatures of 80 and 300 K for passivated and unpassivated HFETs.

## First Neutron Irradiation Experiment

All irradiations produced similar results regardless of total exposure. Figures 45-51 present the results for one device from Set #2 (JM22) which is representative of the four irradiated devices. Device variations are discussed as necessary.

All irradiations were conducted at  $84 \pm 2$  K in order to reduce defect migration and annealing during irradiation. Electrical measurements conducted immediately following irradiation, while the HFETs were maintained below 85 K, were used to observe the effect of displacement damage on  $I_{gs}$  and  $I_{ds}$ . Electrical measurements performed at 80 K and at RT following the RT anneal provided insight into the stability of the displacement effects and the annealing mechanisms involved after irradiation.

Figure 44 presents the temperature profile, irradiations, and measurements performed on the HFETs in this experiment.

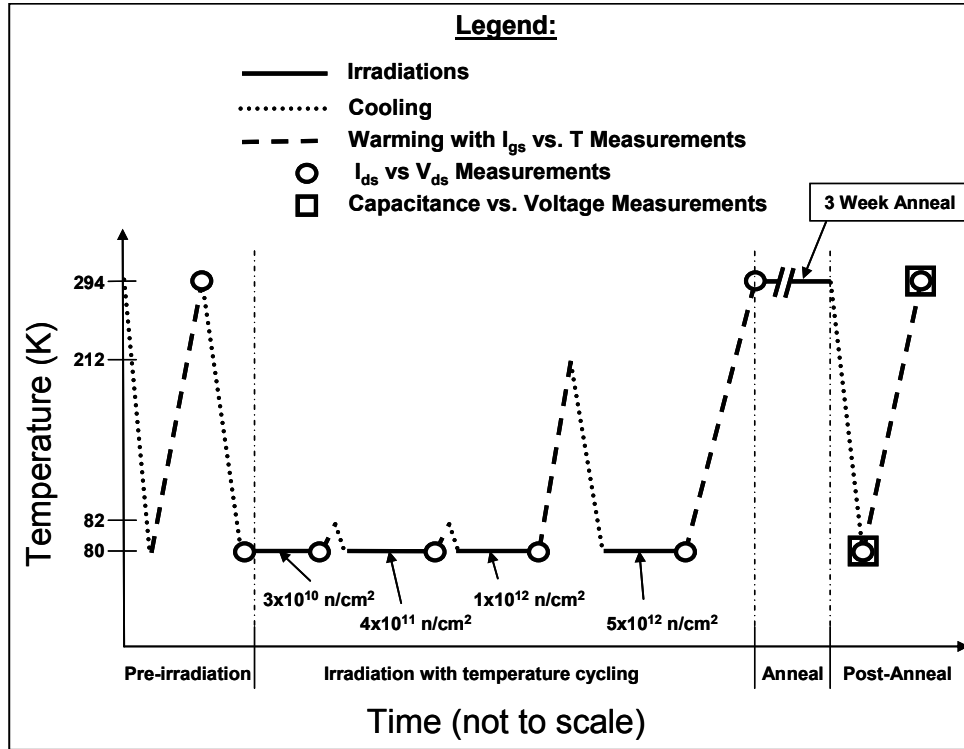


Figure 44. Experimental procedure of the first neutron irradiation experiment showing irradiations, measurements, and temperature profile.

Figure 45 presents the pre- and post-irradiation  $I_{gs}$  as a function of temperature. In this experiment, measurements were made from 82-294 K pre-irradiation, 82-84 K after exposure to  $3 \times 10^{10}$  n/cm<sup>2</sup> and a second exposure to  $4 \times 10^{11}$  n/cm<sup>2</sup>, 82-212 K after exposure to an additional  $10^{12}$  n/cm<sup>2</sup>, and 82-294 K after a final exposure to  $5 \times 10^{12}$  n/cm<sup>2</sup>. The initial increase in gate current reaches a maximum after exposure to  $3 \times 10^{10}$  n/cm<sup>2</sup> and did not change after subsequent irradiations. This increase of 13% (0.03 mA at 82 K) is constant to 244 K and then changes to 20% at RT.

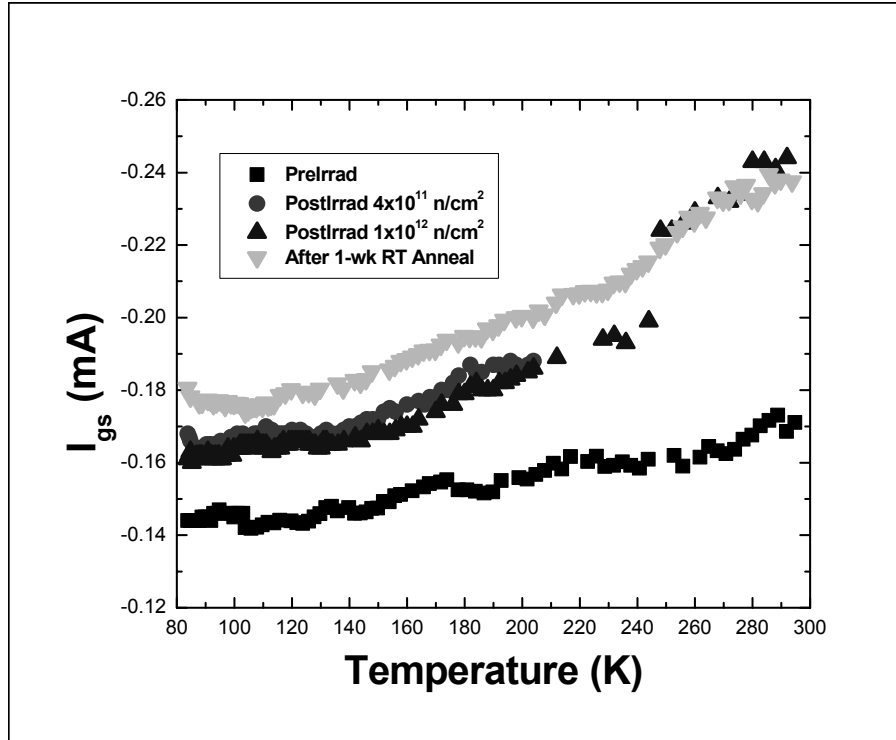


Figure 45. Temperature dependent  $I_{gs}$  before and after neutron irradiation

Figure 46 presents the pre- and post-irradiation  $I_{ds}$  at 80 K.  $I_{ds}$  increases 16% (+3.4 mA in the saturation region) after a  $3 \times 10^{10} \text{ n/cm}^2$  exposure. As with  $I_{gs}$ , it does not increase after subsequent exposures. The figure shows the results for one HFET which was typical for the four HFETs measured.

Figure 47 presents the pre- and post-irradiation  $I_{ds}$  at 294 K. The post-irradiation measurements are taken only after the final irradiation in order to reduce the effects of annealing on the 80 K measurements. Following irradiation the current in the saturation region decreased 31% (-2.4 mA) for  $V_{gs} = -2 \text{ V}$ . The decrease in the saturation region current of the other three HFETs was -34%, -35%, and -32% regardless of the total exposure. This temperature-dependent behavior, increased  $I_{ds}$  at low temperature and decreased  $I_{ds}$  at room temperature, was further explored after RT annealing.

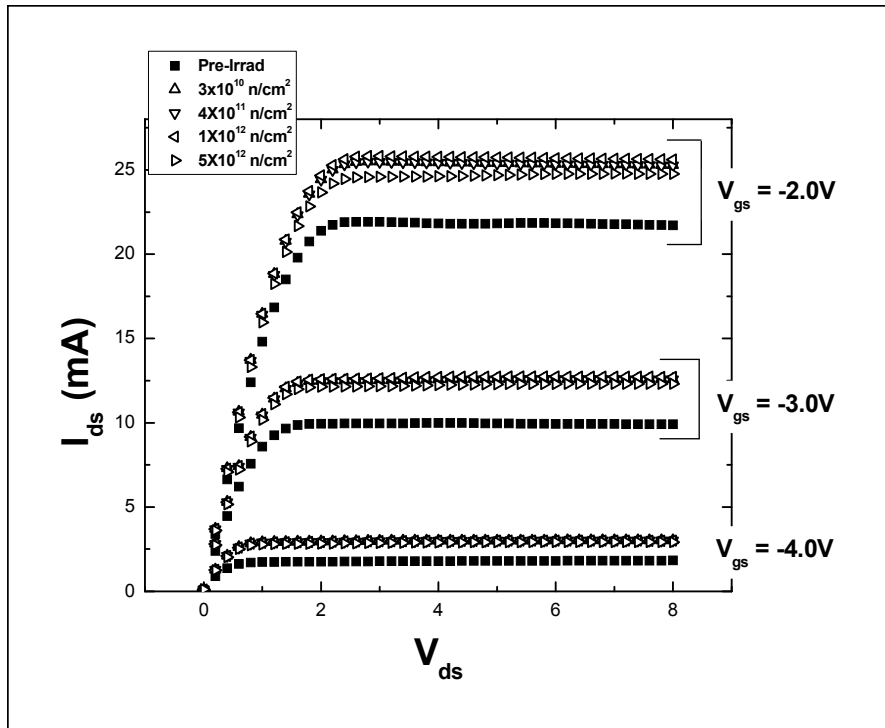


Figure 46. HFET transistor curves measured at 80 K before and after neutron irradiation at 84 K.

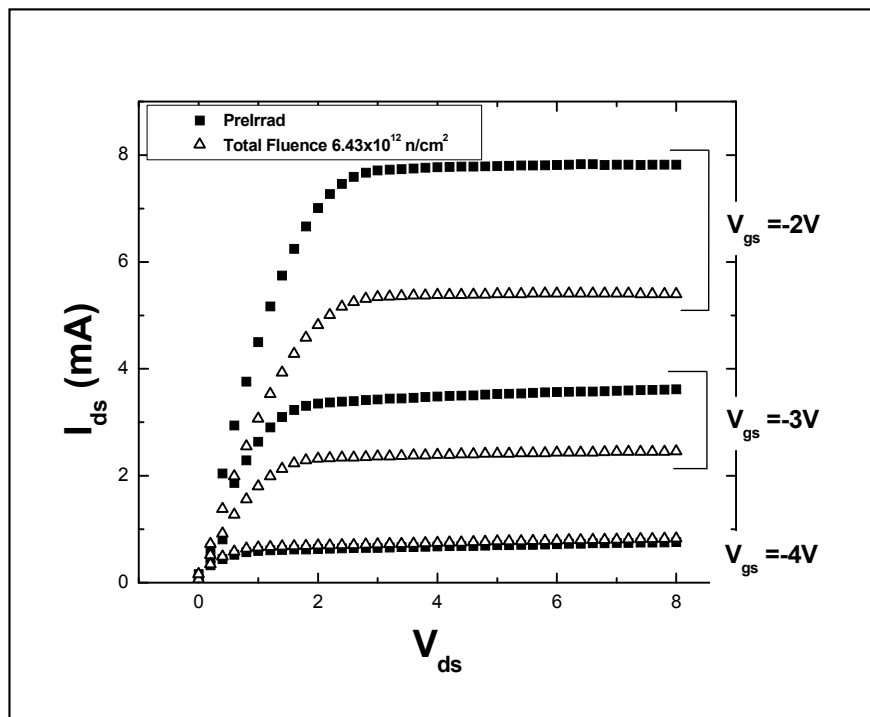


Figure 47. HFET transistor curves measured at 294 K before and after neutron irradiation at 84 K.

Figure 48 presents  $I_{gs}$  as a function of temperature after a one-week RT anneal. The current did not return to its pre-irradiation value. Instead it increased by  $\sim 0.02$  mA from the post-irradiation values across the entire temperature range. The post-anneal data closely matches the measurement immediately after irradiation above 240 K indicating that stable defects had formed during annealing with an activation temperature of  $\sim 240$  K.

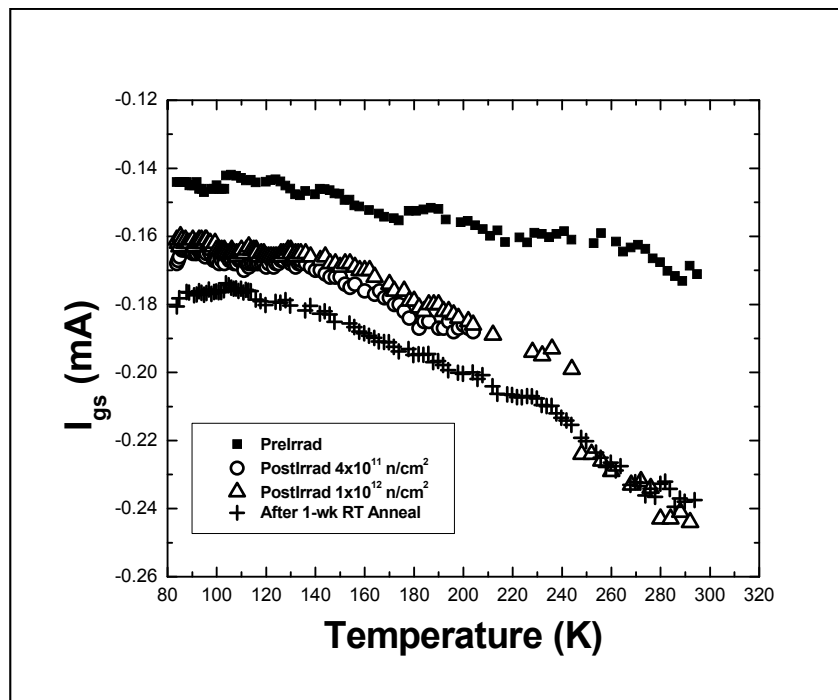


Figure 48. Temperature-dependent  $I_{gs}$  before and after neutron irradiation and after a one-week room-temperature anneal.

Figure 49 presents  $I_{ds}$  at low temperature ( $\sim 80$  K) following a three-week RT anneal. The current in the saturation region has fully recovered to its pre-irradiation value. This effect is consistent for all four HFETs.

Figure 50 presents  $I_{ds}$  at RT ( $\sim 294$  K) after a 3-week RT anneal. The current in the saturation region has not recovered to its pre-irradiation value. Instead, the saturation

current decreases by an additional 0.60 mA at -2 V<sub>gs</sub> and -6 V<sub>ds</sub>. This behavior was consistent for all HFETs investigated and an explanation is offered in Chapter 6.

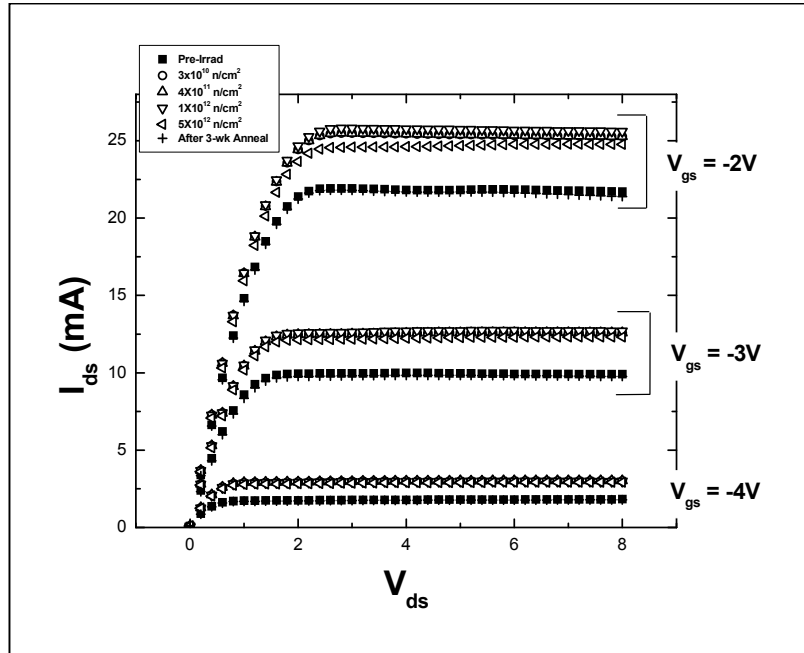


Figure 49. HFET transistor curves measured at 80 K before and after neutron irradiation at 84 K and after a three-week room-temperature anneal.

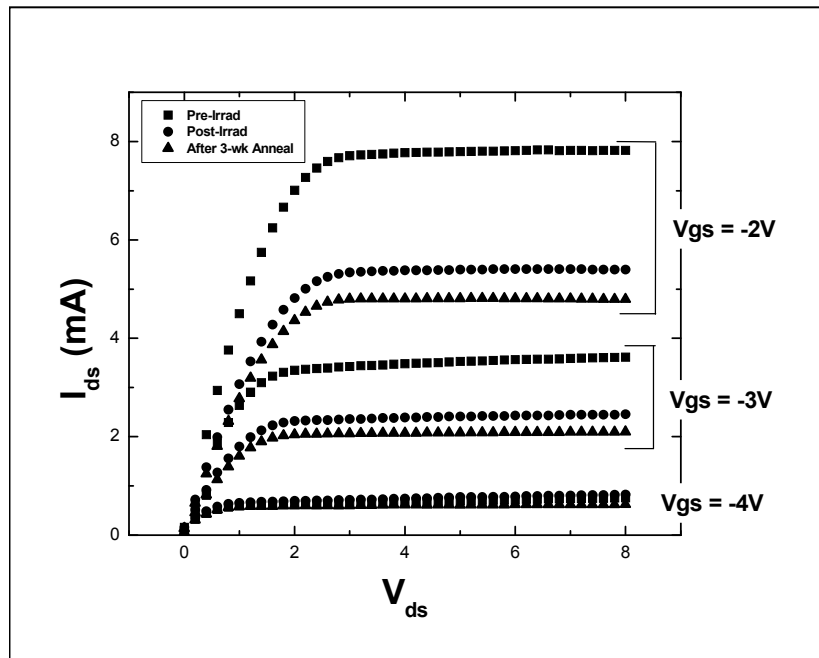


Figure 50. HFET transistor curves measured at 294 K before and after neutron irradiation at 84 K and after a three-week room-temperature anneal.

Figure 51 presents the high frequency (1 MHz) C-V measurements at 80 K and RT after a three-week RT anneal. There is no evidence of a threshold voltage shift between the two temperature-dependent curves after annealing that would lead to the 2.0 mA drain current shift at 300 K. In Figure 51 there is evidence of donor-like interface traps in the upper half of the bandgap [92] in the RT C-V curve. This may be responsible for the temperature dependent differences in  $I_{ds}$  after annealing as discussed in Chapter 6. In the second neutron irradiation experiment pre- and post-irradiation temperature-dependent C-V measurements were taken to better determine the evolution of charged defects through the irradiation-annealing cycle.

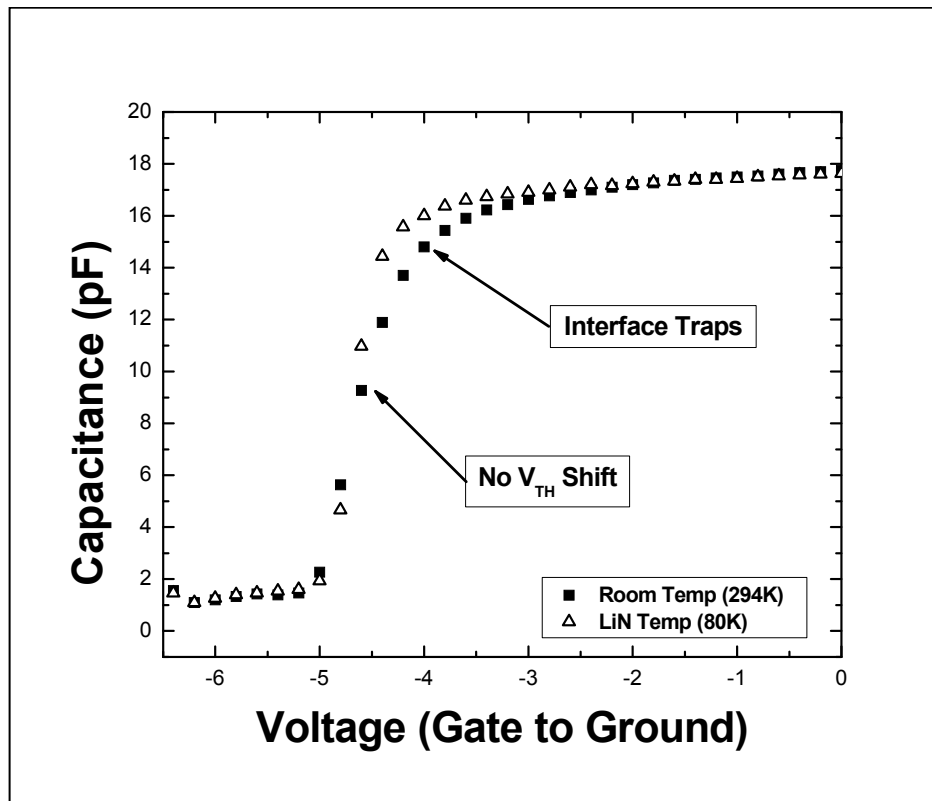


Figure 51. C-V measurements at high frequency (1 MHz) at room-temperature and 80K, following irradiation at 84 K, and a 3-week room-temperature anneal.



## Second Neutron Irradiation Experiment

There were more variations in the results from the second neutron experiment. Twelve HFETs were irradiated and measured with a combination of passivated and unpassivated HFETs. The range of irradiation was greater with total 1 MeV(eq) neutron fluences ranging from  $10^9$  n/cm<sup>2</sup> to  $10^{13}$  n/cm<sup>2</sup>. More measurements were made with multiple C-V and gate conductance vs. gate voltage sweeps at different temperatures. Figures 53-66 present results for typical HFETs representing both the passivated and unpassivated sets.

Additional HFETs were irradiated in order to determine the repeatability of the results observed in the first neutron experiment. A combination of unpassivated and passivated HFETs was irradiated in order to determine the effect SiN passivation has on HFET radiation response. The range of fluences was also greater in this experiment. The lower fluence irradiations were used to determine if there is a minimum damage threshold. The higher fluence level was used to determine if higher fluences would cause device failure. The capacitance and gate conductance measurements were used to determine the temperature and radiation dependent changes to the threshold voltage.

All irradiations were conducted at  $84 \pm 2$  K in order to reduce defect migration and annealing during irradiation. Measurements conducted immediately following irradiation, while the HFETs were maintained below 85 K, were used to observe the effect of displacement damage to  $I_{gs}$ ,  $I_{ds}$ , capacitance, and gate conductance. Measurements performed at 80 K and at RT following the RT anneal provided insight into the stability of the displacement effects and the annealing mechanisms involved after

irradiation. Figure 52 presents the temperature profile, irradiations, and measurements performed on the HFETs in this experiment.

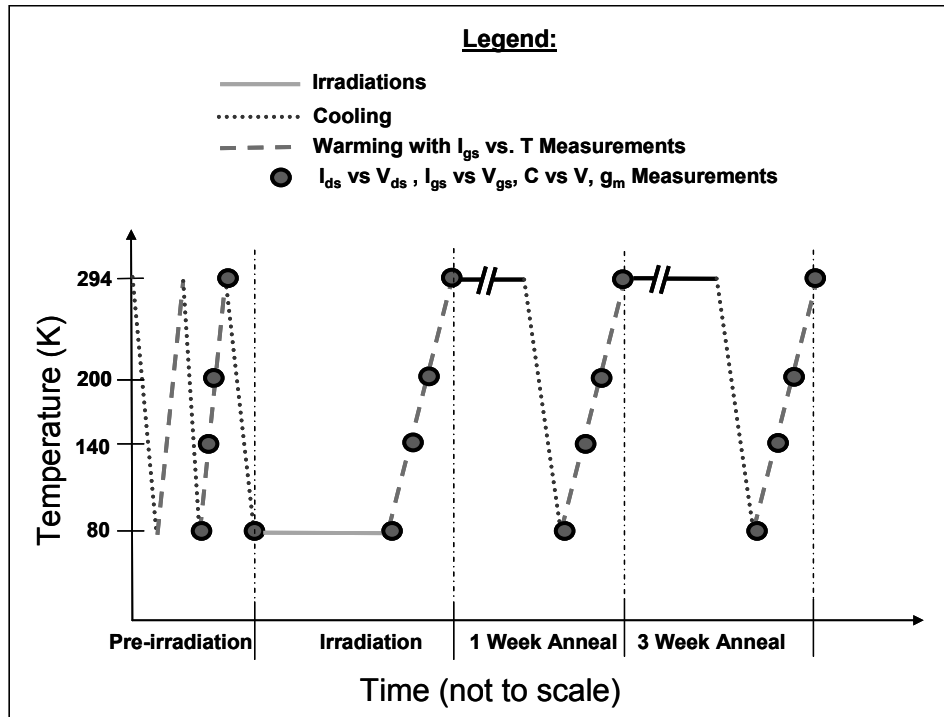


Figure 52. Experimental procedure of the second neutron irradiation experiment showing irradiations, measurements, and temperature profile.

Figure 53 presents the pre- and post-irradiation  $I_{gs}$  as a function of temperature for an unpassivated and passivated HFET. Measurements were made from 82-294 K pre-irradiation and after an exposure to  $1 \times 10^{11}$  n/cm<sup>2</sup> and a  $1 \times 10^{12}$  n/cm<sup>2</sup> respectively. The gate leakage current increased by an average of 18% (0.01 mA at 80 K) in the unpassivated HFET and 16% (0.04 mA at 80 K) in the passivated HFET throughout the temperature range.

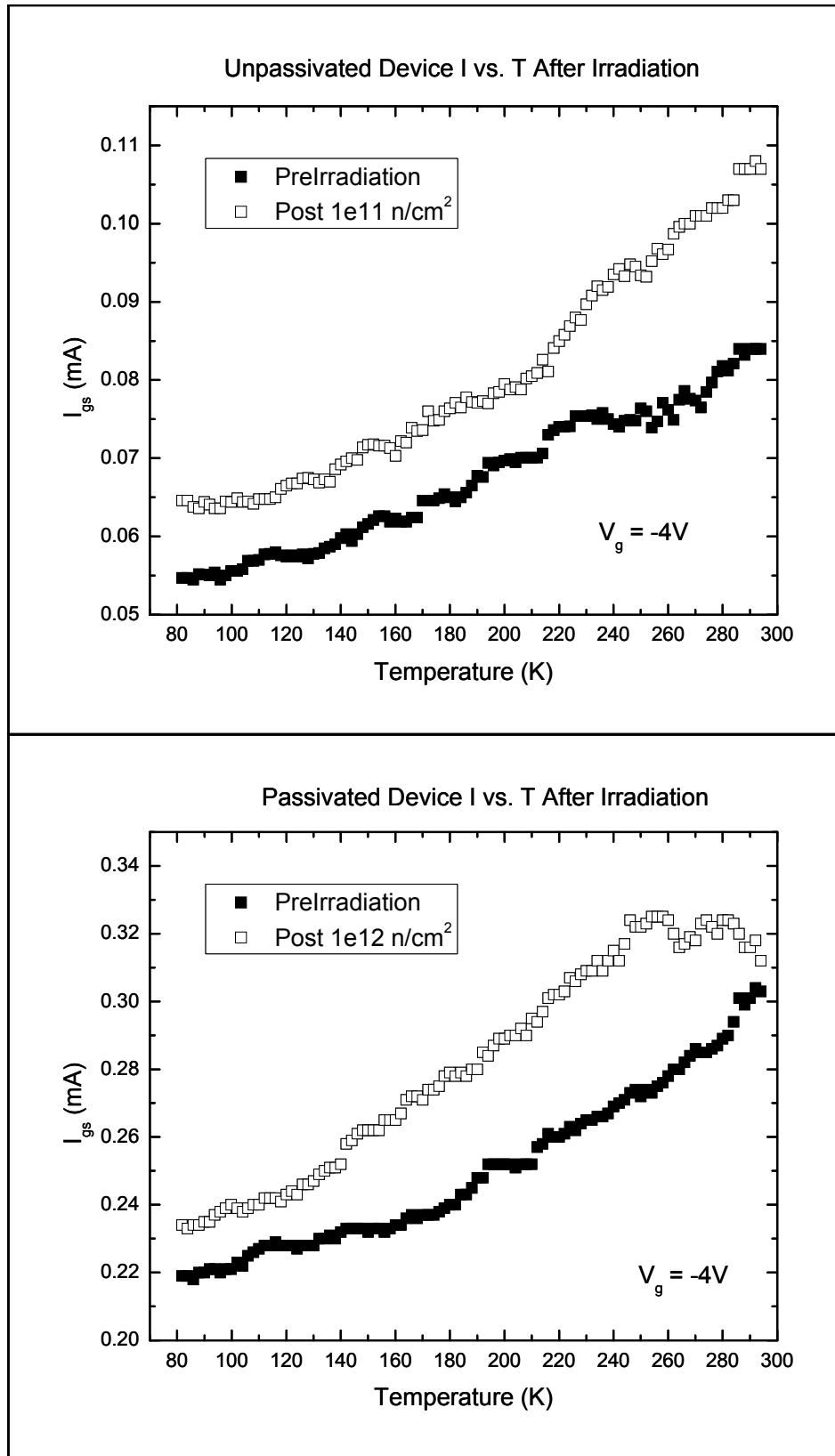


Figure 53. Temperature dependent  $I_{gs}$  before and after neutron irradiation for an unpassivated and a passivated HFET.

Figure 54 presents the pre- and post-irradiation  $I_{ds}$  at 80 K for an unpassivated and passivated HFET.  $I_{ds}$  increases 32% (+5.0 mA) at  $V_{gs} = -2$  V in the saturation region in the unpassivated HFET after a  $10^{11}$  n/cm<sup>2</sup> exposure and 25% (+4.5 mA) at  $V_{gs} = -2$  V in the passivated HFET after a  $10^{12}$  n/cm<sup>2</sup> exposure.

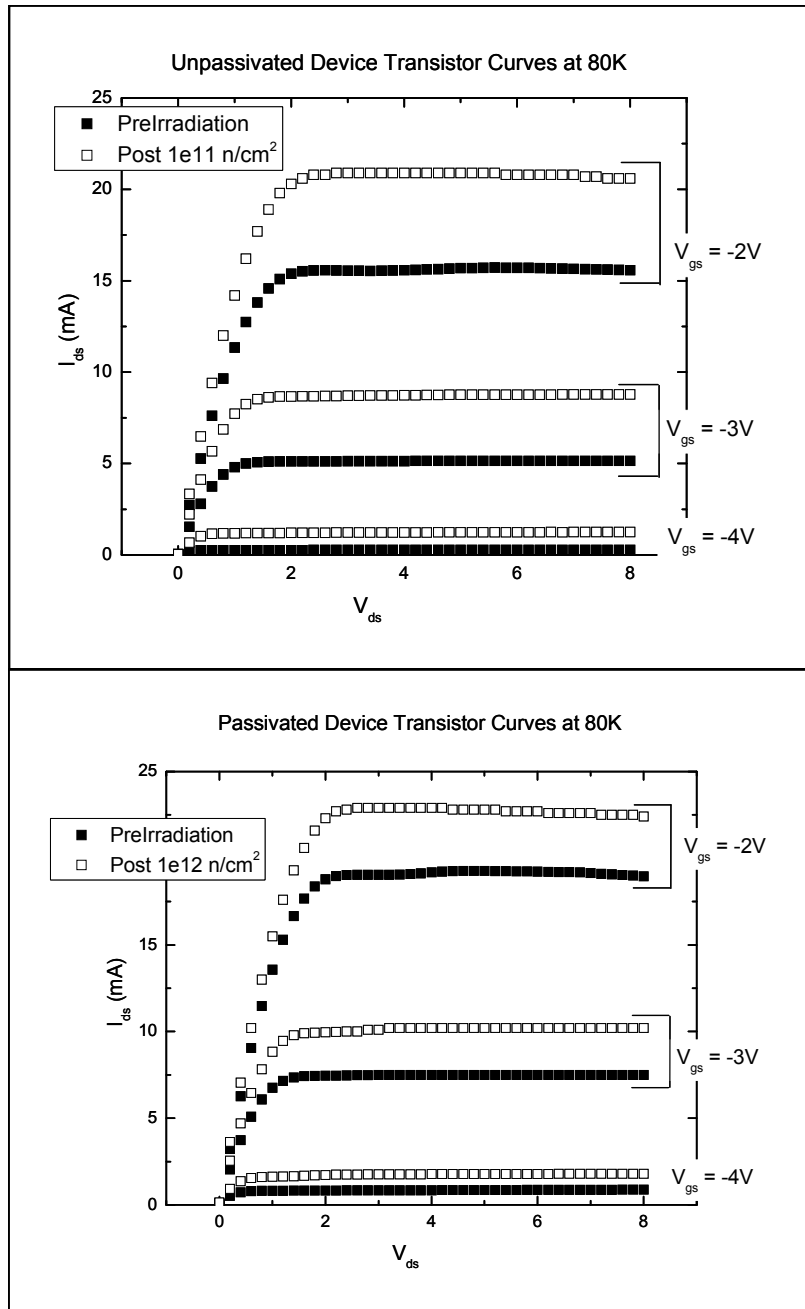


Figure 54. HFET transistor curves measured at 80 K before and after neutron irradiation at 84 K for an unpassivated and a passivated HFET.

Figure 55 presents the pre- and post-irradiation  $I_{ds}$  at 300 K for an unpassivated and passivated HFET. Following irradiation the current in the saturation region decreased 13% (-0.4 mA) for  $V_{gs} = -2$  V after an irradiation of  $10^{11}$  n/cm<sup>2</sup> for the unpassivated HFET and increased 4% (+0.2 mA) for  $V_{gs} = -2$  V after an irradiation of  $10^{12}$  n/cm<sup>2</sup> for the passivated HFET. This temperature-dependent behavior, increased  $I_{ds}$  at low temperature and decreased  $I_{ds}$  at room temperature was consistent for unpassivated but not for passivated HFETs. Some passivated HFETs had either increases or decreases to  $I_{ds}$  at 300 K.

The pre- and post-irradiation C-V measurements at 80 K for an unpassivated and a passivated HFET are presented in Figure 56 and at 300 K in Figure 57. Both HFETs have a slight decrease in capacitance and a threshold voltage shift in the reverse bias direction at 80 K and in the forward bias direction at 300 K. The voltage shift at 80 K of the unpassivated HFET is more pronounced with a -0.2 V shift compared to a shift of only -0.05 V for the passivated HFET. The voltage shift at 300 K for the unpassivated HFET is +0.4 V but less than +0.01 V for the passivated HFET.

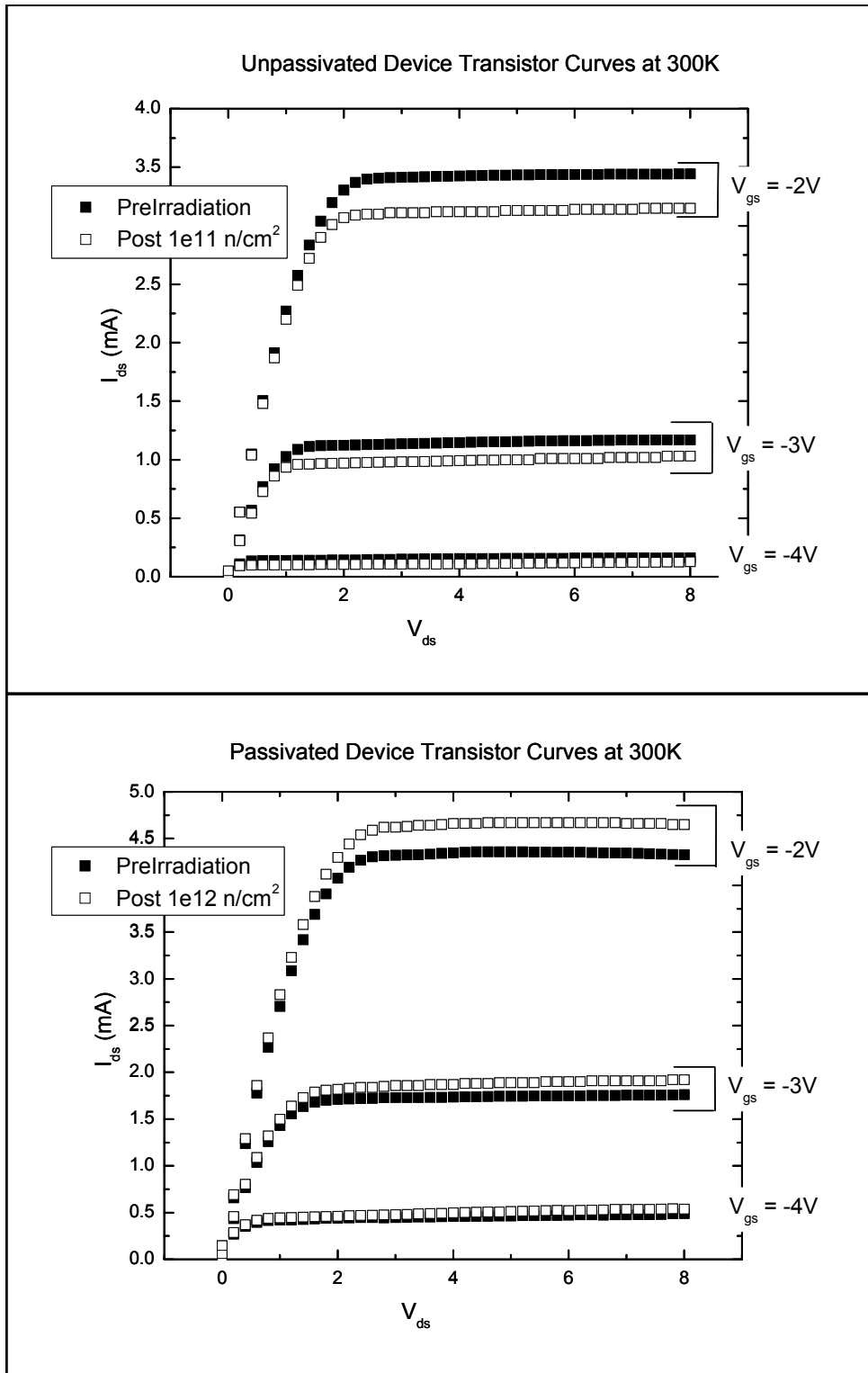


Figure 55. HFET transistor curves measured at 300 K before and after neutron irradiation at 84 K for an unpassivated and a passivated HFET.

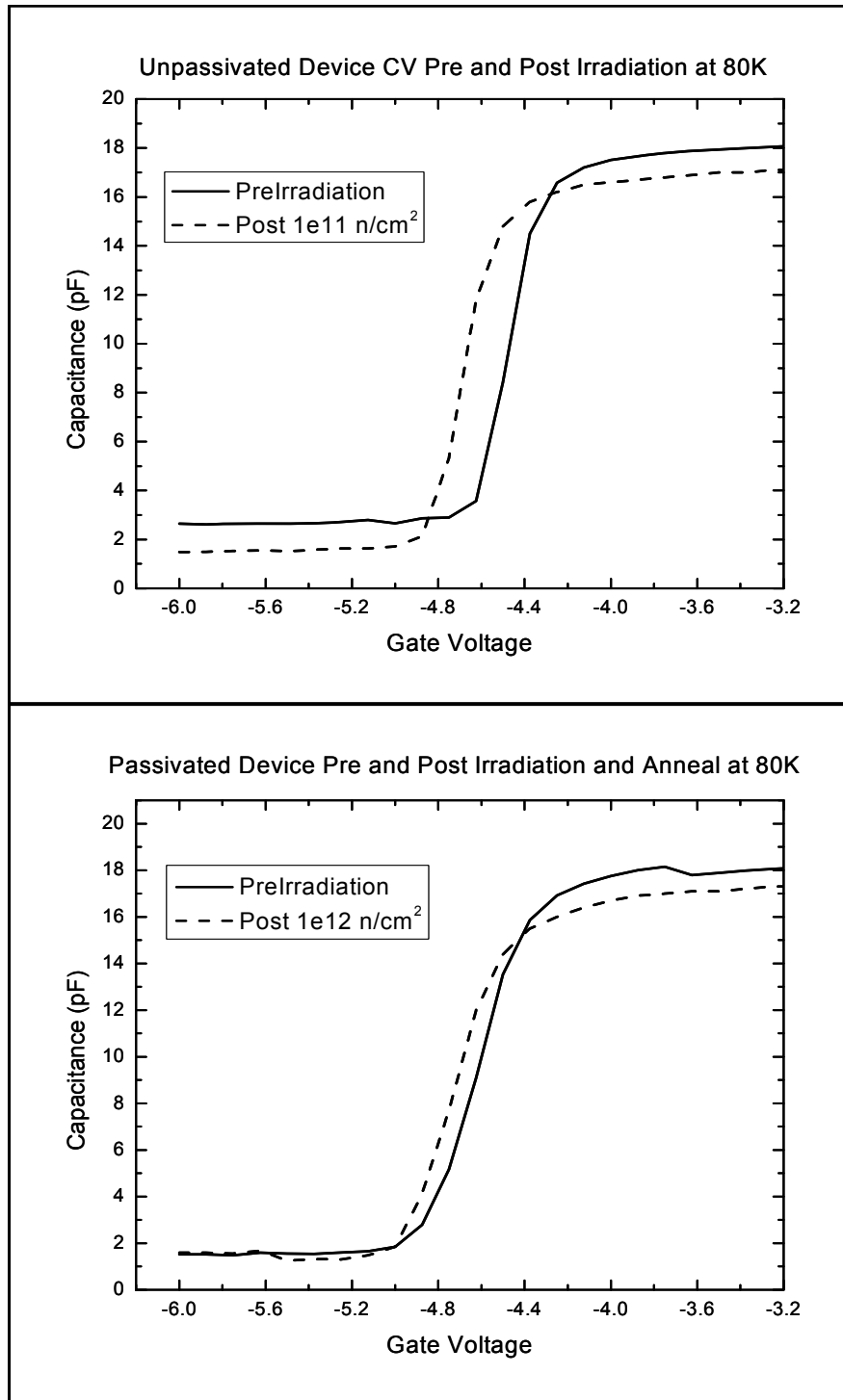


Figure 56. HFET capacitance vs. voltage curves measured at 80 K before and after neutron irradiation at 84 K for an unpassivated and a passivated HFET. The threshold voltage shift is more apparent in the unpassivated HFET.

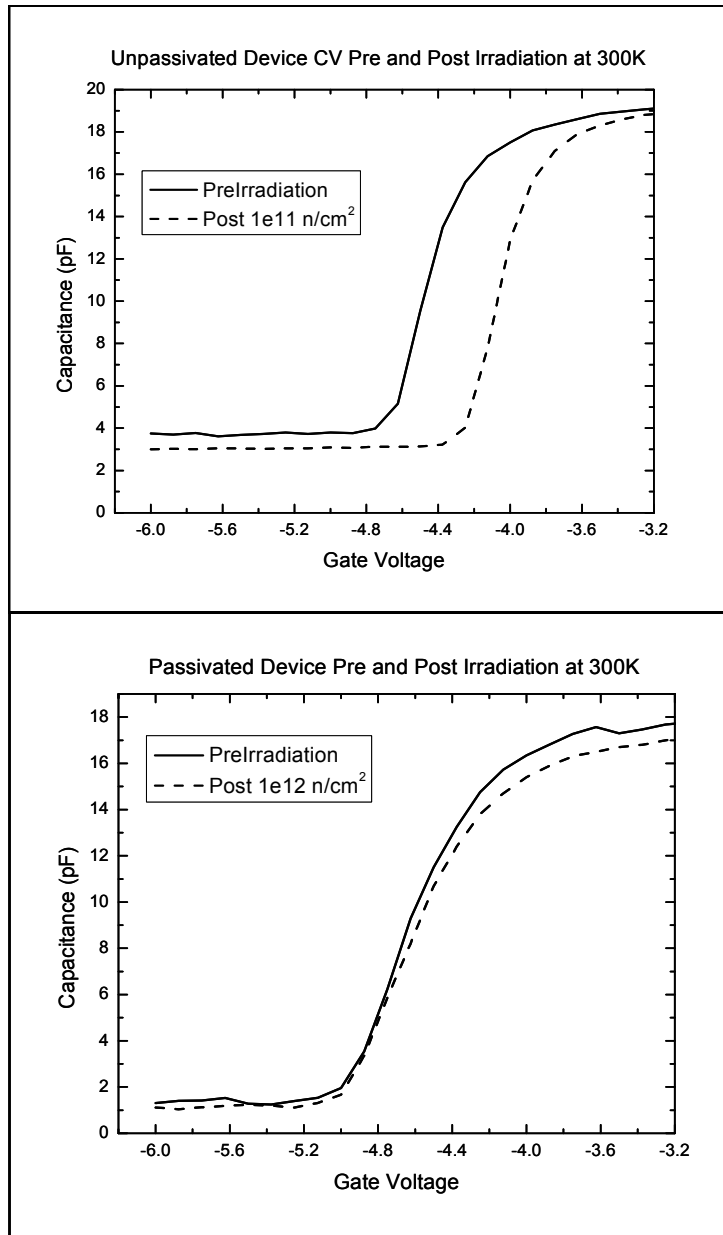


Figure 57. HFET capacitance vs. voltage curves measured at 300 K before and after neutron irradiation at 84 K for an unpassivated and a passivated HFET. The threshold voltage shift is more apparent in the unpassivated HFET.

The pre- and post-irradiation gate conductance vs. voltage measurements at 80 K for an unpassivated and passivated HFETs are presented in Figure 58 and at 300 K in Figure 59. Both HFETs show an increase in gate conductance and a shift in the peak gate conductance voltage in the reverse bias direction at 80 K. The voltage shift at 80 K of the



unpassivated HFET is more pronounced with a -0.2 V shift compared to a shift of less than -0.01 V for the passivated HFET. The voltage shift at 300 K for the unpassivated HFET is +0.38 V but less than +0.01 V for the passivated HFET. The peak gate conductance at 80 K increases by 35% for both the unpassivated and passivated HFET. The peak gate conductance at 300 K decreases by 35% for the unpassivated HFET but increases by 10% for the passivated HFET.

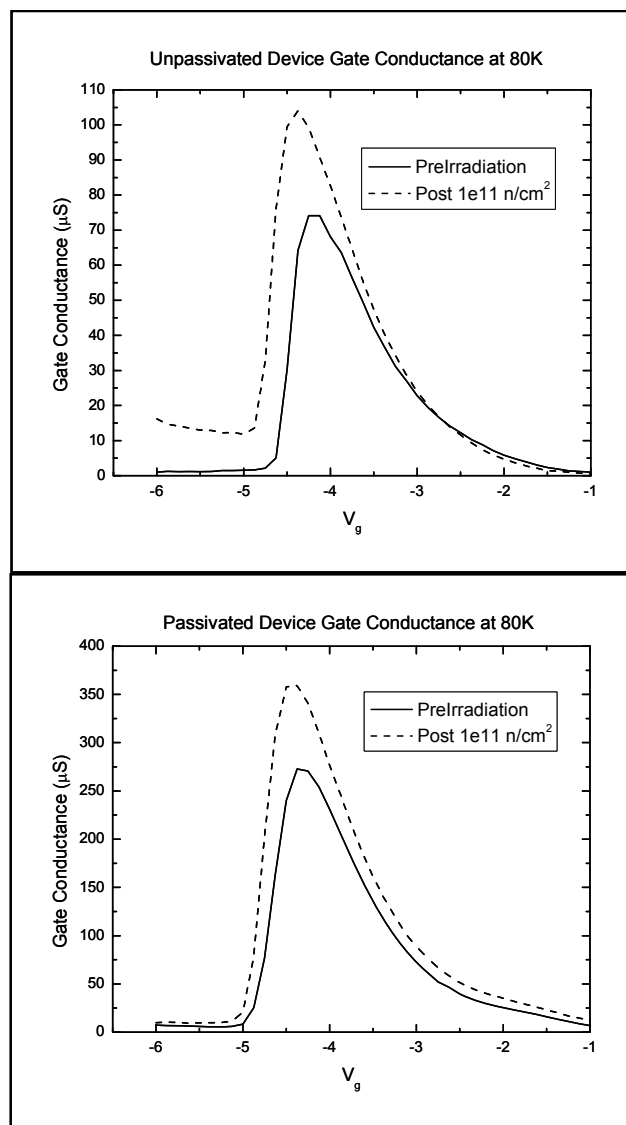


Figure 58. HFET gate conductance vs. voltage curves measured at 80 K before and after neutron irradiation at 84 K for an unpassivated and a passivated HFETs. The shift in the peak gate conductance is more apparent in the unpassivated HFET.

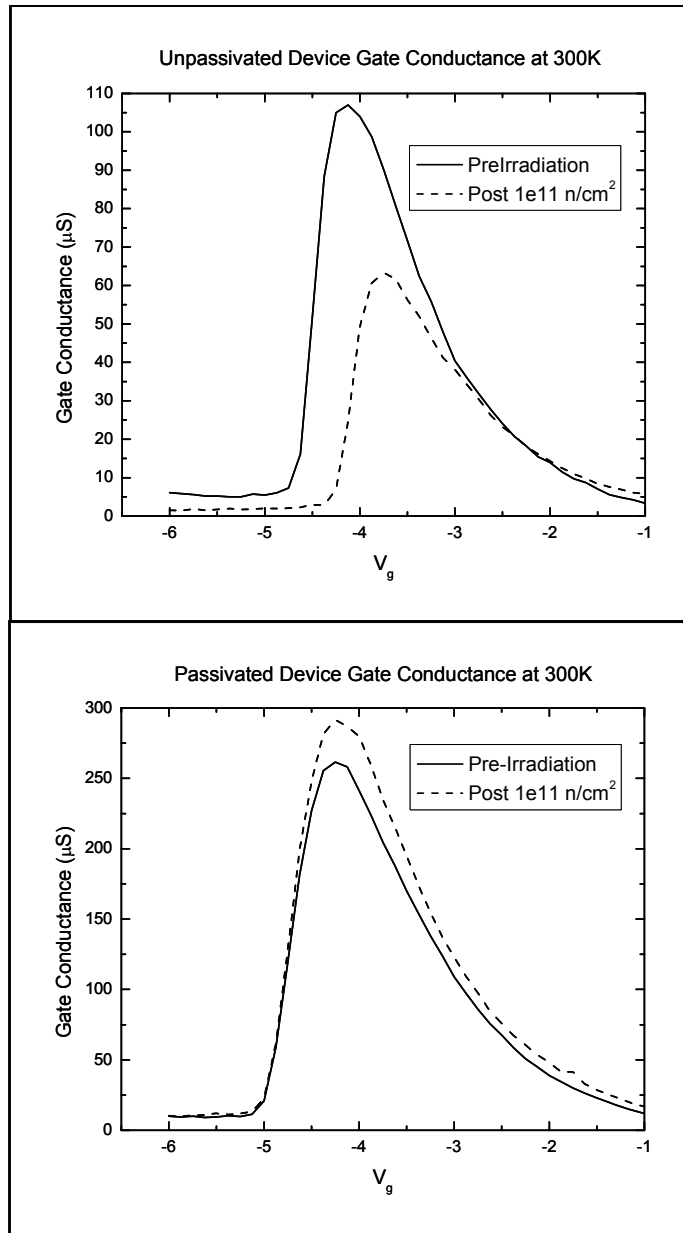


Figure 59. HFET gate conductance vs. voltage curves measured at 300 K before and after neutron irradiation at 84 K for an unpassivated and a passivated HFETs. The shift in the peak gate conductance is more apparent in the unpassivated HFET. The peak level is reduced in the unpassivated HFET but slightly increased in the passivated HFET.

Figure 60 presents  $I_{gs}$  as a function of temperature after a one-week and a four-week RT anneal for an unpassivated and a passivated HFET. The current did not return to its pre-irradiation value after annealing. Instead it either stayed at the pre-irradiation value or increased slightly across the entire temperature range in each case. The

post-anneal data closely matches the measurement immediately after irradiation above 220 K indicating that permanent defects had formed during annealing with an activation temperature of  $\sim 220$  K similar to the results in the first neutron experiment.

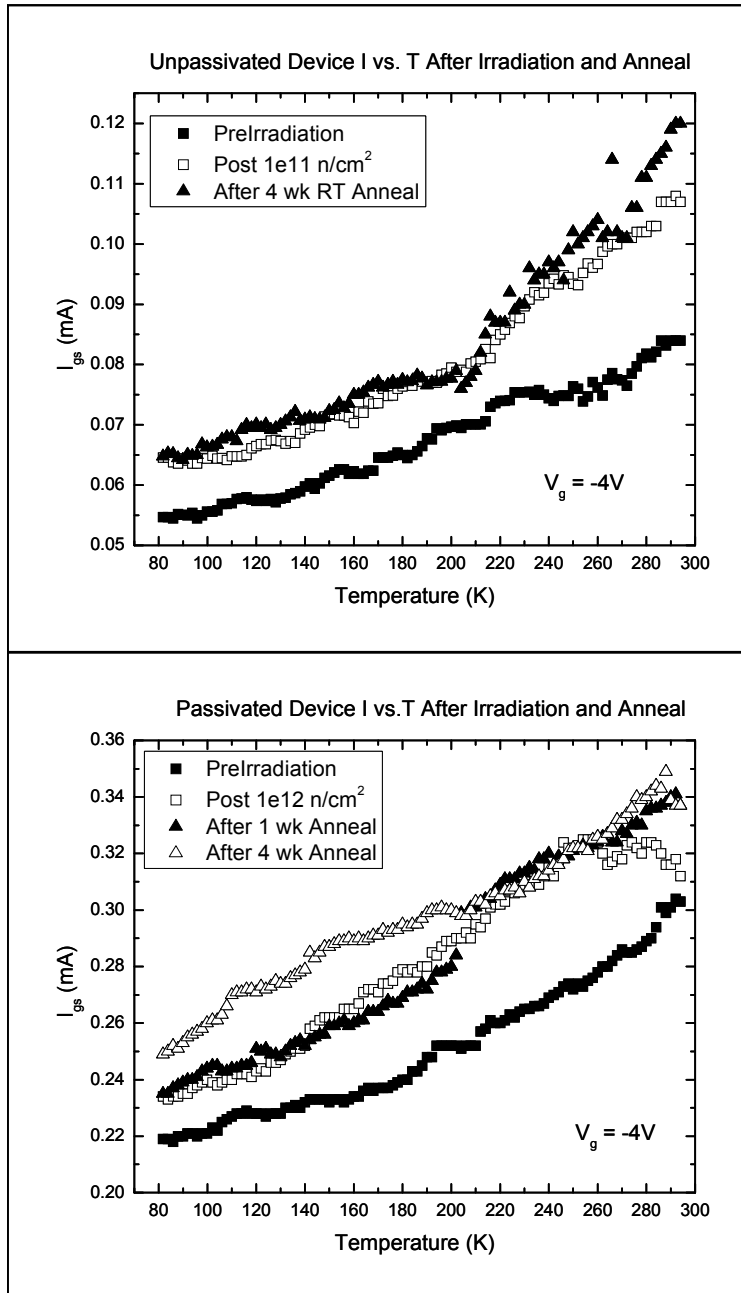


Figure 60. Temperature-dependent  $I_{gs}$  before and after neutron irradiation and after one- and four-week room-temperature anneals for unpassivated and passivated HFETs.

Figure 61 presents  $I_{ds}$  at low temperature (80 K) following a one-week and a four-week RT anneal for an unpassivated and a passivated HFET. For the unpassivated HFET the current in the saturation region initially super-recovered lower than its pre-irradiation value after the first anneal. It then rebounded after three more weeks close to the pre-irradiation values. For the passivated HFET the current in the saturation region fully recovered to its pre-irradiation value after the first anneal and remained there after the second annealing period.

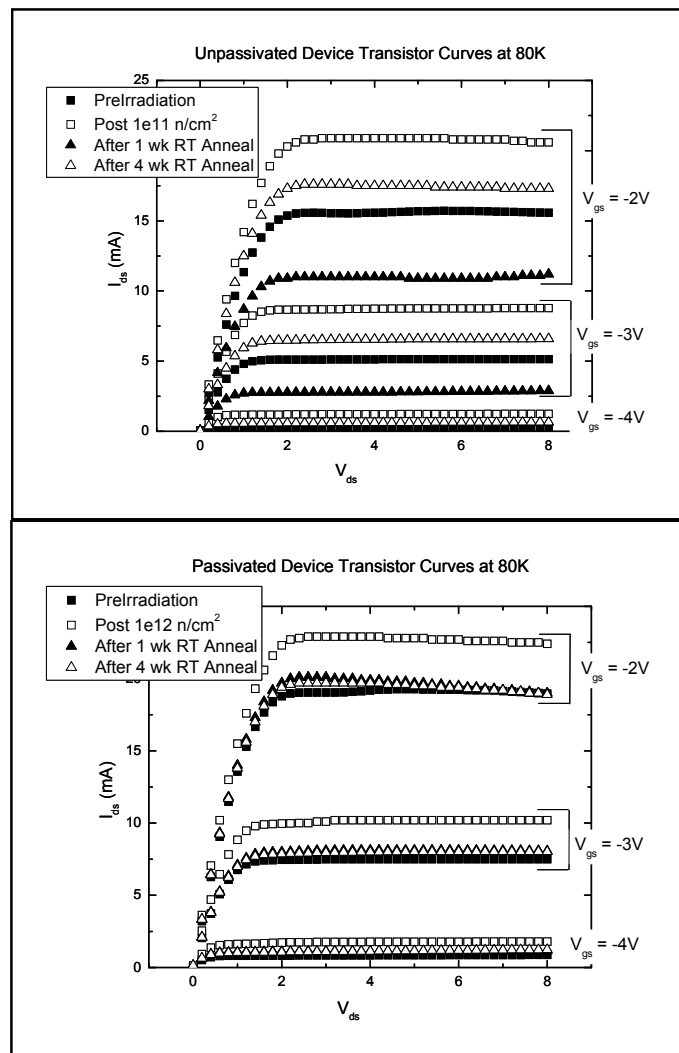


Figure 61. HFET transistor curves measured at 80 K before and after neutron irradiation at 84 K and after one- and four-week room-temperature anneals for unpassivated and passivated HFETs.

Figure 62 presents  $I_{ds}$  at RT after a one-week and a four-week RT anneal for an unpassivated and a passivated HFET. For the unpassivated HFET the current in the saturation region initially continued lower than its initial post-irradiation value after the first anneal. It then rebounded after three more weeks close to the post-irradiation values. This device never recovered fully to its pre-irradiation value. For the passivated HFET the current in the saturation region fully recovered to its pre-irradiation value after the first anneal and remained after the second annealing period.

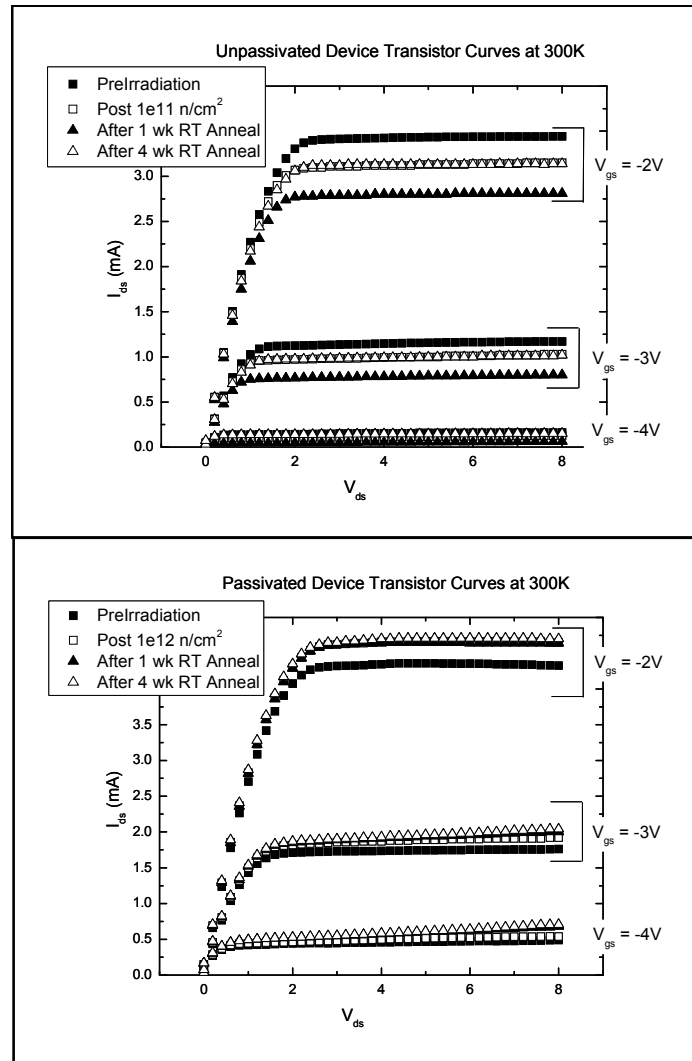


Figure 62. HFET transistor curves measured at 304 K before and after neutron irradiation at 84 K and after one- and four-week room-temperature anneals for unpassivated and passivated HFETs.

Figure 63 presents the high frequency (1 MHz) C-V measurement at low temperature (80 K) following a one-week and a four-week RT anneal for an unpassivated and a passivated HFET. The threshold voltage of the unpassivated HFET shifts back in the forward bias direction past the pre-irradiation value after the initial one-week anneal at 80 K. After an additional three weeks of RT annealing, the threshold voltage shifts back toward but still less than the pre-irradiation value. The threshold voltage shift of the passivated HFET is negligibly different from the pre-irradiation value after the RT anneal.

Figure 64 presents the high frequency (1 MHz) C-V measurement at high temperature (300 K) following a one-week and a four-week RT anneal for an unpassivated and a passivated HFET. The threshold voltage of the unpassivated HFET increases in the forward bias direction after the initial one-week anneal at 80 K. After an additional three weeks of RT annealing the threshold voltage shifts back in the reverse bias direction past the initial post-irradiation value, but still less than the pre-irradiation value. The threshold voltage shift of the passivated HFET is negligibly different from the post-irradiation value after the RT anneals.

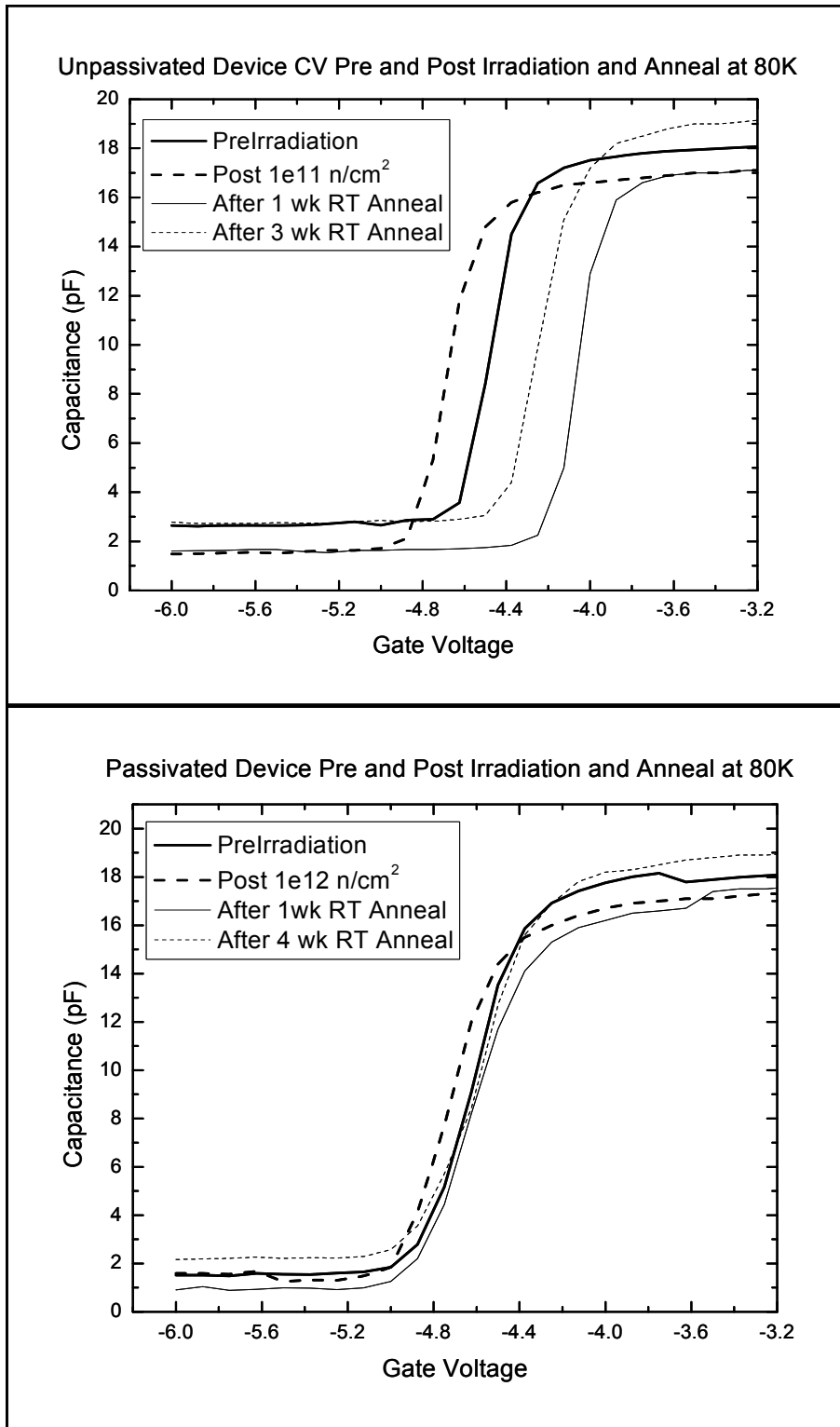


Figure 63. HFET capacitance vs. voltage curves measured at 80 K before and after neutron irradiation at 84 K and after one- and four-week room-temperature anneals for unpassivated and passivated HFETs.

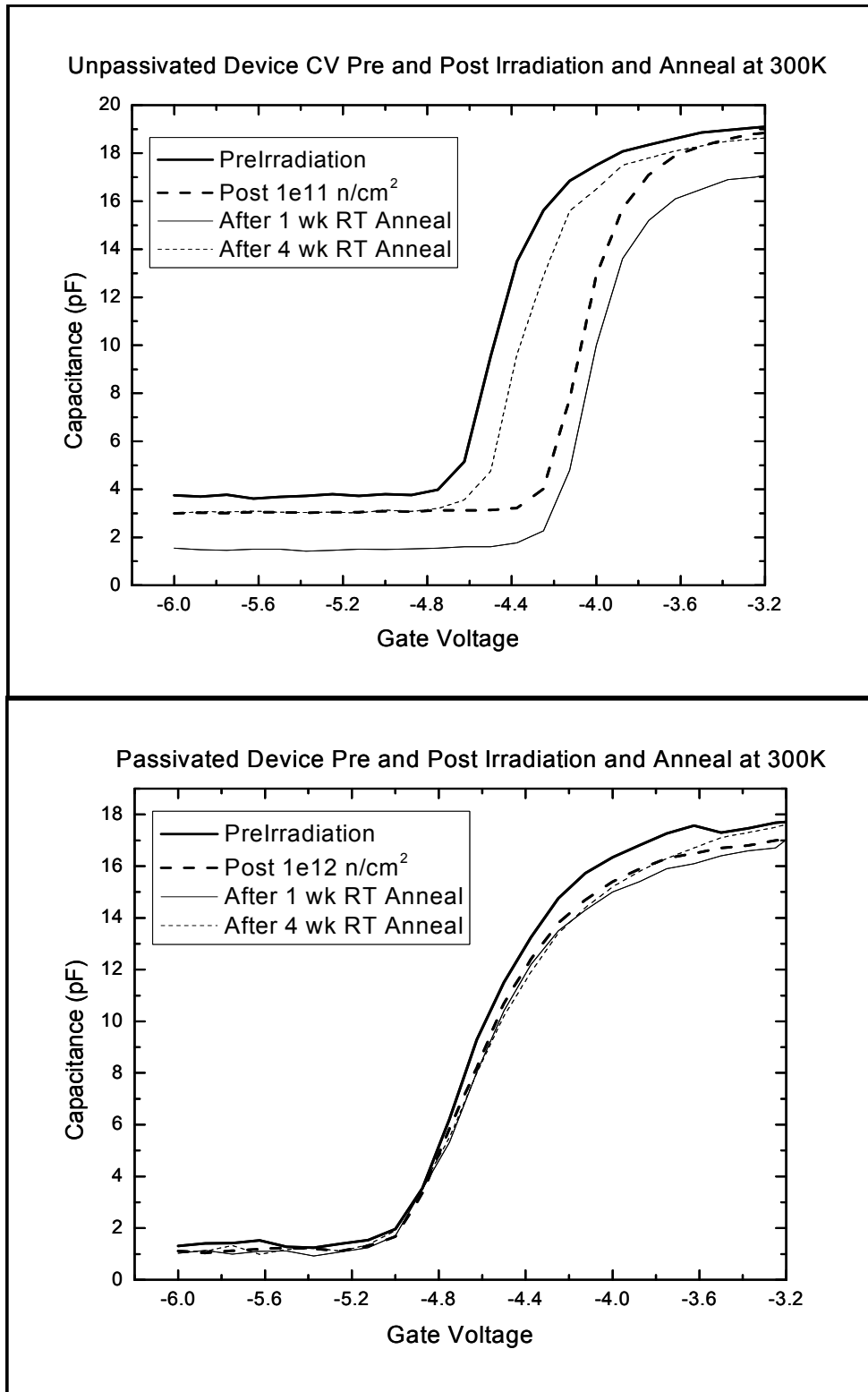


Figure 64. HFET capacitance vs. voltage curves measured at 300 K before and after neutron irradiation at 84 K and after one- and four-week room-temperature anneals for unpassivated and passivated HFETs.



Figure 65 presents the DC gate conductance vs. voltage measurement at low temperature (80 K) following a one-week and a four-week RT anneal for an unpassivated and a passivated HFET. Both HFETs show an decrease in gate conductance and a shift in the peak gate conductance voltage in the forward bias direction at 80 K from the post-irradiation values after a one-week RT anneal. The shift is past the pre-irradiation value for the unpassivated HFET and between the pre- and post-irradiation values for the passivated HFET. Additionally, the changes in the unpassivated HFET are more pronounced than in the passivated HFET. After the additional three weeks of RT anneal the peak gate conductance in the unpassivated HFET is above the pre-irradiation value with no threshold voltage shift. The peak gate conductance of the passivated HFET is slightly above the post-irradiation with no threshold voltage shift.

Figure 66 presents the DC gate conductance vs. voltage measurement at high temperature (300 K) following a one-week and a four-week RT anneal for an unpassivated and a passivated HFET. The unpassivated HFET shows no change in the peak gate conductance from the post-irradiation value after a one-week RT anneal. The passivated HFET shows an increase but no shift in the peak gate conductance from the post-irradiation value after a one-week RT anneal. Both devices show an increase in the peak gate conductance, higher than the pre-irradiation value with no voltage shift after an additional three weeks of RT anneal.

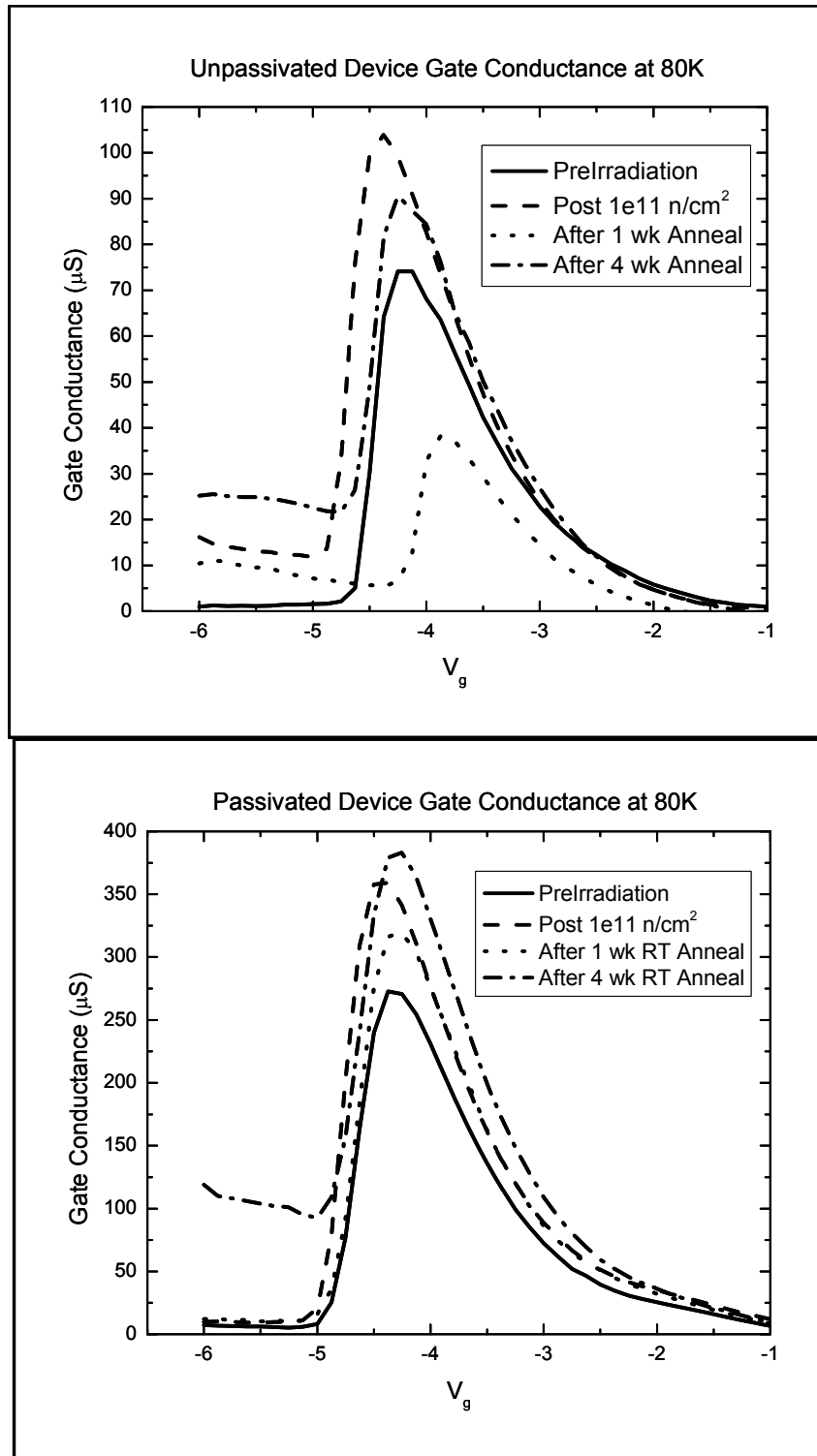


Figure 65. HFET gate conductance vs. voltage curves measured at 80 K before and after neutron irradiation at 84 K and after one- and four-week room-temperature anneals for unpassivated and passivated HFETs.

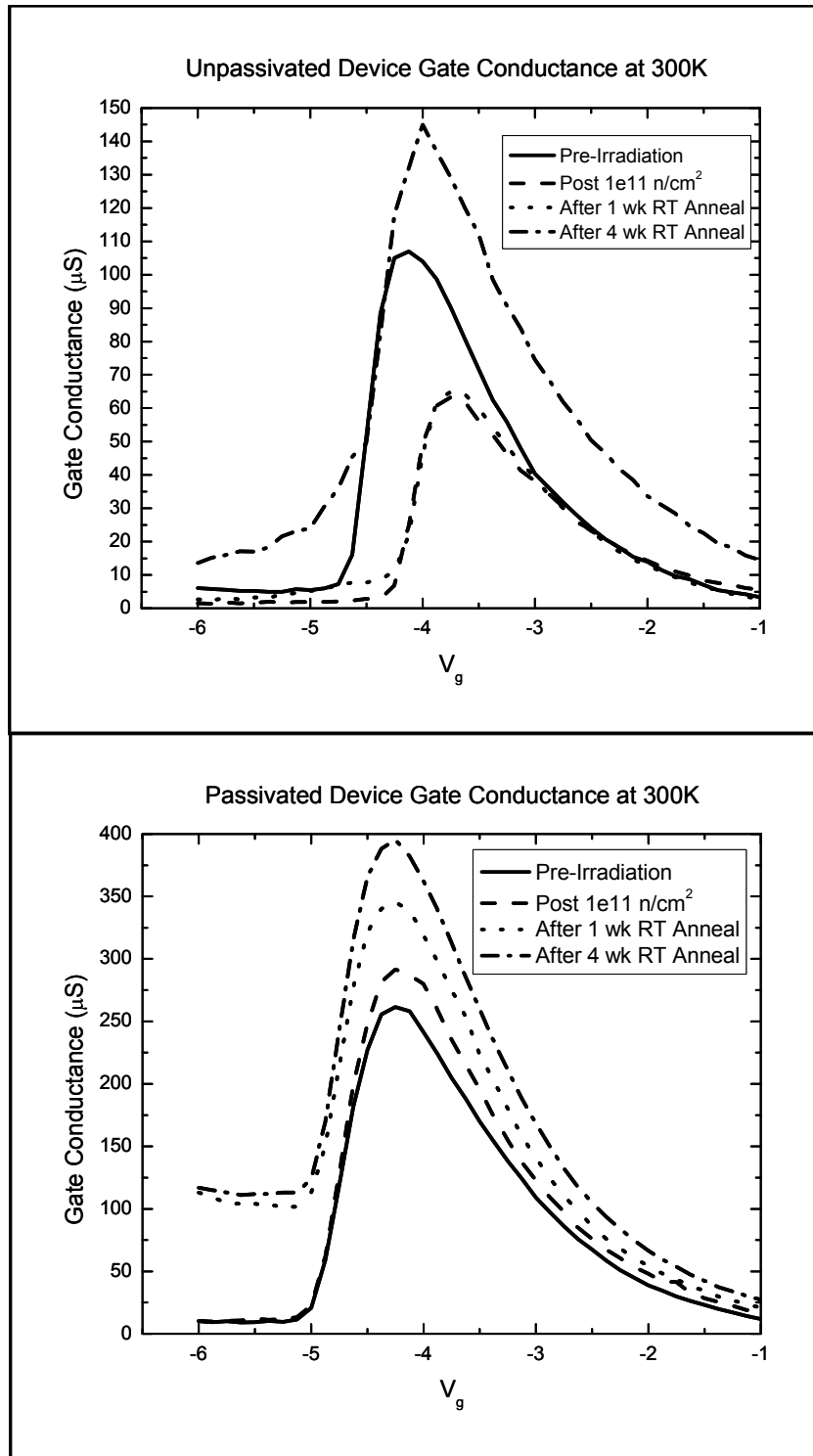


Figure 66. HFET gate conductance vs. voltage curves measured at 300 K before and after neutron irradiation at 84 K and after one- and four-week room-temperature anneals for unpassivated and passivated HFETs.

### **5.3 Modeling Results**

The focus of the Trap-Assisted Tunneling (TAT) modeling was to determine the parameters that characterize the gate region of the HFET and to ascertain how they changed with radiation. The process used included matching the pre- and post-irradiation data for gate leakage current. The four parameters of the model were allowed to vary in order to get the best fit to the gate leakage current data. Figures 67 and 68 are representative fittings of the TAT model to pre-irradiation experimental data for an unpassivated and passivated HFET respectively. For the unpassivated HFET the fitting includes two curves;  $I_{gs}$ - $T$  at a fixed gate voltage of -4 V, and  $I_{gs}$ - $V_g$  at a fixed temperature of 200 K. For the passivated HFET the two curves are  $I_{gs}$ - $T$  at a fixed gate voltage of -4 V, and  $I_{gs}$ - $V_g$  at a fixed temperature of 140 K. One standard deviation error bars are included on the experimental data points. In both cases there is greater variation from the data at higher temperature, more so in the case of the passivated HFET.

As the fit approaches the low end of the temperature scale, towards 80 K, there is a different shape to the fitted curve in the unpassivated HFETs versus the passivated HFETs. This is due to the difference in Schottky barrier height. The smaller Schottky barrier height in the passivated devices causes a more pronounced increase in the current at lower temperature. This is as expected and visible in both the data and the fitted line.

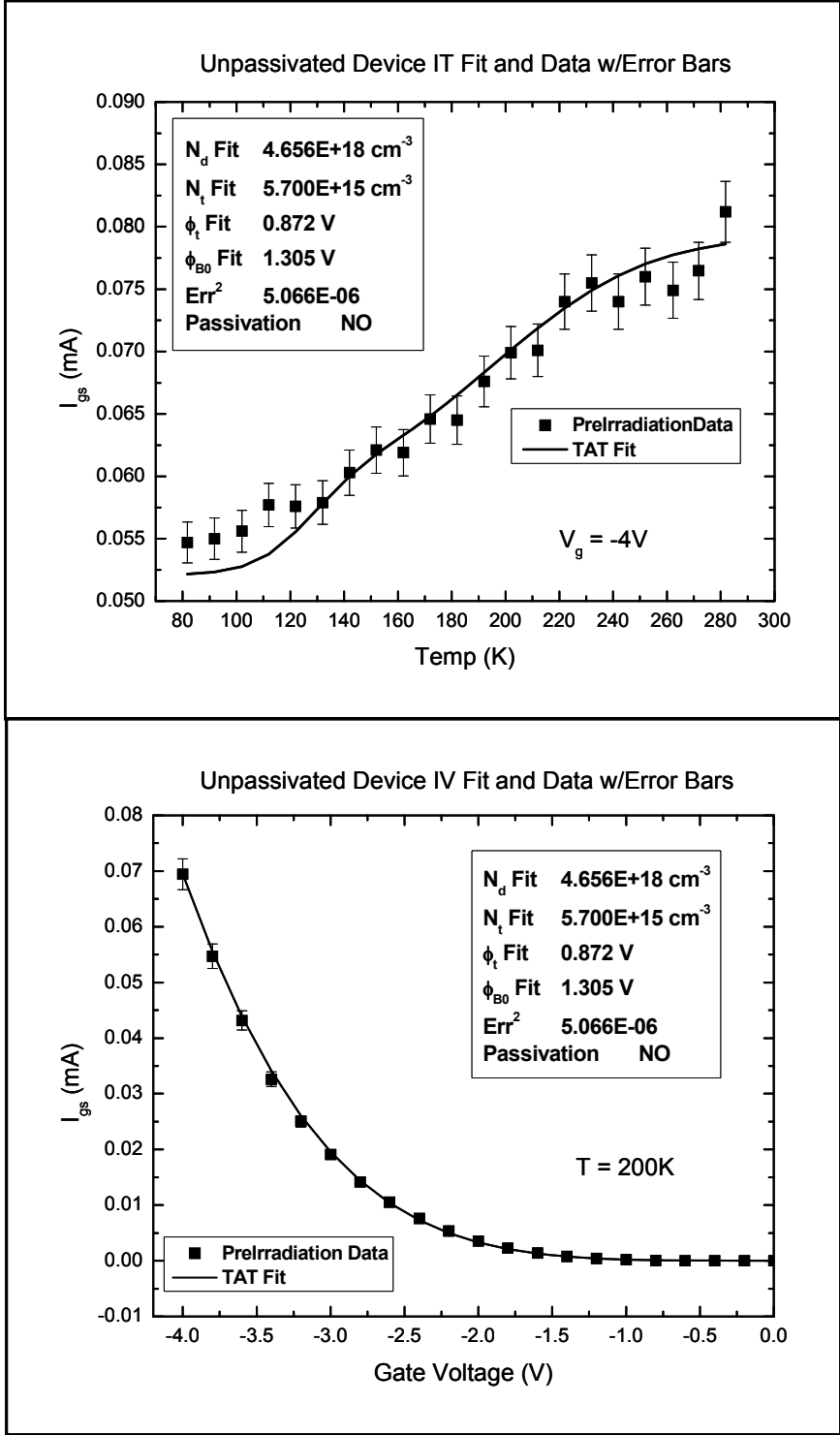


Figure 67. Pre-irradiation gate leakage current vs. temperature at a fixed voltage and gate leakage current vs. voltage at a fixed temperature for an unpassivated HFET. The data with error bars is displayed along with the best fit using the TAT model.

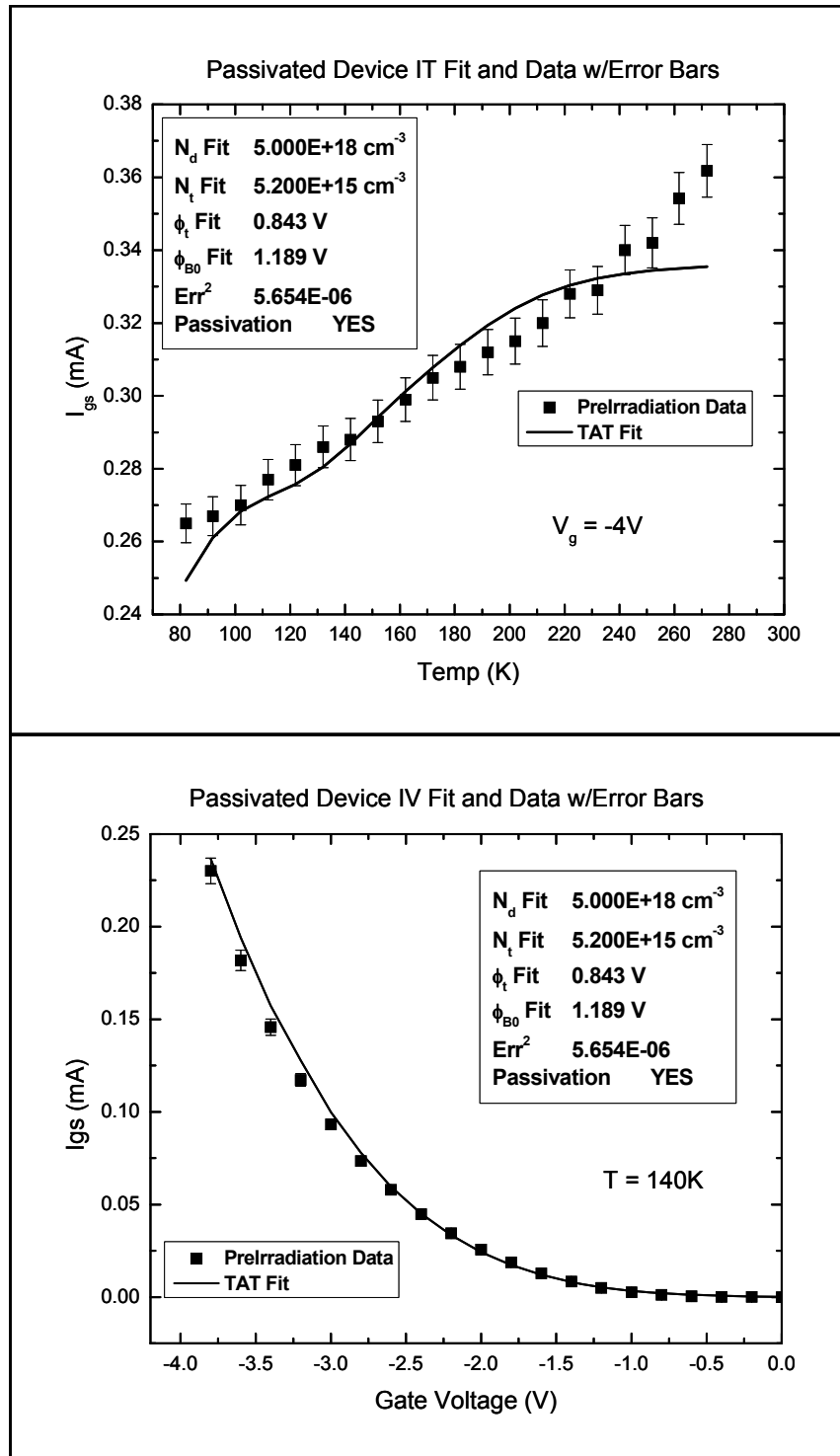


Figure 68. Pre-irradiation gate leakage current vs. temperature at a fixed voltage and gate leakage current vs. voltage at a fixed temperature for a passivated HFET. The data with error bars is displayed along with the best fit using the TAT model.

In order to determine the influence on the change in gate current after irradiation for each parameter, each parameter was individually varied while keeping the other three parameters fixed. Figure 69 shows the change in gate current from the pre-irradiation fit as the optimization program attempted to fit the model to the post-irradiation data while varying only one parameter at a time. Starting with the pre-irradiation parameters as determined by the model fit to the pre-irradiation data, each parameter was individually varied. The optimization algorithm was used to adjust the parameters to fit the post-irradiation data. The result is a best fit line to the data while varying each parameter individually. A Schottky barrier height,  $\phi_b$ , only adjustment gives a poor fit while varying only the trap height,  $\phi_t$ , the donor concentration,  $N_d$ , and the trap concentration,  $N_t$ , provide near fits to the post-irradiation data. Varying  $N_t$  only provides the best possible fit in both cases.

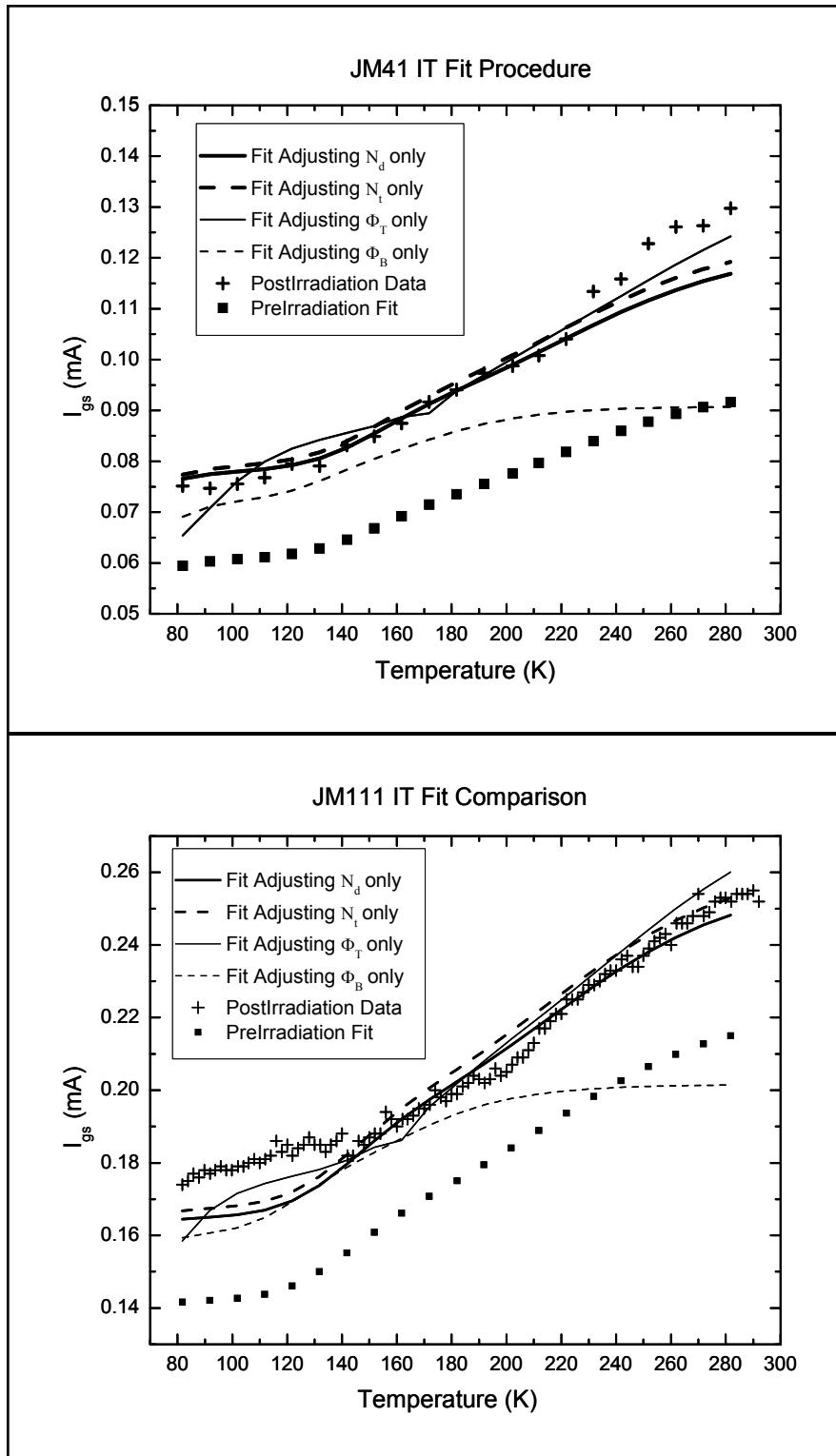


Figure 69. Pre- and post-irradiation gate leakage current vs. temperature at a gate voltage of -4 V for unpassivated HFETs. Each of the four parameters of the model are varied independently from their pre-irradiation fitted values in order to match the post-irradiation data.



Figures 70, 71, and 72 show three examples of HFET gate current fitting with  $I_{gs}$ -T at a fixed gate voltage of -4 V and  $I_{gs}$ - $V_g$  at a fixed temperature that varies for each case. In each case the dominant parameter change is the trap density,  $N_t$ , as in the figures.

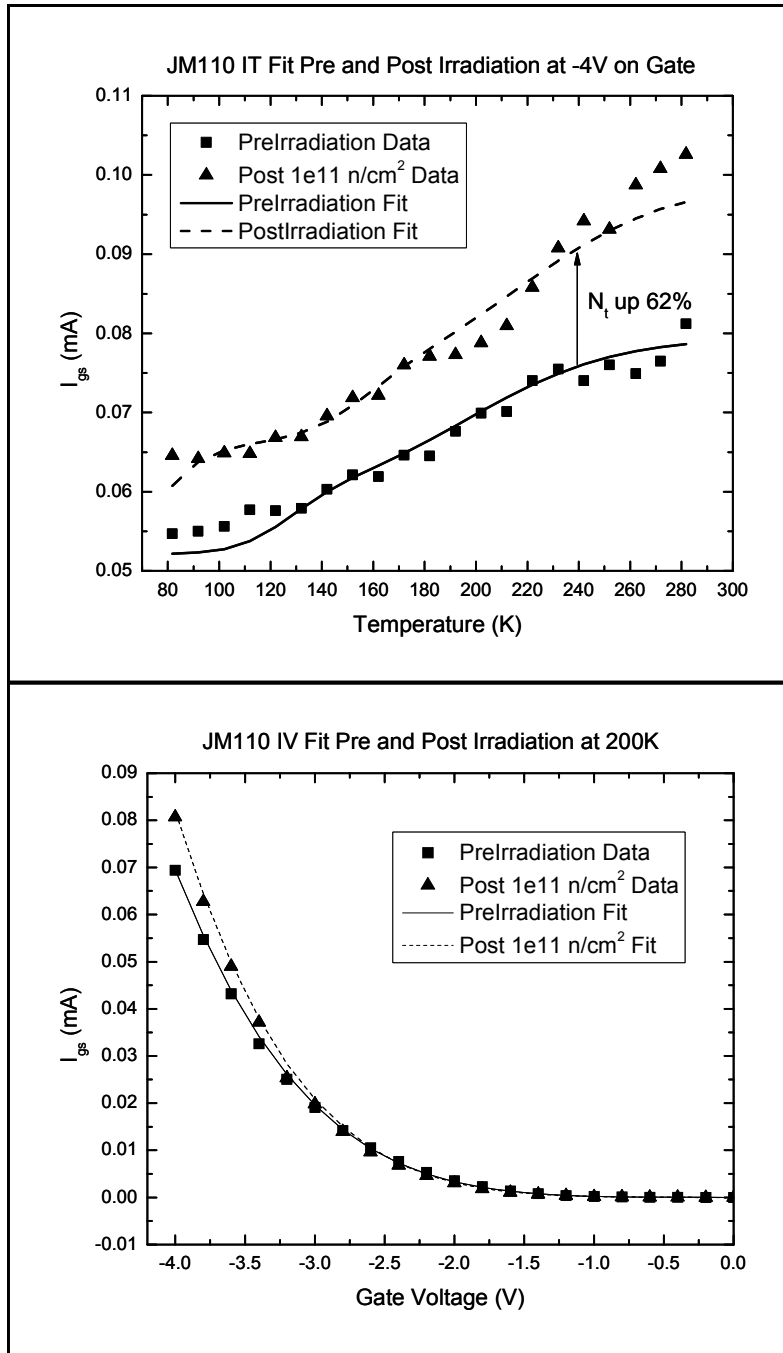


Figure 70. Pre- and post-irradiation gate leakage current vs. temperature at a fixed voltage and gate leakage current vs. voltage at a fixed temperature for an unpassivated HFET (JM110). The data is displayed along with the best fit using the TAT model.

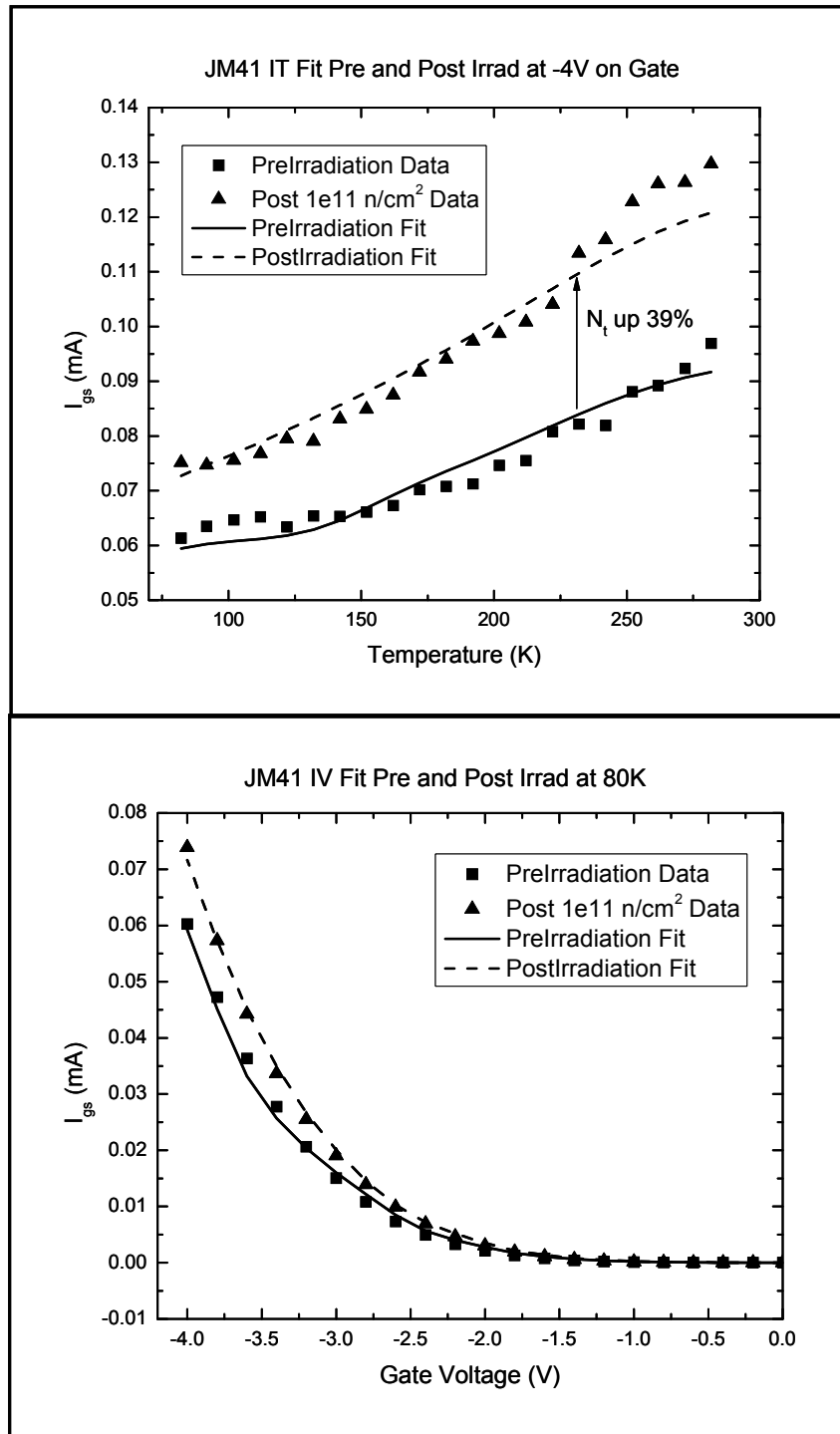


Figure 71. Pre- and post-irradiation gate leakage current vs. temperature at a fixed voltage and gate leakage current vs. voltage at a fixed temperature for an unpassivated HFET (JM41). The data is displayed along with the best fit using the TAT model.

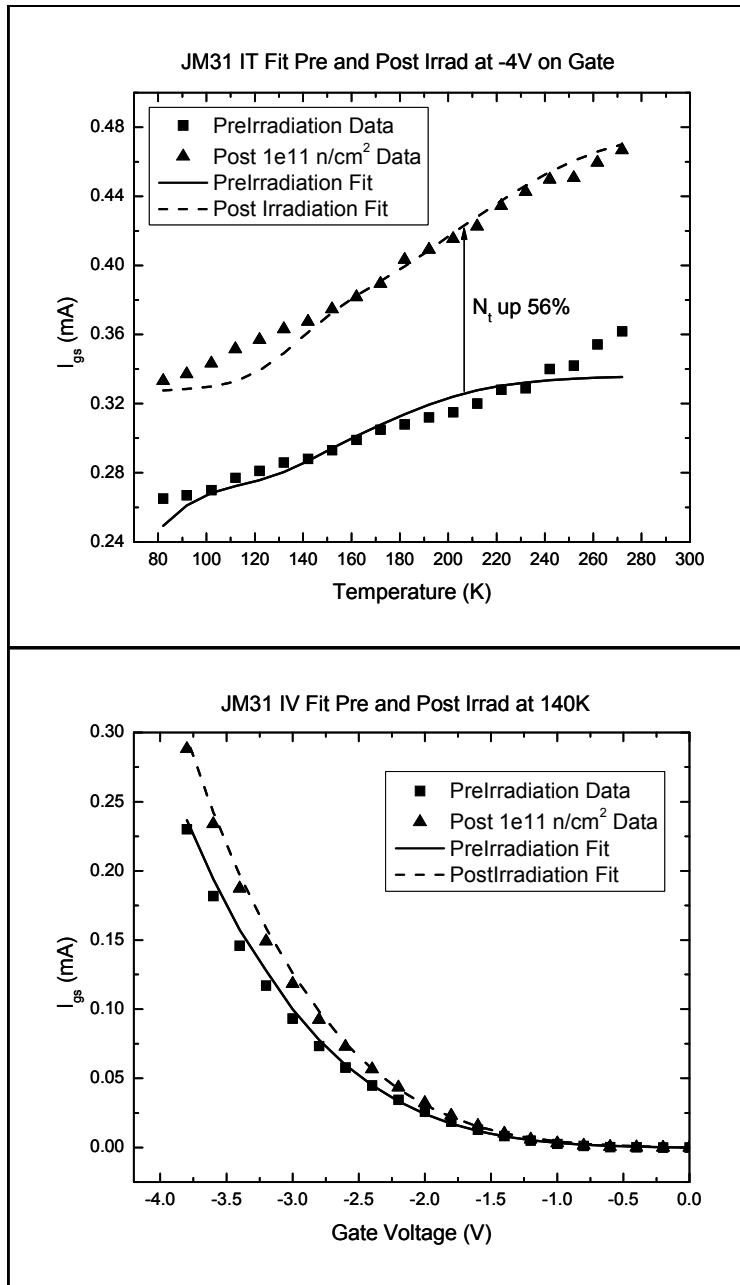


Figure 72. Pre- and post-irradiation gate leakage current vs temperature at a fixed voltage and gate leakage current vs. voltage at a fixed temperature for a passivated HFET (JM31). The data is displayed along with the best fit using the TAT model.

Table 11 shows the pre- and post-irradiation fitting parameters for all twelve of the HFETs. The change in the parameters from pre- to post-irradiation values and the percentage change as well as the R-RMSE values are included for comparison.

Table 11. Modeling Results Pre- and Post-Irradiation

I <sub>gs</sub> -T Fit from 80-290 K at -4 V <sub>g</sub>														
I <sub>gs</sub> -V <sub>g</sub> from -4 to 0 V at 80 K														
HFET #	Pre-Irradiation							Post Irradiation						
	N <sub>d</sub> Fit x10 <sup>18</sup> cm <sup>-3</sup>	N <sub>t</sub> Fit x10 <sup>15</sup> cm <sup>-3</sup>	φ <sub>t</sub> Fit eV	φ <sub>b</sub> Fit eV	R-RMSE μA	Irradiation n/cm <sup>2</sup>	ΔN <sub>d</sub> Fit x10 <sup>18</sup> cm <sup>-3</sup>	ΔN <sub>t</sub> Fit x10 <sup>15</sup> cm <sup>-3</sup>	%	Δφ <sub>t</sub> Fit eV	%	Δφ <sub>b</sub> Fit eV	%	R-RMSE μA
Unpassivated														
JM16	4.06	4.24	0.851	1.30	2.30	1x10 <sup>12</sup>	+0.15	+4%	+93%	+0.052	+6%	+0.04	+3%	3.20
JM18	4.04	5.68	0.834	1.26	7.83	1x10 <sup>09</sup>	+0.00	0%	0%	-0.010	-1%	+0.00	0%	9.81
JM41	4.06	4.13	0.886	1.33	4.27	1x10 <sup>11</sup>	+0.11	+3%	+41%	+0.024	+2%	+0.03	+2%	5.23
JM42	4.69	5.92	0.888	1.30	3.88	1x10 <sup>10</sup>	-0.05	-1%	+17%	-0.007	-1%	+0.01	+1%	2.84
JM110	4.06	4.15	0.905	1.34	1.26	1x10 <sup>11</sup>	-0.12	-3%	+68%	+0.021	+2%	+0.04	+3%	2.79
JM111	4.67	5.70	0.875	1.31	4.30	1x10 <sup>13</sup>	-0.01	-1%	+51%	+0.018	+2%	+0.02	+2%	8.78
Passivated														
JM23	5.00	3.40	0.860	1.22	6.28	1x10 <sup>12</sup>	+0.20	+4%	+12%	+0.00	0%	+0.01	+1%	14.0
JM26	5.00	6.00	0.899	1.26	12.90	1x10 <sup>11</sup>	+0.15	+3%	+73%	+0.036	+4%	+0.12	+10%	10.7
JM29	5.10	2.20	0.838	1.15	7.28	1x10 <sup>10</sup>	+0.27	+5%	+200%	+0.065	+8%	+0.20	+17%	3.91
JM31	5.00	5.20	0.843	1.19	5.65	1x10 <sup>11</sup>	-0.11	-2%	+48%	+0.004	+1%	+0.02	+2%	6.42
JM32	5.00	4.00	0.864	1.22	3.16	1x10 <sup>13</sup>	-0.03	-1%	+55%	-0.003	-1%	+0.08	+7%	4.59
JM34	5.55	9.83	0.938	1.32	13.60	1x10 <sup>12</sup>	+0.00	0%	7%	-0.011	-1%	+0.05	+4%	7.86

## VI. Analysis and Discussion

The purpose of this study was to investigate the effect of displacement damage on the drain ( $I_{ds}$ ) and gate leakage ( $I_{gs}$ ) current in AlGaN/GaN HFETs. Neutrons were primarily used as the irradiation source to ensure that displacement effects dominate the radiation response. Electron irradiation results were also analyzed to see if the radiation type would substantially change the observed effects. Temperature dependence was used to gain insight into the nature of the defect charge and type. Capacitance and gate conductance measurements were used to observe the effect of irradiation on the threshold voltage of 2DEG formation. The effects of passivation on post-irradiation response were also observed.

The  $I_{gs}$  and  $I_{ds}$  measurements provide key insights into the nature of radiation damage to the heterojunction following irradiation. There are three pertinent results regarding the radiation damage. One is that the basic mechanisms affecting  $I_{ds}$  and  $I_{gs}$  are related, owing to their similar formation and how the current saturates after an initial irradiation. Another is that the increase in  $I_{gs}$  and  $I_{ds}$  at  $\sim 85\text{K}$  is opposite of that observed when the device is irradiated at room temperature [55]. Lastly, the observed changes to the gate leakage current are due to changes in the trap density that increase the trap-assisted tunneling current through the gate in the temperature range of 80 to 300K.

The increase in  $I_{gs}$  immediately after irradiation and the persistence of the increase after a RT anneal, as in Figure 73, demonstrates that neutron and electron elastic collisions form point defects within the AlGaN that do not anneal at elevated temperatures. The explanation for this effect in terms of the theory and TAT model are presented in Section 6.2. In Figure 73 the pre-irradiation, post-irradiation, and post-

anneal  $I_{gs}$ -T for all six unpassivated and passivated HFETs from neutron experiment #2 are separately averaged.

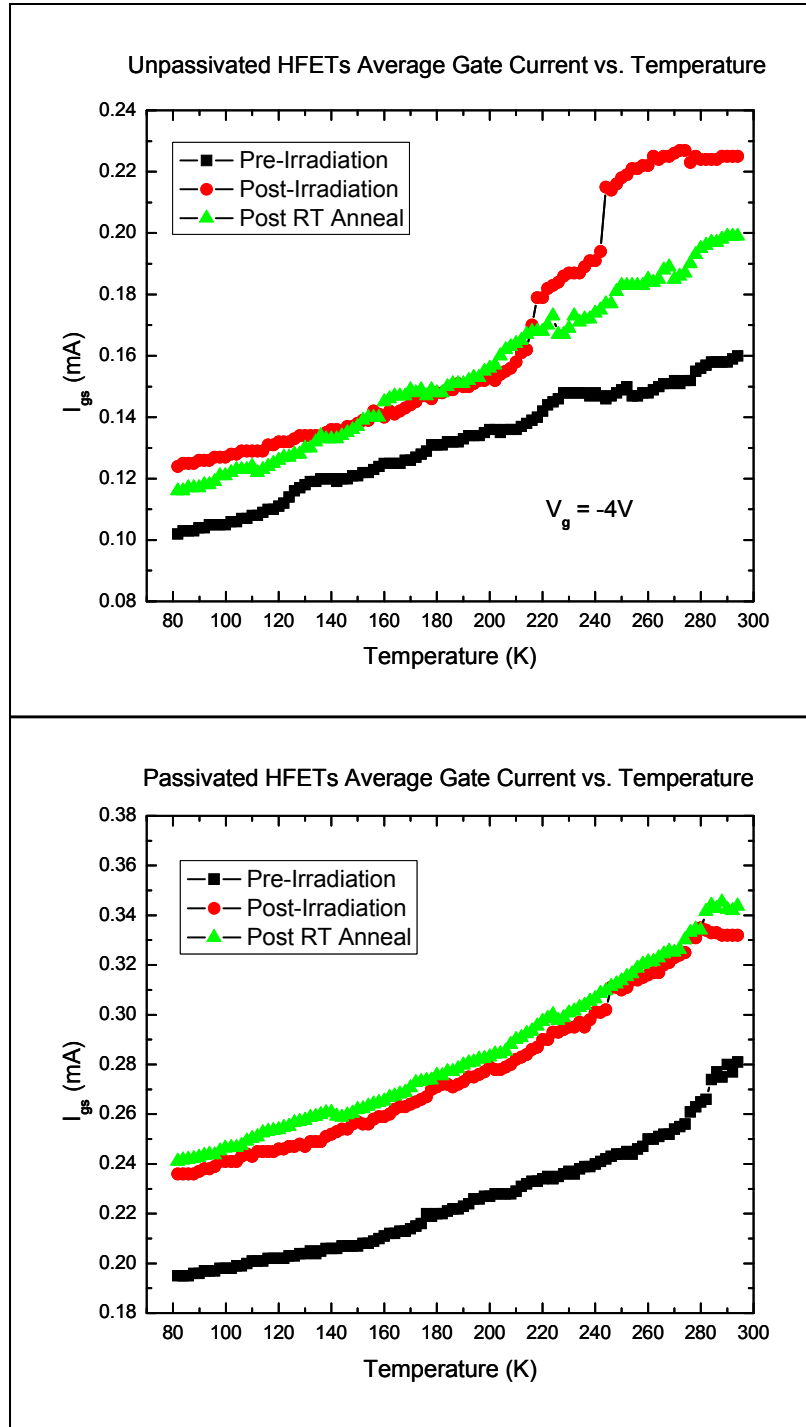


Figure 73. Average  $I_{gs}$ -T for all six unpassivated and passivated HFETs with  $V_{gs} = -4$  V. Data from pre-irradiation, post-irradiation and after a four-week RT anneal measurements is shown.

The increase in  $I_{ds}$  following irradiation at 80 K, as in Figure 74, that decreases at 300 K, as in Figure 75, indicates that temperature affects either the defect's location or type. These defects also have their origin within the AlGaN layer. At RT these defects, or complexes formed from defects, have sufficient thermal energy to migrate under the influence of the intrinsic piezo-electric field at RT to the interface. There they act as charged defects on or near the AlGaN-GaN interface. These defects reduce mobility in the 2DEG and hence reduce the drain-to-source current. These conclusions are supported by analysis in terms of the drain current model in Section 6.1.

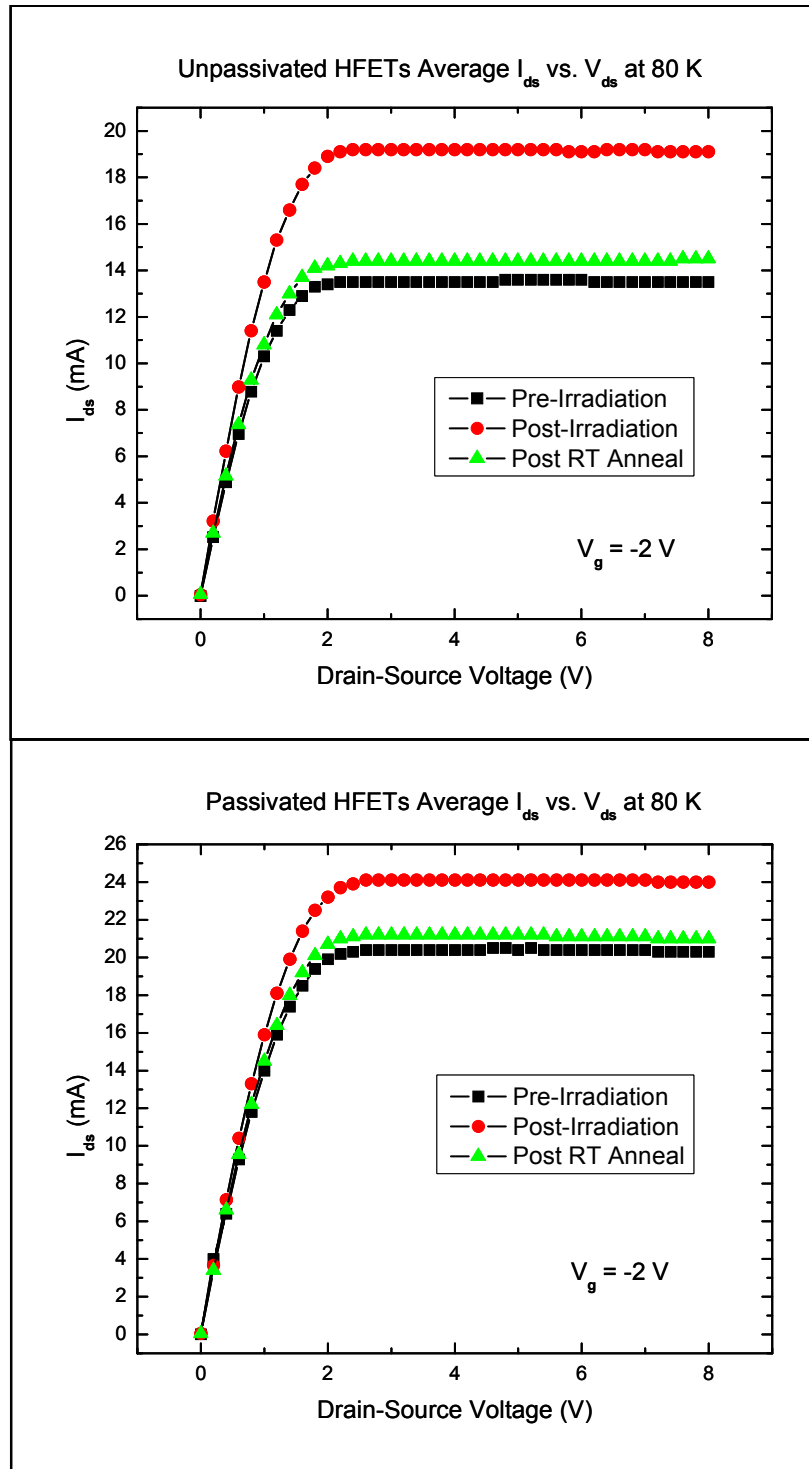


Figure 74. Average  $I_{ds}$ - $V_{ds}$  for all six unpassivated and passivated HFETs at 80 K with  $V_{gs} = -2$  V. Data from pre-irradiation, post-irradiation and after a four-week RT anneal measurements is shown.



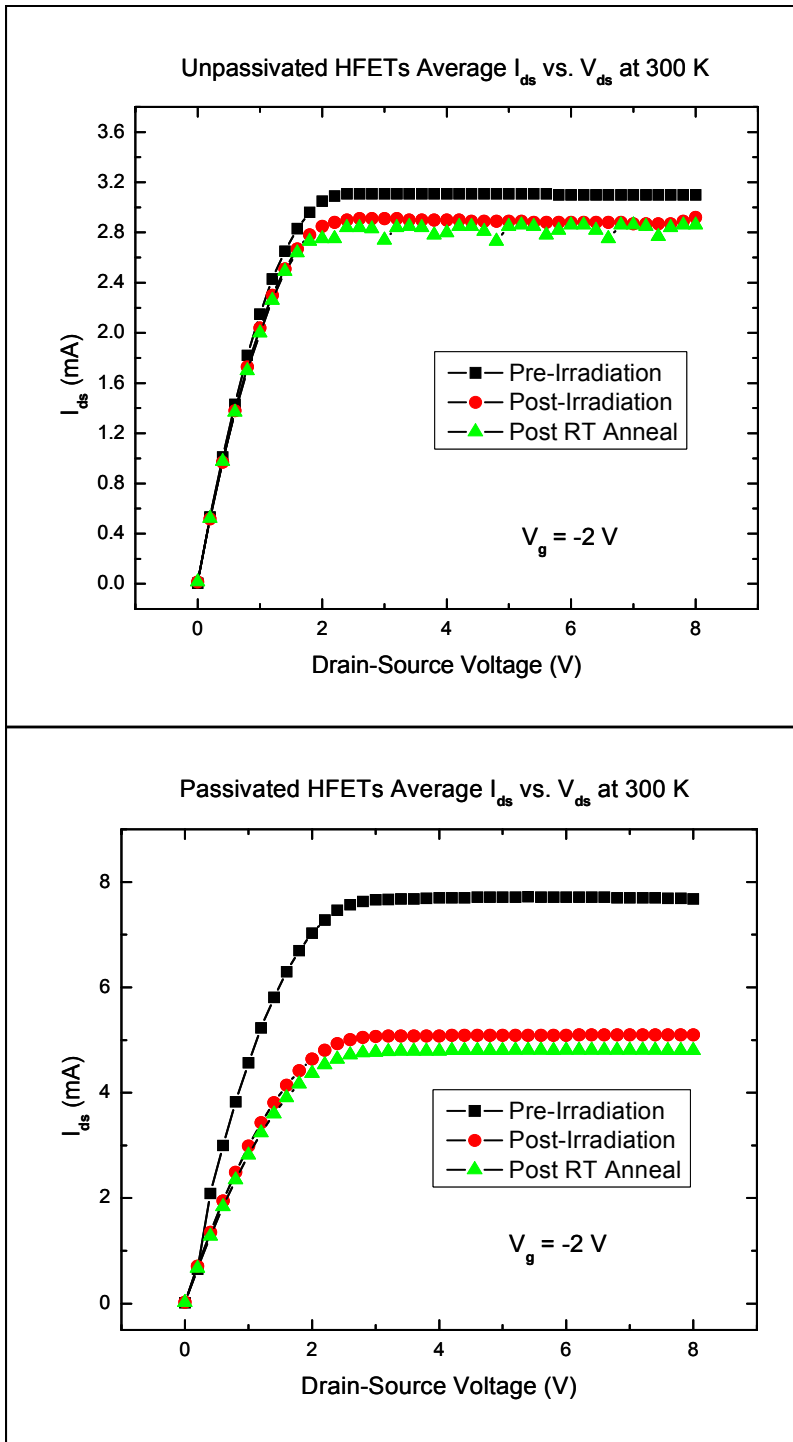


Figure 75. Average  $I_{ds}$ - $V_{ds}$  for all six unpassivated and passivated HFETs at 300 K with  $V_{gs} = -2$  V. Data from pre-irradiation, post-irradiation and after a four-week RT anneal measurements is shown.

Electron-hole pairs are created in the AlGaN layer during irradiation. In the case of electron irradiation, 0.45 MeV electrons interact with AlGaN through ionization and elastic collisions with the atoms. In the case of neutron irradiation, secondary ionization from charged atoms that are displaced by the energetic neutrons has a similar effect but in denser clusters. The ionization creates electron hole pairs that are moved through the gate by the Coulombic force presented by the electric field. This field is the result of the Schottky junction, the spontaneous piezoelectric force at the interface, and the applied bias. The post-irradiation  $I_{ds}$  increase and the negative threshold voltage shift observed in the C-V measurements both signify that there is an initial increase in positive charge within the AlGaN after irradiation. The increase in  $I_{ds}$  after irradiation can be explained by the accumulation of positive charge from ionization in the AlGaN layer provided the positive charge has a low mobility. This is the case at low temperature, which is detailed in Section 6.1 below.

The elastic collisions from electrons and neutrons with the atoms in the AlGaN can form point defects that act as traps through which gate electrons can tunnel. The band structure of the heterostructure (Figure 3) makes this tunneling possible and it has been observed and measured previously [57]. Although the ionization and displacement effects appear to be related, analysis of their relationship is difficult to attribute to a single mechanism. An analysis of the Non-Ionizing Energy Loss (NIEL) of 0.45 MeV electrons and 1 MeV neutrons in AlGaN, and fitting of the gate leakage to a thermionic trap-assisted-tunneling (TAT) model [60] confirms that displacement damage is the source of the increased  $I_{gs}$ . The details of this analysis are in Section 6.2 below.

## 6.1 Irradiation Effect on Drain-to-Source Currents

The principal parameters affecting the HFET drain current are described by the basic drain current model

$$I_{ds} = -qWv(x)n_s(x) \quad (29)$$

where  $q$  is the elementary charge,  $W$  is the gate width,  $v(x)$  is the mobility dependent electron drift velocity, and  $n_s$  is the sheet charge density. Changes to the carrier concentration,  $n_s$ , in the 2DEG and changes to the mobility in the channel region, through  $v(x)$ , are the two parameters affected by displacement damage in the AlGaIn layer. The physics based charge control model developed by Rashmi, *et al.* [18], initially discussed in Section 2.2, applies to carrier concentration in a heterostructure with radiation-induced defects in both the GaN and AlGaIn layers. The 2DEG formed at the AlGaIn-GaN interface has a polarization dependent density that depends on the position of the Fermi level in the well. The thin, 25 nm, AlGaIn layer in this HEFT leads to total depletion, i.e. the gate and junction depletion regions overlap.

The equation for carrier concentration is then

$$n_s(x) = \frac{\varepsilon(x)}{qd} \left( V_{gs} - \varphi_b(x) + \Delta\varphi_c(x) + \frac{qN_d d^2}{2\varepsilon(x)} + \frac{\sigma(x)}{\varepsilon(x)} - \frac{E_F}{q} \right) \quad (30)$$

where  $\varepsilon(x)$  is aluminum molar fraction dependent dielectric constant,  $V_{gs}$  is the gate to source voltage,  $\Delta\varphi_c$  is the conduction band discontinuity, and  $E_F$  is the Fermi level. None of these parameters are expected to change substantially after irradiation. This leaves changes to the Schottky barrier height,  $\varphi_b(x)$ , the intrinsic native doping density in the AlGaIn,  $N_d$ , and the total sheet charge density,  $\sigma(x)$ , induced by both the piezoelectric

field and the field resulting from post-irradiation trapped charge, as potentially important contributors to changes in the carrier concentration after irradiation [3].

The height of the Schottky barrier between the AlGaN layer and the gate metal in a device is determined by the aluminum content of the AlGaN. It is likely that irradiation produces defects that act as trapping sites allowing for TAT by electrons and hence a virtual lowering of the barrier height. This is supported by the persistent increase in the gate leakage current after irradiation as discussed in Section 6.2. However, the increased  $I_{gs}$  is not sufficient to account for the total increase in  $I_{ds}$  at 80 K.

Increases to the doping concentration,  $N_d$ , in the AlGaN layer after irradiation can also result in increases to  $I_{ds}$ . The HFETs under investigation have an as-grown n-type defect doping and radiation induced donor defects have been observed for electron irradiated GaN [53], but were persistent to temperatures above 300 K. No such measurements exist for AlGaN.

Increased sheet charge density,  $\sigma(x)$ , following irradiation could only be the result of increased charge within the AlGaN layer. This charge would change the field in the 2DEG quantum well affecting the carrier concentration through a negative threshold voltage shift. A plausible explanation for the increased charge following neutron irradiation case is that neutron induced point defects trap positive charge in the AlGaN layer. This charge produces the field that increases  $I_{ds}$  at 80 K as in Figure 74. Furthermore, these point defects also act as trapping centers that increase  $I_{gs}$  as in Figure 73. This, however, does not address the decrease in  $I_{ds}$  at elevated temperatures (~300 K), as in Figure 75 since it would require the defects to anneal at the elevated temperature, in conflict with the persistence of  $I_{gs}$ .

At 85 K, this trapping of holes in the AlGaN layer is reasonable since the hole mobility is one-hundredth that of the electron extrapolated from the near RT data by T. Mnatsakanov, *et al.* [68]. Furthermore, the electron current is enhanced by TAT as discussed in Section 6.3. Finally, added positive charge would produce a field that increases  $I_{ds}$  at 85 K as in Figures 30, 46, and 54.

The carrier concentration in the 2DEG under the total depletion approximation in terms of the threshold voltage  $V_{TH}$  is:

$$n_s = \frac{\varepsilon(x)}{qd} \left( V_{gs} - V_{TH}(x) - \frac{E_F}{q} \right) \quad (31)$$

where  $\varepsilon(x)$  is Al mole fraction dependent dielectric constant,  $V_{gs}$  is the gate-to-source voltage,  $d$  is the AlGaN layer thickness, and  $E_F$  is the Fermi level. None of these parameters are expected to change substantially after either electron or neutron irradiation. However,  $V_{TH}$  changes after irradiation as shown, for example, after electron irradiation in Figure 33 from -4.2 to -4.7 volts. Using equation (31) the increased carrier concentration in the 2DEG is

$$\Delta n_s = \frac{\varepsilon(x)}{qd} (-\Delta V_{TH}). \quad (32)$$

For a  $\Delta V_{TH}$  of -0.5 V from Figure 33, the post-irradiation increase in  $n_s$  is  $1.08 \times 10^{12} \text{ cm}^{-2}$ . The ionization from the electrons passing through the AlGaN layer during irradiation is sufficient to produce this many holes remaining from electron-hole pair production. The collisional stopping power for 0.45 MeV electrons in the AlGaN layer calculated from the XGEN code [30] is  $1.4 \text{ MeV-cm}^2/\text{g}$ . A small amount of that,  $10 \text{ eV-cm}^2/\text{g}$ , results in NIEL as discussed in the previous section. What remains goes

into ionization through Compton scattering. The total energy deposited by  $10^{14}$   $0.45 \text{ MeV e}^-/\text{cm}^2$  in the AlGaN layer is then calculated by

$$E_T = \frac{dE}{dx} \rho \phi dA \quad (33)$$

where  $\rho$  is the density of AlGaN,  $6.15 \text{ g/cm}^3$ ,  $\phi$  is the fluence,  $10^{14} \text{ e}^-/\text{cm}^2$ ,  $d$  is the AlGaN layer thickness,  $25 \text{ nm}$ , and  $A$  is the area of the gate,  $10^{-4} \text{ cm}^2$ . The total energy deposited in the AlGaN layer is then calculated as  $E_T = 2.15 \times 10^{11} \text{ eV}$ . The electron-hole production energy in AlGaN is approximately  $10 \text{ eV}$  so there are potentially  $2.15 \times 10^{14} \text{ cm}^{-2}$  electron-hole pairs produced in the AlGaN layer. If  $1/200$  or  $0.5\%$  of the holes produced do not recombine and remain immobile in the AlGaN layer then there is sufficient positive charge to account for the increased carrier concentration. This  $0.5\%$  is a reasonable (and conservative) estimate given that there is a relatively large field ( $\sim 10^8 \text{ V/m}$ ), and the mobility of electrons and holes are significantly different,  $\sim 1000 \text{ cm}^2/\text{V}\cdot\text{s}$  for electrons vs.  $\sim 10 \text{ cm}^2/\text{V}\cdot\text{s}$  for holes in AlGaN, or a two order of magnitude difference. This estimate of hole yield is similar to the development of hole yield in irradiated metal-oxide-semiconductor field effect transistors in [83] and [84].

The incident electrons are also known to create N vacancy defects uniformly throughout the AlGaN layer through elastic collisions [30]. These defects are likely acceptor traps, as measured by [34] since the  $0.45 \text{ MeV}$  electron energy exceeds the minimum displacement energy for N atoms and not Ga. These defects result in N interstitials that form deep electron traps [42] that increase TAT gate currents through the Schottky and AlGaN barriers that add to the drain current. The concept is depicted in Figure 76.

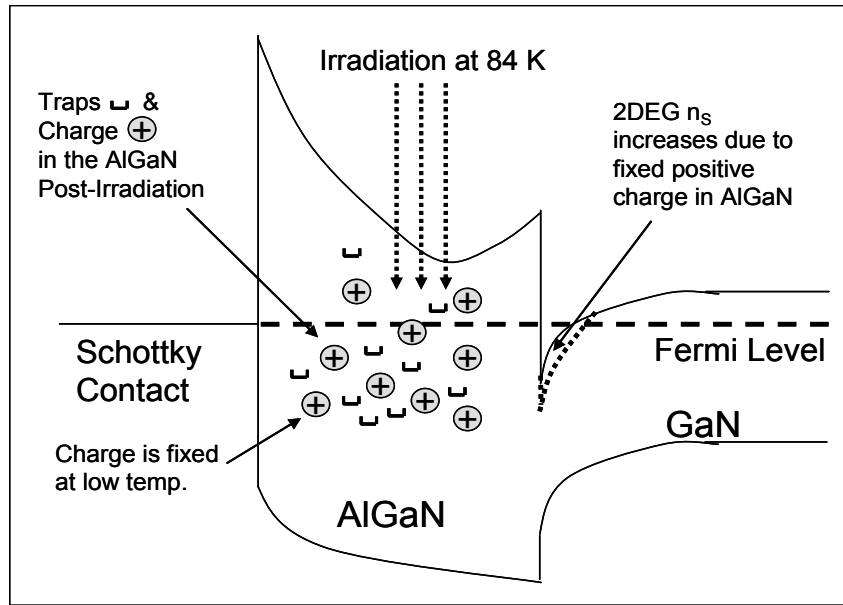


Figure 76. HFET band diagram illustrating the formation of positive charge and traps during neutron and electron irradiation at 84 K.

It is likely that the formation of the N vacancy, the acceptor, and the interstitial trap site are related through a temperature dependent complex precursor similar to that reported by [69]. The complexing results in an acceptor state that increases the local field and results in an as-yet unknown deep trap that increases the TAT across the drain. The damage reaches a threshold below  $10^{14}$   $e^-/\text{cm}^2$  and  $10^{10}$   $\text{n}/\text{cm}^2$  when all precursors have complexed.

Irradiation of the device at 84 K results in an initial increase in  $I_{\text{ds}}$ . The displacement damage that occurs at 84 K is not mobile and the defects remain distributed throughout the AlGaN during the measurements as shown in Figure 76. The defects act as trapping centers for positive charge that increases the charge density in the AlGaN layer. This results in an increase in the 2DEG concentration as the well at the conduction band discontinuity deepens as shown in Figure 76. Since the defects are distributed throughout the AlGaN, they also provide trapping centers that increase  $I_{\text{gs}}$  via TAT. This

same low temperature effect was observed following irradiation by 0.45 MeV electrons as in Figure 30(a) . Additionally, increases in  $I_{ds}$  at room temperature have been reported by [53] following  $^{60}\text{Co}$  gamma irradiations of AlGaIn/GaN HEMTs.

There is a decrease in  $I_{ds}$  at room temperature following irradiation which is in agreement with studies using 1.8 MeV protons [55], [51]. The decrease in  $I_{ds}$  at room temperature can be explained by reduced mobility in the 2DEG channel as described in [55][51][56]. Charged defect centers at the AlGaIn-GaN interface would have an effect on the current by scattering electrons in the quantum well. The current is proportional to mobility ( $\nu(x)/E$ ) as shown in equation (29). Coulombic scattering from charged defect centers in or near the channel region reduces the mobility in the 2DEG channel [51]. This leads to a lower  $I_{ds}$ . The likely source of the Coulombic scattering in the channel region after irradiation that was measured as a decrease in  $I_{ds}$  at RT as in Figure 75 is described below.

As the temperature is increased, the defects produced during irradiation at 80 K become mobile. Since they are positively charged, they drift to the AlGaIn/GaN interface owing to the piezo-electric field in the AlGaIn and create interface traps as shown in Figure 77. The traps reduce the mobility in the channel through coulombic scattering, and decrease  $I_{ds}$  at room temperature. This also explains the return of  $I_{ds}$  to pre-irradiation levels at 80 K as shown in Figure 74. It is slightly higher as the annealing takes time to completely rid the AlGaIn layer of the radiation induced charge. As the period increases from hours to days or longer the current gets closer to the pre-irradiation value.



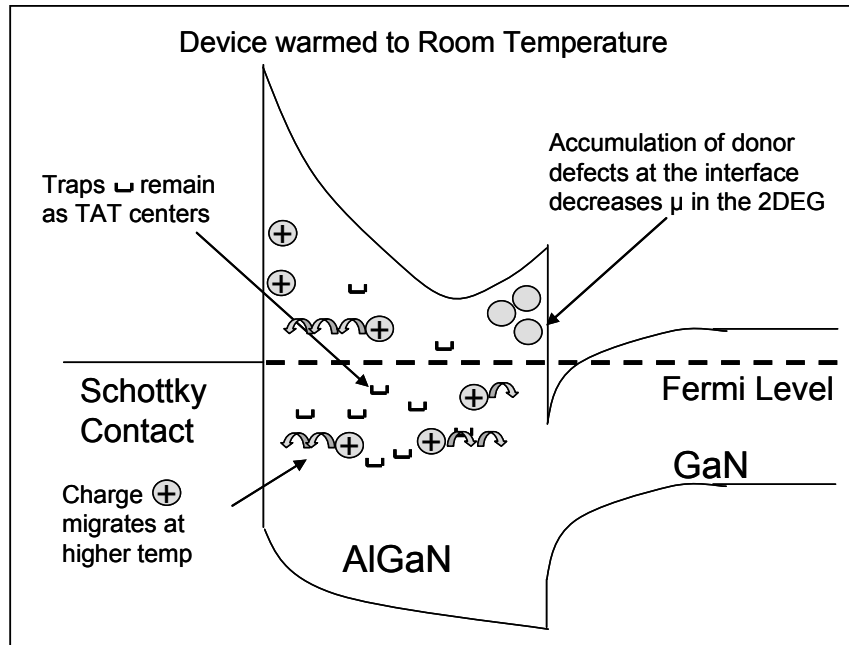


Figure 77. HFET band diagram illustrating the movement of positive charge and the accumulation of donor-like charged defects near the AlGaIn-GaN interface during post-irradiation annealing at room temperature.

Once the temperature is raised and during the subsequent annealing periods, the defects continue to migrate to both the interface at the Schottky junction and the AlGaIn-GaN interface, owing to the presence of the piezo-electric field and thermal energy, as illustrated in Figure 77. This further decreases  $I_{ds}$  at 294 K after long-term annealing as shown in Figure 75.

Charged defect centers at the interface at room temperature are also apparent in the post-anneal C-V data at 294 K. The absence of a threshold voltage shift between the 84 K and 294 K curves rule out latent charges remaining within the AlGaIn, but the C-V stretch-out is evidence of donor-like interface charges. The donor interface traps are ionized at room temperature (below the Fermi level) reducing the mobility, but filled at low temperature. This is consistent with the post-anneal  $I_{ds}$  in both Figures 49 and 50.

## **6.2 Irradiation Effect on Gate Leakage Currents**

An increase in  $I_{gs}$  following irradiation was not previously observed in [55], [51], or [45]. In those studies, an exposure to  $10^{13} \text{ p}^+/\text{cm}^2$  resulted in negligible changes in the gate current and a substantial decrease at higher fluences. In the current research  $I_{gs}$  increased by 10-30% at an exposure of  $3 \times 10^{10} \text{ n}/\text{cm}^2$  with negligible additional increases up to total fluence of  $10^{13} \text{ n}/\text{cm}^2$ . The irradiation at 84 K, as opposed to RT, is likely the reason for the difference and is consistent with the analysis in Section 6.1.

By irradiating at low temperature, the defects form throughout the AlGa<sub>N</sub> layer, and are relatively immobile. As the temperature increases, the charge drifts to the AlGa<sub>N</sub>-Ga<sub>N</sub> interface under the influence of the piezo-electric field. This migration is clearly observed in Figure 73 at around 240 K. At this temperature the gate current increases to a level that is not affected by the RT anneal.

The complex gate structure in these HFET's includes two energy barriers that electrons must traverse in order to form a gate current. A barrier at the AlGa<sub>N</sub>/Ga<sub>N</sub> interface exists owing to the lattice strain and is the primary reason for the existence of the 2DEG. Additionally, a Schottky barrier exists owing to the metal work function of the gate metal. These barriers are present by design, and their function is to reduce the current flow through the gate. Both barriers are only a few nm thick and 0.5-2.0 V high [70]. Thus they are prone to electron tunneling currents when traps are present and within 0.5-2.0 V of the conduction band.

The findings of this work can be explained by a post-irradiation increase in gate leakage current resulting from radiation-induced traps formed in the AlGa<sub>N</sub>, enhancing the TAT currents. Although the nature of the traps is unknown, 0.45 MeV electrons and

1 MeV neutrons have sufficient energy to create traps throughout the AlGa<sub>x</sub>N layer in the unpassivated samples. Owing to electrons having a low NIEL energy; the activation energy of these traps is relatively small. Reference [71] describes native traps in AlGa<sub>x</sub>N with activation energy of 0.38 eV using deep level transient spectroscopy (DLTS) as well as the electron traps described in Chapter 3. It is plausible that the same trap is created in the AlGa<sub>x</sub>N owing to intrinsic precursors in the AlGa<sub>x</sub>N layer and enhanced by the electron radiation.

Previous works support the results of this study. Reference [74] reported that the gate leakage mechanism in AlGa<sub>x</sub>N/GaN (HEMTs) consists of two parallel electron transport processes: TAT and direct tunneling, with the TAT component dominant at low temperatures ( $T < 500\text{K}$ ). Reference [72] also reported that carrier transport across the AlGa<sub>x</sub>N barrier layer is dominated by the tunneling of electrons. Finally, [73] reported a six order of magnitude reduction in gate leakage current from the integration of an oxide region between the gate contact and the Al<sub>x</sub>Ga<sub>1-x</sub>N layer. The TAT current was modeled and fitted to the data with the theoretical description of the model in Section 3.5, the optimization algorithm in Section 4.4 and the results of fitting the model to the measurements in Section 5.3.

### **Increased Gate Leakage and the TAT Model**

The HFETs showed gate current I-T and I-V behavior that was consistent with trap-assisted tunneling and was fit with success using the TAT model. The TAT model produced a fit to pre-irradiation gate current for all twelve of the HFETs modeled that had R-RMSE values of 3 to 14  $\mu\text{A}$  (Table 11) with temperature-dependent gate currents in the range 50 to 500  $\mu\text{A}$ , as in Figure 35 using the primary parameters  $\varphi_b$ ,  $\varphi_t$ ,  $N_d$ , and

$N_t$ . The pre- and post-irradiation results averaged for the six unpassivated and six passivated HFETs respectively are presented in Table 12.

Table 12. Low Temperature Parametric Changes Following Neutron Irradiation

Parameter	Symbol	Average Pre-irradiation	Average Post-irradiation	Trend
Trap Density	$N_t$	Passivated $5.11 \times 10^{15} \text{ cm}^{-3}$	Passivated $7.56 \times 10^{15} \text{ cm}^{-3}$	↑ +48%
		Unpassivated $4.97 \times 10^{15} \text{ cm}^{-3}$	Unpassivated $7.03 \times 10^{15} \text{ cm}^{-3}$	+41%
Trap Energy	$\phi_t$	Passivated 0.873 V	Passivated 0.888 V	↑ +2%
		Unpassivated 0.873 V	Unpassivated 0.889 V	+2%
Donor Density	$N_d$	Passivated $5.11 \times 10^{18} \text{ cm}^{-3}$	Passivated $5.19 \times 10^{18} \text{ cm}^{-3}$	↑ +2%
		Unpassivated $4.26 \times 10^{18} \text{ cm}^{-3}$	Unpassivated $4.29 \times 10^{18} \text{ cm}^{-3}$	+1%
Schottky Barrier	$\phi_b$	Passivated 1.227 V	Passivated 1.307 V	↑ +7%
		Unpassivated 1.307 V	Unpassivated 1.330 V	+2%

In order to determine which of the four parameters are affected by radiation a number of devices were measured and analyzed. Figure 69 in Section 5.3 presents the results of each parameter adjusted individually to fit the post-irradiation data while keeping the other three parameters constant. Increasing  $N_t$ ,  $N_d$ , and  $\phi_t$  provide a reasonable fit to the post-irradiation data while adjusting  $\phi_b$  does not. The effect of changing each parameter on the TAT current calculation is determined from their effect on the TAT integral, equation (27) of Section 4.4.

The TAT current is directly proportional to the trap density,  $N_t$ , as is evident in equation (27). In the fitting to post-irradiation results it is the dominant of the four parameters in fitting the post-irradiation data to the model. It increased for all the HFETs as the post-irradiation current data increased in all cases and the percentage increase in  $N_t$  was an order of magnitude higher than the other parameters as seen for the averages in Table 12.

Changes to the donor density also have a nearly linear effect on the current in the temperature range 80 to 300 K but the relationship is not direct nor as strong as the relationship with  $N_t$ . An increase in the donor density affects the TAT current indirectly through the electric field in the AlGaIn layer. The electric field is linearly dependent on the donor density as in equation (23). The TAT current, equation (27), is inversely proportional to the field but that is not the only dependence on the donor density. The Fermi-Dirac function and the upper limit of integration in the TAT integral are dependent on the Schottky barrier height, as in equations (17) and (22). The height of the Schottky barrier is lowered proportionally by the square root of the field, as in equation (25). As the field in the AlGaIn layer increases the TAT current increases. The result is a nearly linear increase of the TAT current with donor concentration borne out by trials using the model and the optimization algorithm.

Likewise, changes to the trap energy level have a nearly linear effect on the TAT current in the temperature range of this study. The TAT current is proportional to the trap energy level in a complex manner via the tunneling probabilities, the trap energy dependent rate constant, and the lower limit of integration of the TAT integral. Increasing the trap energy level, i.e. moving the trap further from the conduction band, increases the

TAT current as it is easier for lower energy electrons from the metal Fermi level to reach the trap level. This is also borne out in tests with the TAT model and optimization algorithm.

Changes to the Schottky barrier height are more difficult to relate to the changes in the TAT current through the temperature range. Lowering the Schottky barrier height allows electrons to more easily tunnel but the effect is not linear with temperature. A lower barrier allows electrons at a lower temperature to tunnel across the barrier without affecting the higher temperature tunneling which is limited by the other parameters.

The result of the analysis of the data and the model is that the increase in gate leakage current after electron and neutron irradiation is primarily due to an increase in trap density in the AlGa<sub>N</sub> layer. The increase in  $N_t$  dominated the fit of the model to the measured increase in current, both on average as in Table 12 and for each of the 12 HFETs irradiated as in Table 11.

### ***6.3 Irradiation Effect on Capacitance***

Incident electrons and neutrons cause ionizations that create electron-hole pairs in the AlGa<sub>N</sub> during irradiation at low temperature. Due to the large intrinsic electric field in the AlGa<sub>N</sub> and the higher electron mobility, the ionized electrons exit the heterostructure leaving behind a stationary and trapped positive charge in the AlGa<sub>N</sub> along the interface between the AlGa<sub>N</sub> and GaN as described in Section 6.1. This trapped positive charge in the AlGa<sub>N</sub> layer causes an increase in carrier concentration in the 2DEG and hence a negative increase in the threshold voltage as shown in Figure 78. The effect is more pronounced in unpassivated versus SiN passivated HFETs.

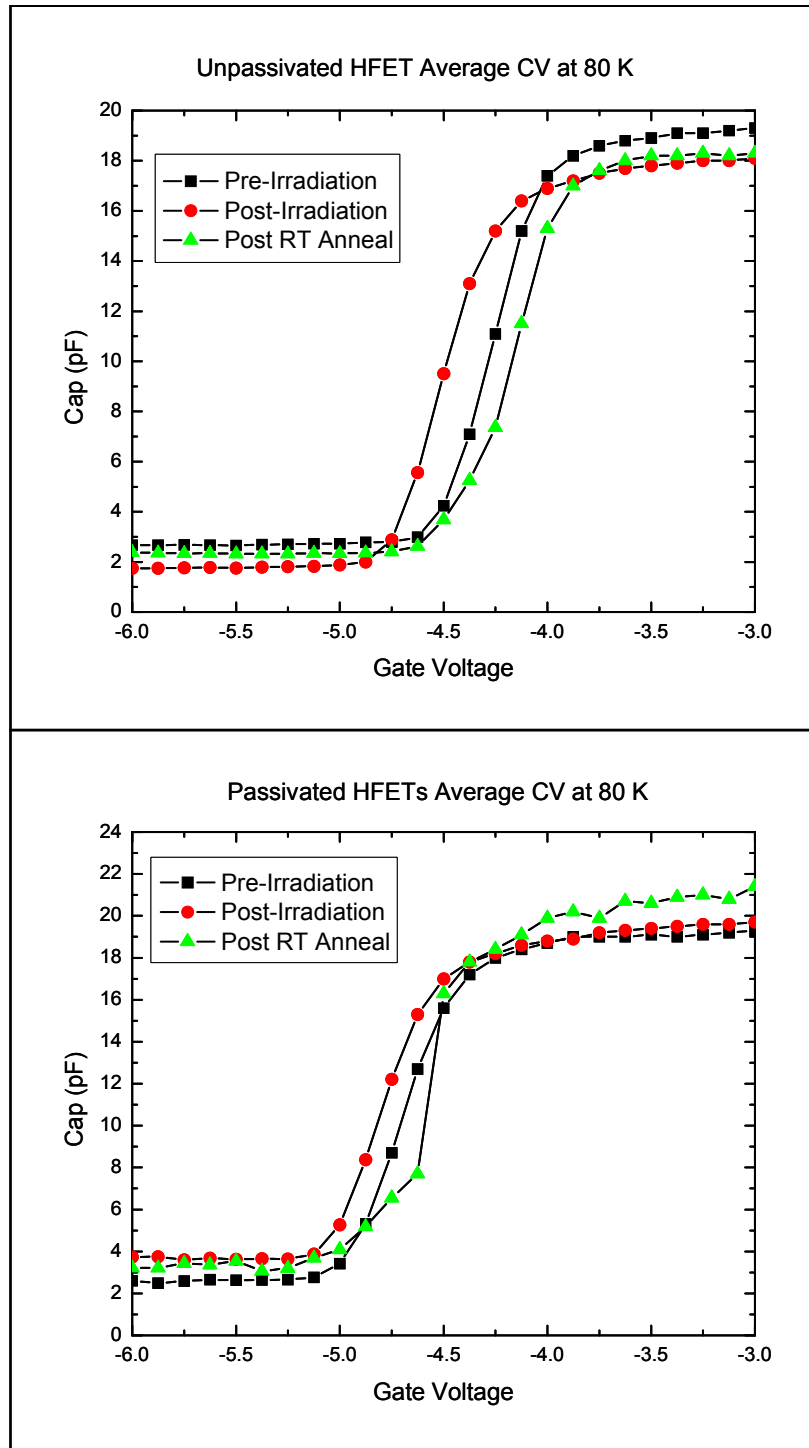


Figure 78. Average  $C-V_g$  for all six unpassivated HFETs and all six passivated HFETs at 80 K with  $V_{ds} = 0$  V. Data from pre-irradiation, post-irradiation and after a four-week RT anneal measurements is shown.

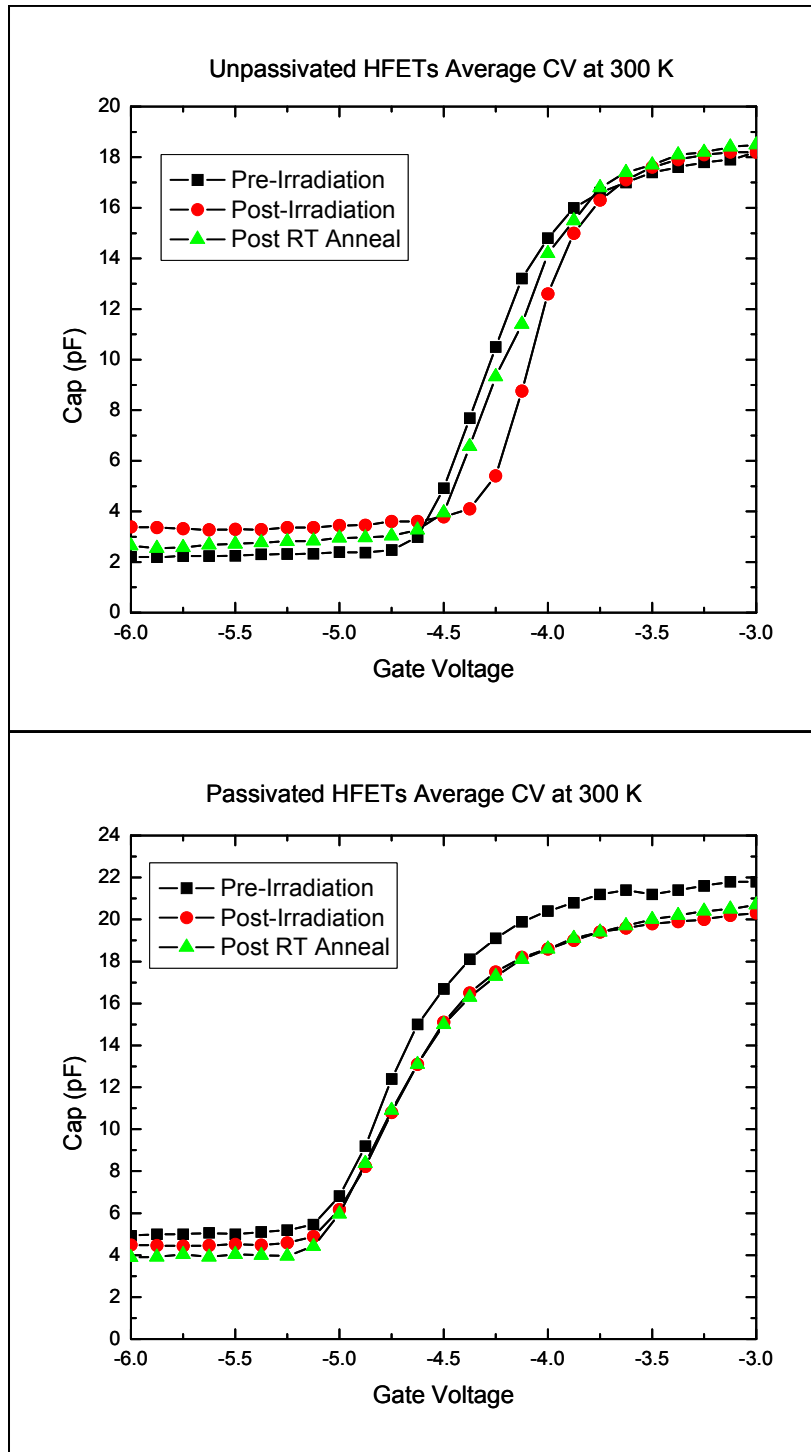


Figure 79. Average  $C-V_g$  for all six unpassivated and passivated HFETs at 300 K with  $V_{ds} = 0$  V. Data from pre-irradiation, post-irradiation and after a four-week RT anneal measurements is shown.



Upon warming to room temperature, the threshold voltage shift changes to a shift in the positive direction as shown in Figure 79. This is due to the movement of charge as described in Section 6.1. Again the effect is diminished in passivated HFETs. Both the 80 K and 300 K threshold voltages return toward the pre-irradiation values after four-week RT annealing.

As the temperature is increased, the defects produced during irradiation at 80 K become mobile. They drift and are neutralized as they move to the two interfaces. The threshold voltage then returns to its pre-irradiation value.

#### ***6.4 Device Design to Mitigate Radiation Effects***

The increase of drain currents at low temperature after irradiation can lead to inadvertent device turn on. Decreased drain currents at room temperature could cause inadvertent device turn off. Increased gate currents throughout the temperature range could lead to device failure. Device design for employment in a radiation environment should attempt to mitigate these effects.

Passivation decreases the changes in drain and gate currents and threshold voltages as shown in the unpassivated/passivated comparison figures presented earlier in this chapter. Passivation generally improves device operation in a non-irradiation environment via higher carrier concentration in the 2DEG but it also causes increased gate leakage currents[93]. Threshold voltage shifts were less severe at low temperature as in Figure 74. Passivated HFETs returned more readily to pre-irradiation drain current characteristics throughout the temperature range after room temperature annealing as in Figure 74. However, the room temperature decrease in drain current was more severe as in Figure 75. Although the increase in gate current after irradiation was similar in

passivated HFETs, the additional increase after the movement of mobilized charge as the temperature was raised above 200 K was less noticeable in passivated HFETs as in Figure 73. Generally, passivation increases not just HFET pre-irradiation but also post-irradiation performance.

The low temperature increase in drain current vs. the high temperature decrease could be an important issue for HFETs operating in a large temperature range. HFET system designers need to be aware of the proposed operating temperature range if the HFET will function in a radiation environment to determine the relative effect of irradiation on device operation. For example, passivation would aid in maintaining pre-irradiation drain currents after radiation exposure at 80 K but may exacerbate drain current decrease at 300 K. Passivation would prevent the jump in gate current at 240 K after irradiation that may lead to gate failure in an unpassivated HFET.

The addition of field plates [90] and thick GaN caps [55] may also aid in reducing radiation-induced degradation. Although not experimentally tested in this research, these design additions have improved the performance of AlGaN/GaN HFETs. These may improve the radiation response via simple shielding of the AlGaN layer from irradiation as well as by their effect on charge build up and motion within the AlGaN layer. However the thickness of shielding necessary to stop the 1 MeV neutron and 0.45 MeV electron radiation would be greater than the structures proposed in [55] and [90]. Chapter 7 contains some recommendations on additional experimentation to determine the validity of different design considerations in mitigating radiation degradation.

## VII. Conclusions

The AlGaN/GaN HFETs studied in this research continued to function properly after radiation fluences up to either  $10^{14}$  0.45 MeV electrons/cm<sup>2</sup> or  $10^{13}$  1.0 MeV(eq) neutrons/cm<sup>2</sup>. However there were noticeable radiation effects on both the drain and gate leakage current. These changes to the currents were temperature dependent in the range of 80 to 300 K and varied with room temperature annealing. The drain current model was applied to the measured changes in the drain current and provided insight into the post-irradiation defect type and the mechanism of drain current changes. Likewise, the trap-assisted tunneling model was applied to the measured changes in the gate leakage current and provided insight into the radiation induced changes to the parameters affecting the gate current in the gate region.

### Summary of Findings

AlGaN/GaN HFETs were susceptible to threshold voltage shifts and changes to drain currents after irradiation. After electron and neutron irradiation applied at ~80 K, measurement of the drain current at this temperature without warming showed an increase in the current that saturated after  $10^{13}$  electrons/cm<sup>2</sup> or  $10^{10}$  neutrons/cm<sup>2</sup>. Measurement of the capacitance and gate conductance through the gate under the same conditions, low-temperature irradiation and low-temperature measurement without warming showed a negative threshold voltage shift.

This low-temperature increase in drain current and negative threshold voltage shift after irradiation is attributed to positive charge in the AlGaN layer. Both electron and neutron irradiation cause electron-hole pair production through ionization in the AlGaN layer. The lower mobility of holes (electron mobility is five times greater) and the

high electric fields in the AlGa<sub>N</sub> layer cause the electrons to be swept out, leaving holes behind. The low temperatures limit the movement of these holes and hence positive charge is fixed in the AlGa<sub>N</sub> layer. The positive charge results in a threshold voltage shift, an increase in carrier concentration in the 2DEG and therefore increased drain currents at identical drain-to-source and gate-to-source voltages compared to those currents measured prior to irradiation.

This increased drain current at low temperature only persists if the HFETs are kept at low temperature. As the temperature is raised toward room temperature, the holes gain sufficient kinetic energy to migrate under the influence of the piezoelectric field in the gate region. Some recombine with electrons and some result in charged defects at the interface. An HFET that has been warmed to room temperature after 80 K irradiation and is then lowered in temperature back to 80 K no longer demonstrates an increased drain current and threshold voltage shift. The positive charge that caused the threshold voltage shift has annealed.

Measurement at room temperature after low temperature irradiation shows a slightly positive threshold voltage shift (much lower than the negative shift at low temperature) and a decrease in drain current. The positive charges that caused the low temperature increase become mobile as the temperature increases and result in charged defects along the AlGa<sub>N</sub>-Ga<sub>N</sub> interface. These charged defects decrease the mobility in the 2DEG and hence decrease the current. The charge state of these defects is temperature dependent. These defects are uncharged at low temperature and therefore do not decrease the mobility at 80 K, but are charged and reduce the mobility of the 2DEG

electrons at room temperature. This drain current reduction does not anneal at room temperature as these defects are persistent.

AlGaIn/GaN HFET gate leakage currents increase after low temperature irradiation. The increased gate current again saturates with additional electron and neutron irradiation above  $10^{13}$  electrons/cm<sup>2</sup> or  $10^{10}$  neutrons/cm<sup>2</sup>. Below  $10^{10}$  neutrons/cm<sup>2</sup> the increase was not observed. The increase was present throughout the temperature range of 80 K, the irradiation temperature, up through 300 K. In some HFETs there was an additional increase in the gate current as the temperature was raised from 200 to 260 K which was attributed to the movement of defects as their kinetic energy increased similar to the increased mobility of positive charge described previously.

The increased gate leakage current can only be attributed to additional trap-assisted tunneling based on the functional increase of the current with the increase in temperature, the energy levels through the gate region, and the effect of radiation on the AlGaIn gate. The increase in gate leakage current was persistent after weeks of annealing at room temperature. The radiation-induced defects that result in increased trap-assisted tunneling are fixed in the AlGaIn layer. The saturation after relatively low levels of irradiation indicates that the defects are based on the complexing of gallium, nitrogen, and/or aluminum defects with an impurity element in the AlGaIn. The impurity is of limited quantity in the AlGaIn and therefore limits the growth of additional defects. Oxygen is the most likely source of this complexing behavior [91].

The source of the increase in the gate leakage current was modeled using the TAT model. An optimization algorithm was applied to the TAT model to determine which of

the four variables of the model was the source of increased TAT. The four parameters were the Schottky barrier height  $\phi_b$ , the trap level  $\phi_t$ , the donor concentration in the AlGaN layer  $N_d$ , and the trap concentration  $N_t$ . Application of the TAT model to pre-irradiation data showed that its output closely matched the pre-irradiation gate current. Application of the model to post-irradiation vs. pre-irradiation data showed that the dominant parameter that conformed to the increased gate current is the trap concentration  $N_t$ . Following irradiation,  $N_t$  increased consistently in order to match the model to the experiment.

The effect of SiN passivation on these radiation-induced changes was also observed. Passivated HFETs have higher drain currents and threshold voltages and higher gate leakage currents prior to irradiation. Passivated HFETs had a smaller percentage increase in drain current at low temperature but a larger percentage decrease at room temperature. The percentage threshold voltage shifts were smaller in the passivated HFETs. The effect of SiN passivation in the gate region, which is higher electric fields due to the neutralization of negative charges at the AlGaN surface, is apparent in these results. Passivation increases the radiation hardness of these devices for radiation expected in the space environment.

## **Proposed Experimental Directions**

Additional electron irradiation and measurements throughout the same temperature range applied to the neutron irradiated HFETs in this research need to be completed. Electron irradiation data was limited to current measurements at low temperature and limited C-V measurements. An additional series of electron irradiations and measurements over the temperature range 80 to 300 K would allow comparison with

the neutron irradiation results. The electron energy level also should be varied to compare the effect on the HFET electrical characteristics from different irradiation energies. At lower electron energies the minimum displacement energy for the AlGa<sub>N</sub> component elements, Al, N, and Ga, can be reached. This allows the study of selective sub-lattice damage. Variation of the fluence could be used to determine the minimum electron fluence at different energies that causes the onset of device degradation. At the other end, higher fluence levels could help determine the maximum electron irradiation the devices can withstand at low temperature without permanent failure.

The examination of Schottky contacts on AlGa<sub>N</sub> would help in determining the charged carrier transport through the contact as opposed to transport through the AlGa<sub>N</sub> layer. Although device level testing provides great insight into total system behavior, some more preliminary device work would add value add to the HFET results. These test structures would also help in determining material baselines as well as device behaviors.

Irradiation testing of different HFET designs for comparison to the results presented in this study is warranted to determine the optimum design characteristics necessary to minimize radiation effects. Device design considerations include passivation techniques, heterostructure layering, varying metallization for Schottky and ohmic contact deposition, the use of field plates, and growth techniques for the Ga<sub>N</sub> and AlGa<sub>N</sub> layers. The HFETs in this study were chosen for simplicity, reliability, and repeatability, not radiation hardness or optimization of operating characteristics. The comparison of the post-irradiation behavior of these devices with HFETs of different designs but irradiated and measured in the same manner could lead to insights into the source of changes in the post-irradiation characteristics. For example, the effect of the

introduction of additional oxygen into the AlGaN layer could be explored through electrical measurements and spectroscopy.

Future research efforts need to address the nature of the defects within the AlGaN and passivation layer. Determining the type, charge state, and motion of the defects will require spectroscopic techniques that can probe into the gate region to the boundary. A combination of cathodoluminescence (CL), electron paramagnetic resonance spectroscopy (EPR), and positron annihilation spectroscopy (PAS) using irradiated as-grown AlGaN and GaN samples may be able to address this issue and is further warranted by this study. Defects caused by neutrons and electrons at different energies and fluences still require type identification. The defect energy level, charge state, and type are all important parameters for fully understanding the observed effect on the electrical characteristics in HFETs.

Further research into the effects of radiation on HFET performance and the ultimate effects on circuitry requires that sufficient physics-based models be developed to include in the effect of irradiation on the simulation system. Work is needed in modeling radiation effects, especially the effect on gate leakage current, as part of a complete package of device and circuit level simulation. The set of software tools in the Sentaurus [87] simulation software package from Synopsys may be suitable for this purpose.



## Bibliography

- [1] U. Mishra, P. Parikh, and Y.-F. Wu, "AlGaIn/GaN HEMTs – An Overview of Device Operation and Applications," *Proceedings of the IEEE*, vol. 90, no. 6, pp. 1022-1031, June 2002.
- [2] A. Ionascut-Nedelescu, C. Carlone, A. Houdayer, H. J. von Bardeleben, J.-L. Cantin, S. Raymond, "Radiation Hardness of Gallium Nitride", *IEEE Transactions on Nuclear Science*, vol. 49, no. 6, pp. 2733-2738, December 2002.
- [3] J. W. McClory, J. C. Petrosky, J. M. Sattler, T. A. Jarzen, "An Analysis of the Effects of Low-Energy Electron Irradiation of AlGaIn/GaN HFETs," *IEEE Transactions on Nuclear Science*, vol. 54, no. 6, pp. 1946-1952, Dec. 2007.
- [4] J. W. McClory, J. C. Petrosky, "Temperature Dependent Electrical Characteristics of Neutron Irradiated AlGaIn/GaN HFETs," *IEEE Transactions on Nuclear Science*, vol. 54, no. 6, pp. 1969-1974, Dec. 2007.
- [5] T. E. Gray, J. W. McClory, J. C. Petrosky, T. A. Uhlman, "Trap-assisted Tunneling Induced Currents in Neutron Irradiated AlGaIn/GaN HFETs," accepted by *IEEE Transactions on Nuclear Science* and currently in revision.
- [6] A. Chow, T. P. Ghezzo. SiC power devices. in *III-Nitride, SiC, and Diamond Materials for Electronic Devices*. Eds. Gaskill D.K, Brandt C.D. and Nemanich R.J., *Material Research Society Symposium Proceedings*, Pittsburgh, PA., vol. 423, pp. 69-73, 1996.
- [7] C. H. Oxley, M. J. Uren, A. Coates, D. G. Hayes, "On the Temperature and Carrier Density Dependence of Electron Saturation Velocity in an AlGaIn/GaN HEMT", *IEEE Transactions on Electron Devices*, vol. 53, no. 3, pp. 565-567, March 2006.
- [8] V. Bougrov, M. Levinshtein, S. Rumyantsev, and A. Zubrilov, in *Properties of Advanced Semiconductor Materials*, edited by M. E. Levinshtein, S. L. Rumyantsev, and M. S. Shur , Wiley, New York, 2001, pp. 1 and 31.
- [9] N. W. Ashcroft, A. R. Denton, "Vegard's Law", *Physical Review A (Atomic, Molecular, and Optical Physics)*, vol. 43, no. 6, March 15, pp. 3161-3164, 1991.
- [10] C. Y. Fong, W. Weber, J. C. Phillips, "Violation of Vegard's law in covalent semiconductor alloys", *Physical. Review B*, vol. 14, pp. 5387 – 5391, 1976.
- [11] T. J. Ochalski, B. Gil, P. Lefebvre, N. Grandjean, M. Leroux, J. Massies, S. Nakamura, and H. Morkoc. "Photorefectance investigations of the bowing

- parameter in AlGa<sub>N</sub> alloys lattice-matched to GaN," *Applied Physics. Letters* vol. 74, 3353, 1999.
- [12] W. Shan, J. W. Ager III, K. M. Yu, W. Walukiewicz, E. E. Haller, M. C. Martin, W. R. McKinney, and W. Yang. "Dependence of the fundamental band gap of Al<sub>x</sub>Ga<sub>1-x</sub>N on alloy composition and pressure," *Journal of Applied Physics* Vol. 85, 8505, 1999.
- [13] R. T. Kemerley, H. B. Wallace, and M. N. Yoder. "Impact of wide bandgap microwave devices on DoD systems," *Proceedings of the IEEE 90*, 1059, 2002.
- [14] L. Hsu, W. Walukiewicz, "Electron mobility in Al<sub>x</sub>Ga<sub>1-x</sub>N/GaN heterostructures," *Physical Review B*, vol. 56, no. 3, pp. 1520, 1997.
- [15] H. Morkoc, *et al.*, "GaN-based modulation doped FETs and UV detectors," *Solid State Electronics*, vol. 46, pp. 157-202, 2002.
- [16] O. Ambacher, *et al.*, "Two-dimensional electron gases induced by spontaneous and piezoelectric polarization charges in N- and Ga-face AlGa<sub>N</sub>/Ga<sub>N</sub> heterostructures," *Journal of Applied Physics*, vol. 85, no. 6, pp. 3222-3333, 1999.
- [17] I. P. Smorchova, *et al.*, "Polarization-induced charge and electron mobility in AlGa<sub>N</sub>/Ga<sub>N</sub> heterostructures grown by plasma-assisted molecular-beam epitaxy," *Journal of Applied Physics*, vol. 86, no. 8, pp.4520-4526, 1999.
- [18] Rashmi, A. Kranti, S. Haldar, R. S. Gupta "An accurate charge control model for spontaneous and piezoelectric polarization dependent two-dimensional electron gas sheet charge density of lattice-mismatched AlGa<sub>N</sub>/Ga<sub>N</sub> HEMTs", *Solid State Electronics*, vol. 46, pp. 621-630, 2002.
- [19] W. Walukiewicz, *et al.*, "Electron mobility and free-carrier absorption in GaAs: Determination of the compensation ratio," *Journal of Applied Physics*, vol. 50, no. 2, pp. 899-908, 1979.
- [20] J. P. Ibbetson, *et al.*, "Polarization effects, surface states, and the source of electrons in AlGa<sub>N</sub>/Ga<sub>N</sub> heterostructure field effect transistors", *Applied Physics Letters*, vol. 77, no. 2, pp. 250-252, July 2000.
- [21] R. Vetury, *et al.*, "Polarization induced 2DEG in MBE grown AlGa<sub>N</sub>/Ga<sub>N</sub> HFETs: On the origin, DC and RF characterization," *Proc. Materials Research Soc. Symp.*, vol. 622, p. T2.5.
- [22] R. Vetury, N. Q. Zhang, S. Keller, U. K. Mishra, "The Impact of Surface States on the DC and RF Characteristics of AlGa<sub>N</sub>/Ga<sub>N</sub> HFETs", *IEEE Transactions on Electron Devices*, vol 48, no. 3, pp. 560-566, March 2001.

- [23] B. M. Green, *et al.*, “The effect of surface passivation on the microwave characteristics of undoped AlGaIn/GaN HEMT’s,” *IEEE Electron Device Letters*, vol. 21, June 2000.
- [24] P. Kordos, P. Kudela, D. Gregusova, D. Donoval, “ The effect of passivation on the performance of AlGaIn/GaN heterostructure field effect transistors”, *Semiconductor Science and Technology*, vol. 21, no. 12, pp. 1592-1596, December 2006.
- [25] L. D. Landau, E. M. Lifschitz,, *The Classical Theory of Fields*, London, 1962.
- [26] J. Nord, *et al.*, “Molecular dynamics study of defect formation in GaN cascades,” *Nuclear Instruments and Methods in Physics Research Section B: Beam Interactions with Materials and Atoms*, vol. 202, pp. 93-99, 2003.
- [27] K. D. Greene, *Electron Paramagnetic Resonance Spectroscopy and Hall Effect Studies of the Effects of Low Energy Electron Irradiation on Gallium Nitride (GaN)*, Air Force Institute of Technology (AU), Wright-Patterson AFB OH, September 2003.
- [28] D. C. Look, *et al.*, “Defect Donor and Acceptor in GaN,” *Physical Review Letters*, vol. 79, no. 12, pp. 2273-2276, 1997.
- [29] D. C. Look, *et al.*, “On the Nitrogen Vacancy in GaN,” *Applied Physics Letters*, vol. 83, no. 17, pp. 3525-3527, 2003.
- [30] Integrated TIGER Series of Coupled Electron/Photon Monte Carlo Transport Codes System, Radiation Safety Information Computational Center, Oak Ridge National Laboratory.
- [31] J. M. Sattler, *An Analysis of the Effects of Low Energy Electron Radiation on AlGaIn/GaN Modulation-Doped Field-Effect Transistors*, Air Force Institute of Technology (AU), Wright-Patterson AFB OH, March 2004.
- [32] ASTM E772(1992), “Standard Practice for Characterizing Neutron Energy Fluence Spectra in Terms of an Equivalent Monoenergetic Fluence for Radiation-Hardness Testing of Electronics”, Approved 15 SEP 1994
- [33] D. C. Look, “Defect-Related Donors, Acceptors, and Traps in GaN,” *Physica Status Solidi B*, vol. 228, no. 1, pp. 293-302, 2001.
- [34] D. C. Look, *et al.*, “Defect Donor and Acceptor in GaN,” *Physical Review Letters*, vol. 79, no. 12, pp. 2273-2276, 1997.

- [35] K. Saarinen, *et al.*, “The influence of Mg doping on the formation of Ga vacancies and negative ions in GaN bulk crystals”, *Applied Physics Letters*, vol. 75, no. 16, pp. 2441-2443, 1999.
- [36] J. Neugebauer, C. G. Van der Walle, “Atomic geometry and electronic structure of native defects in GaN”, *Physical Review B*, vol. 50, no. 11, pp. 8067-8070, 1994.
- [37] K. H. Chow, *et al.*, “Detection of Interstitial Ga in GaN”, *Physical Review Letters*, vol. 85, no. 13, pp. 2761-2764, 2000.
- [38] K. Saarinen, *et al.*, “Ga vacancies in electron irradiated GaN: introduction, stability, and temperature dependence of positron trapping”, *Physica B*, vol. 308-31, pp. 77-80, 2001.
- [39] M. R. Hogsed, *Deep Level Defects in Electron-Irradiated Aluminum Gallium Nitride Grown by Molecular Beam Epitaxy*, Air Force Institute of Technology (AU), Wright-Patterson AFB, OH September 2004 (ADA420816).
- [40] S. A. Goodman, F. D. Auret, M. J. Legodi, B. Beaumont, and P. Gibart. "Characterization of electron-irradiated n-GaN," *Applied Physics Letters*, vol. 78, 3815, 2001.
- [41] Z.-Q. Fang, J. W. Hemsky, D. C. Look, and M. P. Mack. "Electron-irradiation-induced deep level in n-type GaN," *Applied Physics Letters*, vol. 72, 448, 1998.
- [42] M. R. Hogsed, Y. K. Yeo, M. Ahoujia, M. Ryu, J.C. Petrosky, and R. L. Hengehold, “Radiation-induced electron traps in Al<sub>0.14</sub>Ga<sub>0.86</sub>N by 1MeV electron radiation,” *Applied Physics Letters*, vol. 86, 261906, 2005.
- [43] H. Itoh, *et al.*, “Intrinsic Defects in Cubic Silicon Carbide”, *Physica Status Solidi A*, vol. 162, pp. 173-198, 1997.
- [44] J. F. Kucko, *Insulator Charging in RF MEMS Capacitive Switches*, Air Force Institute of Technology (AU), Wright-Patterson AFB, OH, June 2005 (ADA441556).
- [45] B. D. White, *et al.*, “Characterization of 1.8 MeV proton irradiated AlGa<sub>N</sub>/Ga<sub>N</sub> field-effect transistor structures by nanoscale depth-resolved luminescence spectroscopy,” *IEEE Transactions on Nuclear Science*, vol. 49, no. 6, pp. 2695-2701, Dec. 2002.
- [46] D. C. Look, *et al.*, “Residual native shallow donor in ZnO”, *Physical Review Letters*, vol. 82 pp. 2552-2558, 1999.

- [47] B. Luo, *et al.*, “High-energy proton irradiation effects on AlGa<sub>N</sub>/Ga<sub>N</sub> high-electron mobility transistors”, *Journal of Electronic Materials*, vol. 31, no. 5, pp. 437-441, 2002.
- [48] Gaudreau, *et al.*, “Transport Properties of Proton-Irradiated Gallium Nitride-Based Two-Dimensional Electron-Gas System,” *IEEE Transactions on Nuclear Science*, vol. 49, no. 6, pp. 2702-2707, Dec. 2002.
- [49] X. Hu, *et al.*, “Proton-irradiation effects on AlGa<sub>N</sub>/Al<sub>N</sub>/Ga<sub>N</sub> high electron mobility transistors,” *IEEE Transactions on Nuclear Science*, vol. 50, no. 6, pp. 1791-1796, Dec. 2003.
- [50] B. Jun, S. Subramanian, “Carrier removal rate and mobility degradation in heterojunction field effect transistor structures”, *IEEE Transactions on Nuclear Science*, vol. 49, no. 6, pp. 3222-3229. Dec. 2002.
- [51] B. D. White, *et al.*, “Electrical, spectral, and chemical properties of 1.8 MeV proton irradiated AlGa<sub>N</sub>/Ga<sub>N</sub> HEMT structures as a function of proton fluence,” *IEEE Transactions on Nuclear Science*, vol. 50, no. 6, pp. 1934-1941, Dec. 2003.
- [52] X. Hu, *et al.*, “The energy dependence of proton-induced degradation in AlGa<sub>N</sub>/Ga<sub>N</sub> high electron mobility transistors,” *IEEE Transactions on Nuclear Science*, vol. 51, no. 2, pp. 293-297, Apr. 2004.
- [53] O. Aktas, *et al.*, “<sup>60</sup>Co gamma radiation effects on DC, RF, and pulsed I-V characteristics of AlGa<sub>N</sub>/Ga<sub>N</sub> HEMTs,” *Solid State Electronics*, vol. 48, pp. 471-475, 2004.
- [54] A. Y. Polyakov, *et al.*, “Neutron irradiation effects on electrical properties and deep-level spectra in undoped n-AlGa<sub>N</sub>/Ga<sub>N</sub> heterostructures,” *Journal of Applied Physics*, vol. 98, 033529, 2005.
- [55] P. Karmarkar, *et al.*, “Proton irradiation effects on Ga<sub>N</sub>-Based high electron-mobility transistors with Si-doped Al<sub>x</sub>Ga<sub>1-x</sub>N and thick Ga<sub>N</sub> cap layers,” *IEEE Transactions on Nuclear Science*, vol. 51, no. 6, pp. 3801-3806, Dec. 2004.
- [56] G. Sonia, *et al.*, “Proton and Heavy Ion Irradiation Effects on AlGa<sub>N</sub>/Ga<sub>N</sub> HFET Devices,” *IEEE Transactions on Nuclear Science*, vol. 53, no. 6, pp. 3661-3666, Dec. 2006.
- [57] S. Karmalkar, D. M. Sathaiya, M. Shur, “Mechanism of the reverse gate leakage in AlGa<sub>N</sub>/Ga<sub>N</sub> high electron mobility transistors,” *Applied Physics Letters*, vol. 82, pp. 3976-3978, 2003.

- [58] S. Fleischer, P.T. Lai, Y. C. Cheng, “Simplified closed-form trap-assisted tunneling model applied to nitrided oxide dielectric capacitors”, *Journal of Applied Physics*, vol. 72, no. 12, pp. 5711-5715, December 1992.
- [59] C. Svensson, I. Lundstrom, “Trap assisted charge injection in MNOS structures”, *Journal of Applied Physics*, vol. 44, no. 10, pp. 4657, 1973.
- [60] D. M. Saithaiya and S. Karmalkar, “Thermionic trap-assisted tunneling model and its application to leakage current in nitrided oxides and AlGa<sub>N</sub>/Ga<sub>N</sub> high electron mobility transistors,” *Journal of Applied Physics*, vol. 99, 093701, 2006.
- [61] Taurus Medici-Davinci Device Simulation Program, Version Y-2006.06, Synopsys Inc., June 2006.
- [62] NI Labview Professional Development System, Version 8.2, National Instruments Inc., 2006.
- [63] NI Measurement and Automation Explorer, Version 4.1.0.3001, National Instruments Inc., 2006.
- [64] Microsoft Visual Basic 6.0 SP5, Version 8988, Microsoft Corporation, 2000.
- [65] T. A. Jarzen, *Capacitance-Voltage Study on the Effects of Low Energy Electron Radiation on Al<sub>0.24</sub>Ga<sub>0.76</sub>N/GaN High Electron Mobility Transistors*, Air Force Institute of Technology (AU), Wright-Patterson AFB OH, March 2005.
- [66] T. E. Gray, *Investigation of Gate Current in Neutron Irradiated AlGa<sub>N</sub>/Ga<sub>N</sub> Heterostructure Field Effect Transistors Using Voltage and Temperature Dependence*, Air Force Institute of Technology (AU), WPAFB, OH, March 2007.
- [67] J. E. Turner, *Atoms, radiation, and radiation protection*, New York, McGraw-Hill, 1992.
- [68] T. Mnatsakanov, M. Levinshtein b, L. Pomortseva S. Yurkov, G. Simin, M. Khan, “Carrier mobility model for Ga<sub>N</sub>”, *Solid-State Electronics*, vol. 47, pp. 111–115, 2003.
- [69] Z-Q. Fang, *et al.*, “Deep centers in as-grown and electron-irradiated n-Ga<sub>N</sub>,” *IEEE 11th International Conference on Semiconductor and Insulating Materials*, pp. 35-42, Jul. 2000.
- [70] D. M. Sathaiya, S. Karmalkar, “A model for the high field leakage current in nitrided oxides”, *Journal of Applied Physics*, vol. 101, 106104, 2007.

- [71] S. Nozaki, H. Feick, E. R. Weber, M. Micovic, and C. Nguyen, "Compression of the dc drain current by electron trapping in AlGa<sub>N</sub>/Ga<sub>N</sub> modulation doped field-effect transistors," *Applied Physics Letters*, vol. 78, pp. 2896-2898, 2001.
- [72] D. Qiao, L. S. Yu, L. Jia, P. M. Asbeck, and S. S. Lau, "Transport properties of the advancing interface ohmic contact to AlGa<sub>N</sub>/Ga<sub>N</sub> heterostructures," *Applied Physics Letters*, vol. 80, pp. 992-994, 2002.
- [73] M. A. Khan, X. Hu, A. Tarakji, G. Simin, and J. Yang, "AlGa<sub>N</sub>/Ga<sub>N</sub> metal-oxide-semiconductor heterostructure field-effect transistors on SiC substrates," *Applied Physics Letters*, vol. 77, pp. 1339-1341, 2000.
- [74] D. M. Sathaiya, S. Karmalkar, "A Closed-Form Model for Thermionic Trap-Assisted Tunneling", *IEEE Transactions On Electron Devices*, vol. 55, no. 2, pp. 557-564, February 2008.
- [75] R. Gaska, J. W. Yang, A. Osinsky, Q. Chen, M. A. Khan, A. O. Orlov, G. L. Snider, M. S. Shur, "Electron transport in AlGa<sub>N</sub>-Ga<sub>N</sub> heterostructures grown on 6H-SiC substrates", *Applied Physics Letters*, vol. 72, no. 6, pp. 707-709, 1998.
- [76] W. J. Chang, M. P. Houg, Y. H. Wang, "Simulation of stress-induced leakage current in silicon dioxides: A modified trap-assisted tunneling model considering Gaussian-distributed traps and electron energy loss", *Journal of Applied Physics*, vol. 89, no. 11, pp. 6285-6293, June 2001.
- [77] Z. -Q. Fang, D. C. Look, D. H. Kim, I. Adesida, "Traps in AlGa<sub>N</sub>/Ga<sub>N</sub>/SiC heterostructures studied by deep level transient spectroscopy, *Applied Physics Letters*, vol. 87, 182115, 2005.
- [78] T. Hashizume, J. Kotani, H. Hasegawa, "Leakage mechanisms in Ga<sub>N</sub> and AlGa<sub>N</sub> Schottky interfaces", *Applied Physics Letters*, vol. 84, no. 24, pp. 4884-4886, June 2004.
- [79] D. M. Sathaiya, S. Karmalkar, "Edge Effects on Gate Tunneling Current in HEMTs", *IEEE Transactions On Electron Devices*, vol. 54, no. 10, pp. 2614-2622, October 2007.
- [80] D. M. Sathaiya, S. Karmalkar, "A Closed-Form Model for Thermionic Trap-Assisted Tunneling", *IEEE Transactions On Electron Devices*, vol. 55, no. 2, pp. 557-564, February 2008.
- [81] D. Qiao, L. S. Lu, S. S. Lau, J. M. Redwing, J. Y. Lin, H. X. Jiang, "Dependence of Ni/AlGa<sub>N</sub> Schottky barrier height on Al mole fraction", *Journal of Applied Physics*, vol. 87, no. 2, pp. 801-804, January 2000.

- [82] G. P. Summers, E. A. Burke, P. Shapiro, S. R. Messenger, and R. J. Walters, "Damage correlations in semiconductors exposed to gamma, electron, and proton irradiations," *IEEE Transactions on Nuclear Science*, vol. 40, pp. 1372-1379, 1993.
- [83] Andre Holmes-Siedle and Len Adams, *Handbook Of Radiation Effects – Second Edition*, Oxford Press, 2004.
- [84] T. P. Ma, P. V. Dressendorfer, *Ionizing Radiation Effects in MOS Devices and Circuits*, John Wiley and Sons, 1989.
- [85] S. A. Goodman, F. D. Auret, M. J. Legodi, B. Beaumont, and P. Gibart. "Characterization of electron-irradiated n-GaN," *Applied Physics Letters*, vol. 78, 3815, 2001.
- [86] Z.-Q. Fang, J. W. Hensky, D. C. Look, and M. P. Mack. "Electron-irradiation-induced deep level in n-type GaN," *Applied Physics Letters*, vol. 72, 448, 1998.
- [87] Sentaurus Workbench, Version Y-2006.06, Synopsys Inc., June 2006.
- [88] T. Hashizume, S. Ootomo, T. Inagaki, H. Hasegawa, "Surface passivation of GaN and AlGaIn-GaN heterostructures by dielectric films and its application to insulated-gate heterostructure transistors", *Journal of Vacuum Science, Tech. B, Condensed Matter*, vol. 21, no. 4, pp. 1828-1838, 2003.
- [89] W. S. Tan, M. J. Uren, P.A. Houston, R. T. Green, R. S. Balmer, T. Martin, "Surface Leakage Currents in SiN Passivated AlGaIn/GaN HFETs" *IEEE Electron Device Letters*, vol. 27, no. 1, pp. 1-3, January 2006.
- [90] Y.-F. Wu, *et al.*, "30-W/mm GaN HEMTs by Field Plate Optimization", *IEEE Electron Device Letters*, vol. 25, no. 3, pp. 117-119, March 2004.
- [91] M. McCluskey, *et al.*, "Evidence for Oxygen DX Centers in AlGaIn" *Material Research Society Symposium Proceedings*, vol. 512. pp.531-536, 1998.
- [92] D. K. Schroder, *Semiconductor Material and Device Characterization, Second Edition*, pp. 368-373, John Wiley and Sons, New York, 1998.
- [93] L. Chengzhan, L. Jian, L. Xinyu, L. Guoguo, L. Dan, C. Xiaojuan, H. Zhijing, "Effect of Passivation on Increasing of AlGaIn/GaN HEMT Gate Reverse Current", *Proceedings of the IEEE*, 2006.



**REPORT DOCUMENTATION PAGE**

*Form Approved  
OMB No. 0704-0188*

The public reporting burden for this collection of information is estimated to average 1 hour per response, including the time for reviewing instructions, searching existing data sources, gathering and maintaining the data needed, and completing and reviewing the collection of information. Send comments regarding this burden estimate or any other aspect of this collection of information, including suggestions for reducing the burden, to Department of Defense, Washington Headquarters Services, Directorate for Information Operations and Reports (0704-0188), 1215 Jefferson Davis Highway, Suite 1204, Arlington, VA 22202-4302. Respondents should be aware that notwithstanding any other provision of law, no person shall be subject to any penalty for failing to comply with a collection of information if it does not display a currently valid OMB control number.

**PLEASE DO NOT RETURN YOUR FORM TO THE ABOVE ADDRESS.**

1. REPORT DATE (DD-MM-YYYY)			2. REPORT TYPE		3. DATES COVERED (From - To)	
4. TITLE AND SUBTITLE				5a. CONTRACT NUMBER		
				5b. GRANT NUMBER		
				5c. PROGRAM ELEMENT NUMBER		
6. AUTHOR(S)				5d. PROJECT NUMBER		
				5e. TASK NUMBER		
				5f. WORK UNIT NUMBER		
7. PERFORMING ORGANIZATION NAME(S) AND ADDRESS(ES)				8. PERFORMING ORGANIZATION REPORT NUMBER		
9. SPONSORING/MONITORING AGENCY NAME(S) AND ADDRESS(ES)				10. SPONSOR/MONITOR'S ACRONYM(S)		
				11. SPONSOR/MONITOR'S REPORT NUMBER(S)		
12. DISTRIBUTION/AVAILABILITY STATEMENT						
13. SUPPLEMENTARY NOTES						
14. ABSTRACT						
15. SUBJECT TERMS						
16. SECURITY CLASSIFICATION OF:			17. LIMITATION OF ABSTRACT	18. NUMBER OF PAGES	19a. NAME OF RESPONSIBLE PERSON	
a. REPORT	b. ABSTRACT	c. THIS PAGE			19b. TELEPHONE NUMBER (Include area code)	